Studies on Molecular Manipulation for Polariton Electrochemistry

ポラリトン電気化学反応に向けた

分子制御の研究

Nobuaki　Oyamada

小山田　伸明

Graduate School of Chemical Sciences and Engineering

Hokkaido University

北海道大学大学院総合化学院

2023

Contents

Chapter 1 General introduction ····· 1

1.1 Electrochemical reaction at electrode

1.2 Plasmon polariton and light coupling

1.3 Molecular motion in electric field

1.4 Electric-field enhanced vibrational spectroscopy

1.5 Electrochemical control of interfacial molecules

1.6 Electrochemical reaction of water

1.7 Aim of this thesis

1.8 References

Chapter 2 2D-difussion modulation on plasmonic arrays ·····33

2.1 Introduction

2.2 Experimental method

2.2.1 Raman optical measurement combined electrochemical cell
2.2.2 Angle-resolved nanosphere lithography (AR-NSL)
2.2.3 Solution preparation for molecular manipulation system

2.3 Results and discussion

2.3.1 Optical mode of plasmonic arrays
2.3.2 Spectroscopic identification of adsorbed molecules by SERS
2.3.3 Solvent and electrolyte dependence of interfacial molecular motion
2.3.4 Evaluation of molecular property for diffusion modulation
2.3.5 Electrochemical control of adsorbed molecules

2.4 Conclusion

2.5 References

Chapter 3 Molecular selective condensations at the localized electric field of single bowtie gap ····· 65

3.1 Introduction

3.2 Experimental method

3.2.1 Electric field evaluation by FDTD method
3.2.2 Fabrication of single bowtie structure
3.2.3 Electrochemical control of adsorbed molecules at a single hot spot
3.2.4 Time tracing of molecular condensation in bi-analyte solution

3.3 Results and discussion

3.3.1 Estimation of optical force
3.3.2 Raman certification of plasmon-enhanced electric field
3.3.3 *In-situ* probing of switching behavior from single hotspot
3.3.4 Condensation behavior depending on molecular concentration
3.3.5 Molecular number estimation of trapped molecules
3.3.6 Condensation by adsorbate interaction and charge transfer resonance

3.4 Conclusion

3.5 References

Chapter 4 Control of interfacial water structures at electrified nanostructure interface ·····95

4. 1 Introduction

4. 2 Experimental method

4.2.1 Set-up of static pressured electrochemical Raman cell

4.2.2 Sample fabrication of Ag electrode by oxidation-reduction cycle

4. 3 Results and discussion

4. 3. 1 Pressure-dependent water oxidation and reduction
4. 3. 2 Electrochemical SERS measurement under static pressures
4. 3. 3 Interfacial water structure at negative electrochemical potential
4. 3. 4 Nanostructure effects for isotope effects on HER

4. 4 Conclusion

4. 5 References

Chapter 5 Accelerations of hydrogen evolution reaction via tuning plasmon modes ····· 117

5.1 Introduction

5.2 Experimental method

5.2.1 Finite difference time domain simulation of nanostructures
5.2.2 Fabrication of nanostructure for hydrogen evolution reactions
5.2.3 Reflection spectroscopy under static pressure
5.2.4 Video analysis of HER on the nanostructures

5.3 Results and discussion

5.3.1 Conformation of optical mode of nanostructures
5.3.2 Evaluation of hydrogen evolution on each plasmon mode

5.4 Conclusion

5.5 References

Chapter 6 General conclusions ····· 135

Acknowledgment

Chapter 1

General introduction

1.1 Electrochemical reaction at electrode

Many studies of chemical reactions at the electrode interface have been carried out since the 18th century for the development of civilization. To date, there are still enormous challenges in finding the method to obtain desirable molecules, such as hydrogen gas, as future energy resources.[1,2] In electrochemical reaction, the interactions between molecules and electrode materials are critically important to determine the reactivity.[3–5] Therefore, the main strategy for designing the chemical reaction to achieve efficient reactivity is limited to the extensive study of materials and surface modifications to improve reaction activity as catalysts (Figure 1-1). In addition to studies of electrode

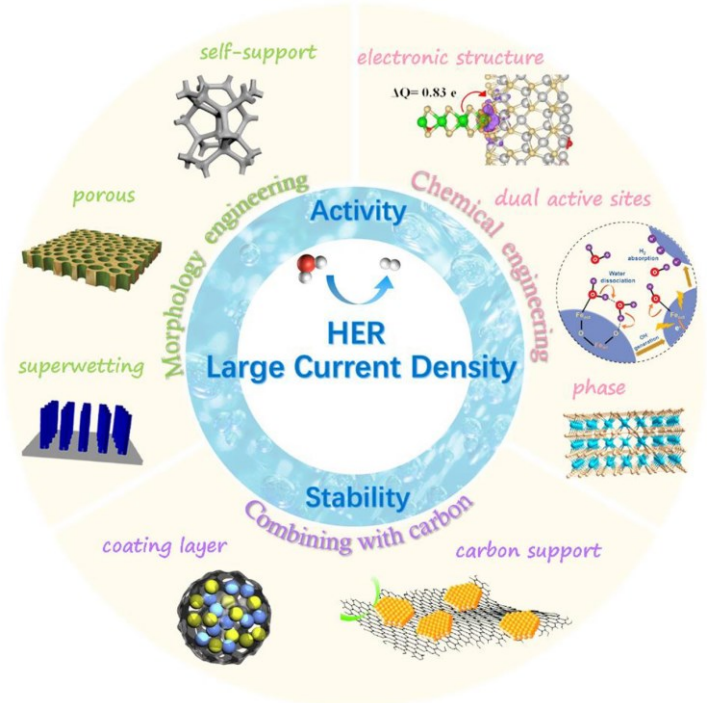

Figure 1-1. Schematic examples of various experimental approach to achieve efficient hydrogen evolution reaction by electrochemical reaction.[1]

materials, from recent progress about interfacial chemistry, the new aspects about interfacial water are revealed.[6] At the electrified interface for example of H_2O, the solvated cation plays an important role in defining the water structure and the OH bonding energy, which is related with chemical reactivity.[7–10] Therefore the element of electrode and solution components determine the electronic states of molecules as the reactants, intermediates and products.[11,12] At this point of view, in contrast to this classical method of inventing active electrode materials, one of the possible approaches to control reactivity is the coupling of the polariton mode and the interfacial water, which is hardly defined conventionally. Recently, some report shows that the polariton control could be change the energy states or the reaction path.[13,14] For the ultimate molecular reaction control, the defined polariton mode of molecules as a result of interaction in between molecules and polariton mode of electrode, called molecular polariton shown in Figure 1-2, has a possibility to innovate the various chemical reaction on arbitrary materials fundamentally.[15] Thus for first step of ultimate molecular manipulation, it is necessary to understand the interactions between molecules and defined polariton mode .

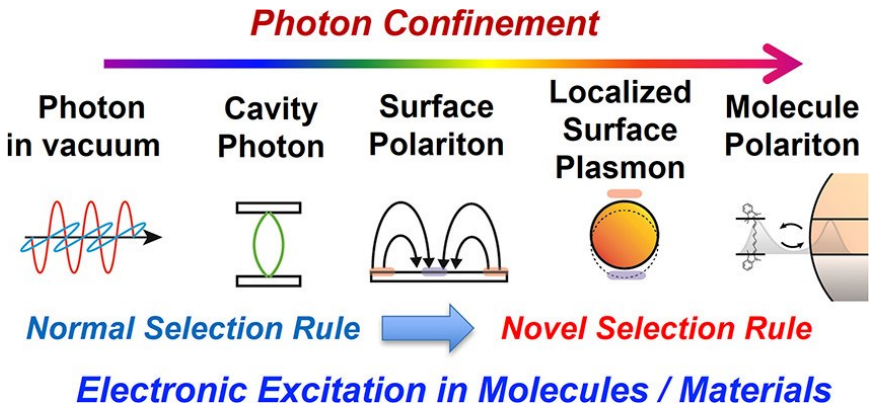

Figure 1-2. Schematic of polariton mode from light to molecular polariton states, leading to the modification of electronic excitations as coupling polariton.[15]

1. 2 Plasmon polariton and light coupling

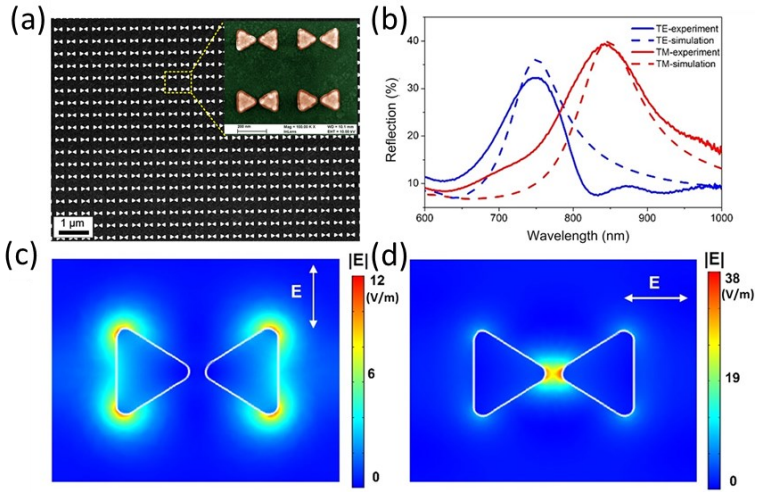

Figure 1-3. (a) Scanning electron microscopy image of the Au bowtie nano antenna arrays. (b) Experimental (solid lined) and simulated (dashed line) reflection spectra of the bowtie nano nano antenna arrays in water with incident TE (blue) and TM (red) polarized light. (c, d) Normalized electric field distributions from FDTD calculation at the resonances under (c) the TE and (d) TM polarization, respectively.[26]

The plasmon is well known as the confined polariton mode that easily couples the light and matter in the visible region at room temperature.[16,17] In nanostructures of noble metals such as Au, Ag, and Cu, free electrons in the metal structure resonate with visible light irradiation, inducing the excitation of local surface plasmon resonance (LSPR). By the LSPR, an electromagnetic field localized which is different from ordinary electromagnetic waves generates in the vicinity of metal nanoparticles that is. [18] In this case, the energy of the light can be localized into the nm-order region beyond the diffraction limit. [18–25] Interestingly, because the plasmon mode has the special symmetry as polarization of electrons, both the resonant wavelength and the polarization direction are could be tuned by the structural geometry as shown in Figure 1-3a, b, and c.[26] Metallic nanoparticles inducing LSPR showed that the electric field of the incident light is enhanced by a factor of 10^3 at the junction.[27] Such near field electric intensity is expected to enable reaction control and physical manipulation of the single-molecule.[28–33]

The dipole oscillating is formed inside the metal at this time when the single photon irradiation. After that, the electric field created by the dipole immediately is excited at t = 0 described from Maxwell's equations. It is commonly derived through a mathematical process called gauge transformation that satisfies the Lorentz condition to Maxwell's equations for the magnetic $(B(r,t))$ and electric $(E(r,t))$ field in a dielectric as follows. [34,35]

$$B(r,t) = \frac{\mu_0}{4\pi}\left\{-\frac{p(t_0)}{r^3} - \frac{r\times\ddot{p}(t_0)}{cr^2}\right\} \qquad \text{(Equation 1-1)}$$

$$E(r,t) = \frac{1}{4\pi\varepsilon_0}\left\{-\frac{p(t_0)}{r^3} + \frac{3r\,r\cdot p(t_0)}{r^5} + \frac{p(t_0)}{cr^2} + \frac{3r\,r\cdot\dot{p}(t_0)}{cr^4} + \frac{r\times r\times\ddot{p}(t_0)}{c^2r^3}\right\} \qquad \text{(Equation 1-2)}$$

Since the spherical surface area of the radiation field is described as $4\pi r^2$, the intensity per unit area is assigned by the value of r^2, so the far field has no intensity because the intensity decays faster than the square of distance. The first and second terms in Equation 1-2 are the electric field distribution created by a point charge, called the electrostatic field, which decays inversely proportional to r^3 as a net exponent. The third and fourth terms in the Equation 1-2 are the induced fields in the flowing current by the oscillation of the charge and also inversely proportional to r^2 with decay in the same way of surface area. The fifth term is called the radiation field because it is inversely proportional to r and has more than 1 intensity even in the far from point charge. Almost all spectroscopic scattering cross sections by experiments are derived from this fifth term as detection of propagating light. On the other hand, first term called as the near-field component, dominant in the region $r << \lambda$ (wavelength) distance from the center of the spherical nanoparticle.[34] So this is the reason why plasmon resonance induced the local electric field in the vicinity of the metal surface.

While the LSPR mode has the highly localized electric filed, the two-dimensionally arranged metal nanostructures excite the unique plasmon mode recognized as the surface lattice resonance (SLR) mode. The SLR mode is the coupling between LSPR and diffraction light from each nanostructure and shows the relatively delocalized electric field distribution near to wavelength order.[36–38] The SLR wavelength called Rayleigh anomaly is determined by diffraction order of lattice as following equation.[39]

$$\lambda_{m,p} = \frac{a}{(m^2+p^2)}\sqrt{n_2^2(m^2+p^2) - n_1^2 p^2 \sin^2\theta} \pm mn_1 \sin\theta \qquad \text{(Equation 1-3)}$$

In the equation, periodicity is a nm and refractive indexes of substrate or surroundings

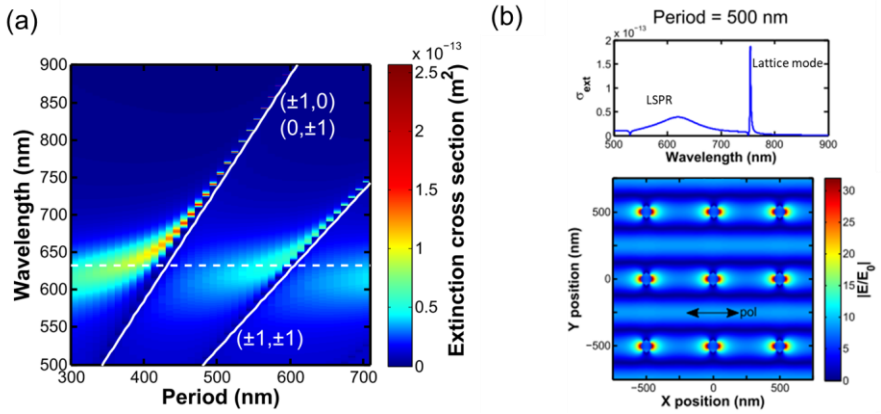

Figure 1-4. (a)Normal incidence extinction cross-section spectrum calculated with FDTD for a square array of gold nanodisks with diameter D= 80 nm and thickness h = 50 nm and (b) with periodicity a= 500 nm. The field map in bottom is calculated in the arrow indicating.[39]

are n_1 or n_2, respectively. The term of θ is the angle of incident light, and m and p integers correspond to the diffracted order of the anomaly. As definition of SLR, the peak wavelength is easily tuned by nanostructure diameter and period distance in the entire visible to infrared wavelength as shown in Figure 1-4a. Typically SLR mode shows very sharp absorption, corresponding to high Q value, because of that mode supposed to be close to optical mode property as a cavity in Figure 1-4b. When the incident light shines on the substrate with angle, there are two type resonance with in-plane and out-plane

mode for the lattice dimension. [40] This property of SLR gives the possibility of arbitral mode design in nm to mm scale by structural control.

1.3 Molecular motion in electric field

One of dreams of chemical scientists and others is to control each molecule individually to induce desired chemical reactions. The control of single molecules one by one would realize the arbitrary modulation of chemical reaction pathways. It is well known that focused light could manipulate small materials. This technique is recognized as the laser trapping which has the potential for the ultimate manipulation of chemicals.[41–44] The optical force (F_{opt}) under the laser light illumination can be described as follows.[45,46]

$$< \boldsymbol{F_{opt}} > = \frac{I_0 \mathrm{n}}{\varepsilon_0 \mathrm{c}} \{ \alpha' \nabla \left(\frac{|\boldsymbol{E_{loc}}|}{|\boldsymbol{E_0}|} \right)^2 + \alpha'' \boldsymbol{k} \left(\frac{|\boldsymbol{E_{loc}}|}{|\boldsymbol{E_0}|} \right)^2 \} \qquad \text{(Equation 1-4)}$$

where n, ε_0, c, I_0, E_{loc}, and E_0 are the refractive index of the surrounding media, permittivity, the velocity of the light, incident light intensity, the intensity of the localized electric field, and the intensity of the electric field for the far field, respectively. The $\alpha'$and α'' are the real and imaginary polarizabilities of the targets. The former and latter parts of the right side of Equation 1-4 indicate the gradient and dispersion forces, respectively. The strong gradient force results in efficient light-induced trapping. Generally, the efficient trapping by the focused laser is limited to the micrometer scale-materials. This is because that the relatively small polarizability of the small size materials and the diffraction limit of the light prevent the F_{opt} to overcome the Brownian motion

(~1 k_BT).[47,48] However, because the metal nanostructures can enhance the E_{loc} up to 1000 times under the plasmon excitation, the strong light (~10 mW cm^{-2}) illuminations onto the material at the hot spot can achieve the relatively strong F_{opt} (~ 0.1 pN (= optical potential of 1 k_BT (4.1 × 10^{-21} J at 298 K)). In fact, recent efforts demonstrate the trapping of relatively small materials, such as metal particles,[49,50] polystyrene beads,[48,51,52], protein,[53,54] dye molecules,[55,56] or quantum dots,[57,58] at the plasmonic field. It is emphasized here that the target materials should still have a larger size or polarizability than 50 nm and ~2.0 × 10^{-38} C^2 m J^{-1}, respectively. However, the several small size molecules, e.g., Rhodamin-6G, Crystal Violet, or other fluorescent molecules, have been applied to the molecular trapping because they show the improved α'under the resonant condition, leading to ten times larger than that under the non-resonant condition.[59] Because of these facts, it can be said that the plasmon induced optical manipulation of small size molecules is still a big challenge.

Especially for molecules without absorption bands in the entire visible spectrum, the resonance frequency is equal to the energy required for electronic excitation, and the imaginary component of the polarizability is small. When the energy of incident light is small with respect to the resonance frequency, the polarizability can be approximated by α_0 as the real part of the static polarizability because there is no dispersion relation.

$$\alpha(\omega) = \alpha'(\omega) + i\,\alpha''(\omega) = \alpha_1 \frac{\omega_1^2}{\omega_1^2 - \omega^2 - i\omega\Gamma_1} + \alpha_\infty \qquad \text{(Equation 1-5)}$$

$$\alpha(\omega) \approx \alpha'(\omega) = \alpha_1 + \alpha_\infty = \alpha_0 \qquad \text{(Equation 1-6)}$$

Thus, the light pressure <*F*> and its potential can be described as the static polarizability real part α_0 of the numerator as follows.

$$\langle F \rangle = \frac{I_0 n}{c\varepsilon_0} \alpha_0 \nabla M_1 \quad (\alpha' \gg \alpha'') \qquad \text{(Equation 1-7)}$$

$$\mathrm{U} = \int \langle F \rangle \, dr \qquad \text{(Equation 1-8)}$$

Since the local electric field associated with the excitation of localized surface plasmon resonance generates only in a very narrow region, it affects only on molecules present in the electric potential gradient.[60–62] As expected from theory, in the enhanced electric field localized at hot spot , the particles are trapped within the less than wavelength order displacement in Figure 1-5.[62]

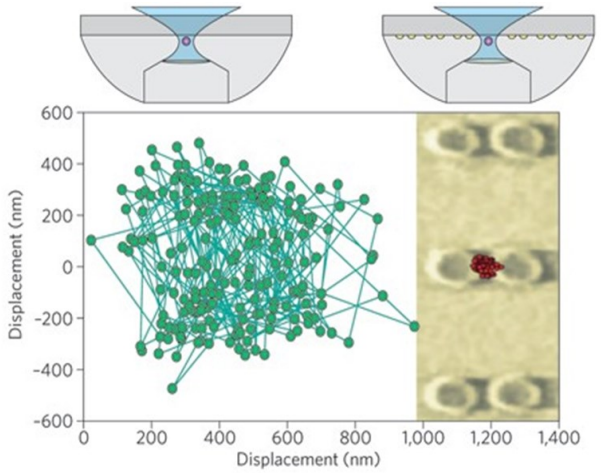

Figure 1-5. The mapping of polystyrene position trapped by optical tweezers (left) are spread widely. While the positions on plasmonic structure with light (right) are very concentrated on gap of dimers. [62]

It has been proposed that the existence probability of a molecule ($P(r, U)$) can be expressed approximately as the combination of the existence probability in the absence of light pressure and the light pressure potential, and can be treated by a simple equation as following. [46,63,64]

$$P(r, U) \propto P(r) exp\left(\frac{U}{k_B T}\right) \qquad \text{(Equation 1-9)}$$

The translational motion of molecules on a metal surface is determined by temperature, and a phenomenon called blinking, which is a time-dependent fluctuation of the spectrum,

and is not limited to cases where there is thermal convection due to light irradiation or electron transfer on the metal surface. [65–68] Furthermore, it is known that the smaller target molecules shows the wide spatial distributions due to the Brownian motion from the surrounding solvents.[68]

1.4 Electric-field enhanced vibrational spectroscopy

The localized electric field not only modulates the optical properties of the metal, but also causes a significant increase in scattering intensity in infrared absorption and Raman scattering spectroscopies due to the electromagnetic enhancement effect.[69–72] The intensity of the electric field itself in the vicinity of a porous plasmonic structure has a magnitude of up to 10^3 with respect to the incident electric field. This leads to experimental enhancement effect of Raman scattering up to 10^{12}, known as surface-

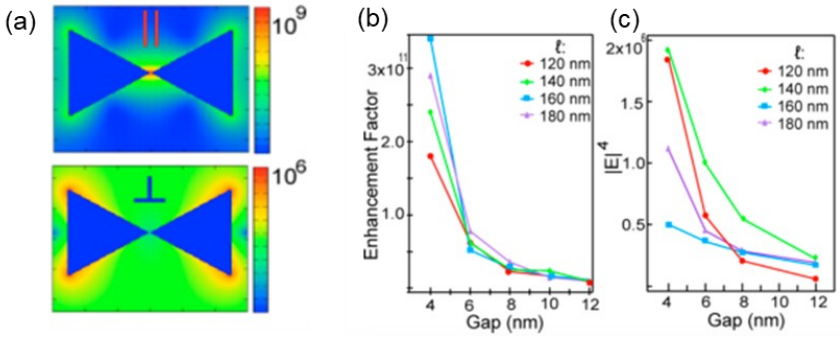

Figure 1-6. Au bowtie structure SERS activity. (a) Simulated electric field (E) images as $|E|^4$ scale with incident polarization direction parallel to long axis (upper panel) and perpendicular to long axis. (b) SERS intensity dependence of gap distance quoted from experimental spectra. (c) Calculated plot of $|E|^4$ as a function of gap distance. [73]

enhanced Raman scattering(SERS). [73] The magnitude of the electric field enhancement is determined by geometry and elements of substrate. For example, the narrow gap in the

Au bowtie shape excites relatively strong electric field depending on the gap distance (Figure 1-6). This highly enhanced molecular vibration is useful for understanding the interfacial molecular states and their motion influenced by plasmon.

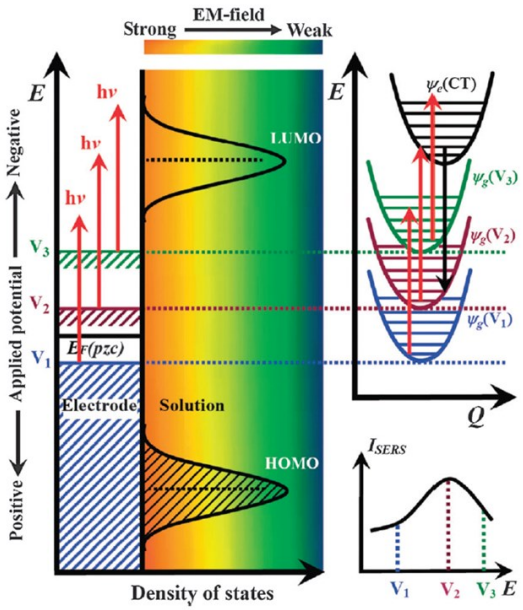

Figure 1-7. Schematic diagrams of the charge transfer (CT) from a metal electrode to an adsorbed molecule in the EC-SERS system. Electrochemical potential corresponds the fermi energy of electrode. CT resonance gives large intensity and different peaks from normal Raman scattering[80].

On the other hand, it is known that the Raman scattering cross-section is enhanced by an additional factor called the chemical enhancement effect. This is caused by the electron-orbit interaction between adsorbed molecules and the metal surface.[74–77] The latter enhancement has been proven both computationally and experimentally to be relatively weak compared to former enhancement factors, ranging from 10 to 10^2.[78,79] In addition, since chemical bonding is determined by the combination of molecule and metal, the spectral shape and intensity will vary depending on the type of metal, even for the same molecule.[80] Since the chemical bond changes the energy state of the adsorbed molecule, the charge transfer (CT) resonance occurs at the certain electrochemical

potential dependi ng on the metal as shown in Figure1-7. Fermi level in metal-molecule systems is expected to contribute to CT resonances in practice. The modulation of molecular levels can be predicted from density functional theory (DFT) calculations.[81] For example, in a model of pyridine adsorbed on a silver icosahedron, since the transition level from silver to pyridine empty orbitals can be determined for each electrochemical potential, the CT resonance effects at different incident wavelengths can be predicted.[82,83]

The resonant Raman effect is observed in strong scattering derived from vibrational excitations when the first electron transition resonates with the incident photon energy. When the excitation light is at a wavelength that satisfies the energy level difference between the highest occupied molecular orbital (HOMO) and the lowest unoccupied molecular orbital (LUMO), the Raman scattering intensity is enhanced by ~10^4 compared to normal Raman scattering.[84] The scattering process via LUMO of the molecular orbital also induces unusual excitation vibrations by the excited electrons. Therefore, resonant Raman scattering not only enhances the intensity but can also excite bands that are normally forbidden. Such resonant Raman scattering is caused from the outside of the metal into the reacting molecule under CT resonance.[85,86] The equations below are quantum mechanical treatment of the Raman scattering tensor. It is redefined quantum mechanically by several terms including the initial, intermediate, and final states.[84]

$$\alpha_{\rho\sigma} = A + B + C \qquad \text{(Equation 1-10)}$$

$$\mathrm{A} = \sum_{e \neq g} \sum_{v} \frac{[g_0|D_\sigma|e_0][e_0|D_\rho|g_0]}{E_e^0 + E_v^0 - E_g^0 - E_i^0 - E_i - i\Gamma_e} (i|v)(v|f) \qquad \text{(Equation 1-11)}$$

$$B = \sum_{e\neq g}\sum_{v}\sum_{k}\frac{[g_0|D_\sigma|e_0]\left[s_0\left|\left(\partial H_{mol}^{ev}/\partial Q_k\right)_0\right|e_0\right][e_0|D_\rho|g_0]}{E_e^0+E_v^0-E_g^0-E_i^0-i\Gamma_e}\frac{(i|Q_k|v)(v|f)}{\left(E_s^0-E_e^0\right)}$$

$$+\sum_{e\neq g}\sum_{v}\sum_{k}\frac{[g_0|D_\sigma|e_0]\left[e_0\left|\left(\partial H_{mol}^{ev}/\partial Q_k\right)_0\right|s_0\right][s_0|D_\rho|g_0]}{E_e^0+E_v^0-E_g^0-E_i^0-E_i-i\Gamma_e}\frac{(i|v)(v|Q_k|f)}{\left(E_s^0-E_e^0\right)} \qquad \text{(Equation 1-12)}$$

$$C = \sum_{g\neq s}\sum_{v}\sum_{k}\frac{\left[g_0\left|\left(\partial H_{mol}^{ev}/\partial Q_k\right)_0\right|s_0\right][s_0|D_\sigma|e_0][e_0|D_\rho|g_0]}{E_e^0+E_v^0-E_g^0-E_i^0-i\Gamma_e}\frac{(i|v)(v|Q_k|f)}{\left(E_s^0-E_e^0\right)}$$

$$+\sum_{g\neq s}\sum_{v}\sum_{k}\frac{[g_0|D_\sigma|e_0][e_0|D_\rho|s_0]\left[s_0\left|\left(\partial H_{mol}^{ev}/\partial Q_k\right)_0\right|g_0\right]}{E_e^0+E_v^0-E_g^0-E_i^0-E_i-i\Gamma_e}\frac{(i|v)(v|Q_k|f)}{\left(E_s^0-E_g^0\right)} \qquad \text{(Equation 1-13)}$$

In the above equations, the Frank-Condon term (A) of the electron and the Hertzberg-Teller term (B: Molecular to Metal, C: Metal to Molecular) are mainly considered. In resonant Raman scattering, the scattering originating from A and B is more likely to occur. In CT resonance, it has been theoretically and experimentally proven that the contribution from the C term is also included.[87] Several examples of CT resonance are obtained in pyridine-Ag nano particle system and water-Ag electrode.[88,89] This CT resonant states show direct observation of plasmon and molecular interaction as coupled states, in other words the molecular polariton is possibly understood by studying CT SERS.

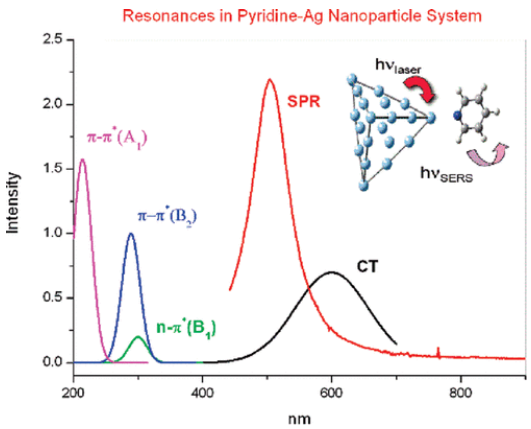

Figure 1-8. Experimental and simulated optical resonances in the pyridine-Ag nanoparticle with various wavelength for plasmon (simulated absorption), molecules (absorption) and CT (Raman). [88]

1.5 Electrochemical control of interfacial molecules

Unlike conventional Raman scattering, the orientation of molecules to the surface is the most important factor in SERS. This is because the vibrational polarizability tensor (Equation 1-14) as a key factor for determining the scattering intensity (Equation 1-15). The scattering intensity can be easily changed depending on the molecular position if the localized electric field has an anisotropic distribution.

$$\boldsymbol{\alpha} = \begin{pmatrix} \alpha_{xx} & \alpha_{xy} & \alpha_{xz} \\ \alpha_{yx} & \alpha_{yy} & \alpha_{yz} \\ \alpha_{zx} & \alpha_{zy} & \alpha_{zz} \end{pmatrix} \qquad \text{(Equation 1-14)}$$

$$I_s R^2 = \frac{{\omega_s}^4}{c^4} (e_s \alpha e_i)^2 I_i \qquad \text{(Equation 1-15)}$$

In particular, it is known that a change in surface potential can change the orientation of the adsorbate, resulting in a change in coverage. In the case of 2,2'-bipyrideine (22bpy) shown in Figure1-9, the nitrogen atoms in the positive potential

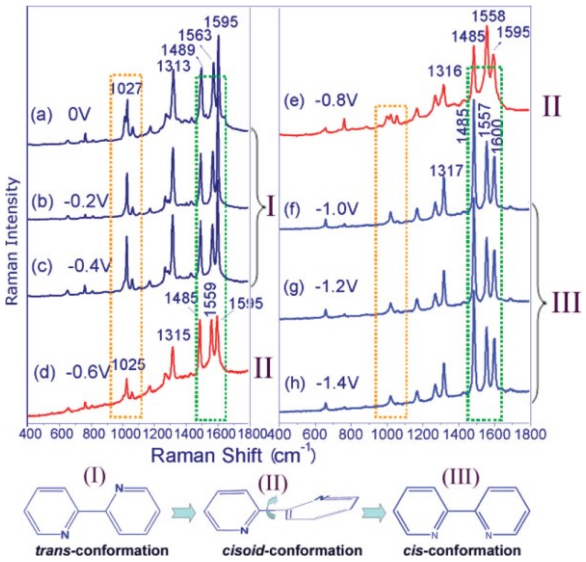

Figure 1-9. Orientation and SERS spectra of 22BPY molecules on a Ag-coated Ag electrode depend on potential (20 μL volume of 22BPY solution rapidly added onto the electrode surface and dried fully before adding the ice-cold KCl solution, 0.1 M, 0 ℃).[90]

region at the Ag electrode have both a trans structure and a cis structure.[90] On the Ag electrode, 22bpy stabilizes in the trans and cisoid structures with twisted nitrogen atoms in the positive potential region and stabilizes in the cis structure with aligned nitrogen atoms in the negative potential region. In the presence of an external magnetic field, both the orientation and intensity of the spectra change.

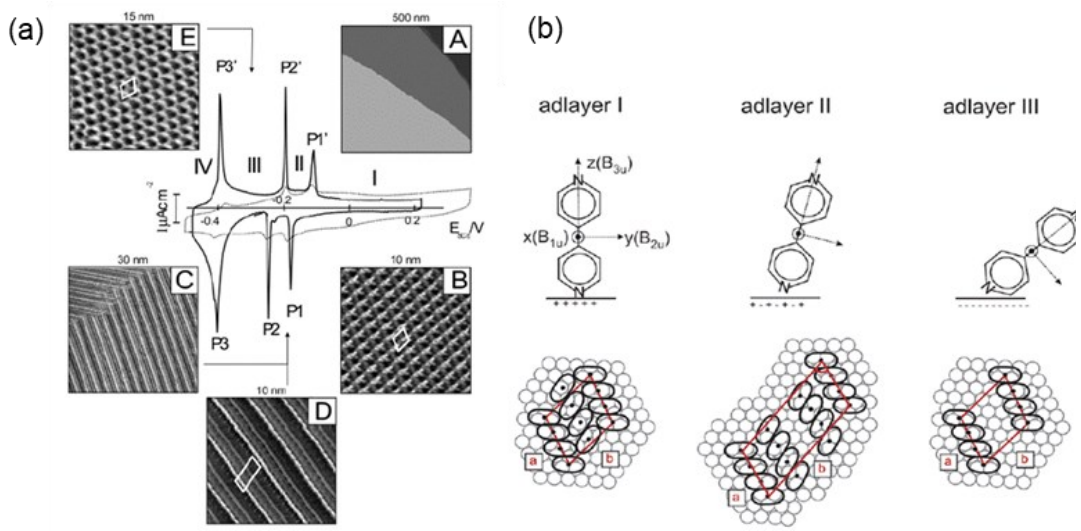

Figure 1-10. 44bpy adsorbed on Au (111) with particular orientation at certain applied potential. (a) Cyclic Voltammetry of 0.05 M $KClO_4$ + 3 mM 44bpy aq. and STM image. (b) Each phase orientation of 44bpy on Au(111) by SEIRAS and Estimated packing model.[91]

In the case of structure isomer 4,4'-bipyridine (44bpy), the stabilization of Gibbs energy by adsorption is strongly dependent on the orientation, which is controlled by the surface potential. Figure 1-10a shows the orientation change of 44bpy on the Au(111) plane in cyclic voltammetry (CV), which was observed by scanning tunneling electron microscopy (STM).[91] The orientation is sensitive to the potential, and the alignment also changes with the orientation. The peak of the CV is not perfectly symmetrical with respect to the sweep direction of the potential due to the overvoltage against desorption. Therefore, the CV peak shows a dependence on the sweep direction. Detailed STM

studies have shown that the fine-packed adlayer IV, i.e., edge-on type orientation, occupies an area of 0.4 nm^2 per molecule, and the cis-type orientation of 22bpy is considered to be similar to this case. Although there is a proportional relationship between the concentration of molecules in SERS in aqueous solution, the coverage, and the SERS intensity, the correlation with the molecular coverage is not linear. While, in the case of pyrazine molecule, the coverage increases nonlinearly with concentration, the SERS intensity increases linearly with concentration, suggesting that SERS is sensitive to interactions with molecules at the metal surface and is modulated by electron transfer as well as orientation and packing structure.[92]

For the case of water at metal interface, the orientation of adsorption also changes with surface potential.[93] Experimentally, the energies of water molecules at the Au interface have been estimated from X-ray absorption spectra, and the orientation of the water molecules has been assigned by observing the hydrogen-bonding network at different potentials.[94] On the Au surface, it was found that the number of water molecules

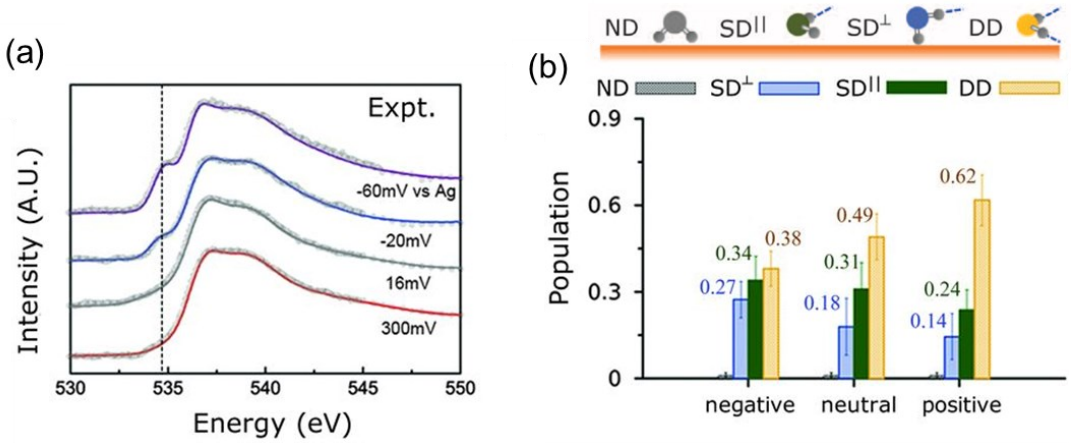

Figure 1-11. Experimental O K-edge total electron yield XAS spectra of water, collected at an Au electrode under polarization. (b) The Populations of H-bonded water molecules deduced from these spectra at different polarization. Number of hydrogen-bond donors of interfacial water molecules at different potentials on an Au electrode calculated from in- situ Raman. [94]

with one of their hydrogen bonds pointing toward the surface increases as toward the negative potential, whereas a relatively large fraction of water molecules are free to exist on the surface in the negative potential side through the combination of XAS and Raman measurements (Figure 1-11). This result was also confirmed by SERS using Au thin films and gold particles, where the orientation of water molecules at the interface is strictly controlled by the potential.[95] On the other hand, the behavior of water at the electrode surface during hydrogen evolution is complicated by the effect of adsorbed hydrogen.[96] As an example, it has been electrochemically verified that hydrogen atoms adsorbed on Pt change the exchange current and even the rate constant of the Arrhenius equation depending on the miller index of crystal plane. One reason for this is thought to be that hydrogen atoms attach perpendicularly to the metal surface in Pt(110), whereas, in Pt(100), they adsorb sideways, preventing bonding with surrounding water or other adsorbed hydrogen diffusing across the surface. [97]

1.6 Electrochemical reaction of water

In both scientific interest and engineering point of view, water electrolysis is an important topic for energy resources. Especially for the production of hydrogen gas, many researchers have tried to make better catalysis.[5,98–100] In the hydrogen evolution reaction (HER), water is reduced to hydrogen gas irreversibly in typical condition as like bellow,

$$2H_2O\,(l) + 2\,e^- \rightleftarrows H_2(g) + 2\,OH^-(aq) \qquad \text{(Equation 1-16)}$$

That HER reaction consists of three elementary steps called as Volmer (Equation 1-17),

Heyrovsky (Equation 1-18), and Tafel step (Equation 1-19).[4,101,102]

$$H_2O\,(l) + e^- + M \rightleftarrows M - H_{ad} + OH^-(aq) \qquad \text{(Equation 1-17)}$$

$$M{-}H_{ad} + H_2O\,(l) + e^- \rightleftarrows H_2(g) + OH^-(aq) \qquad \text{(Equation 1-18)}$$

$$2M - H_{ad} \rightleftarrows H_2(g) \qquad \text{(Equation 1-19)}$$

While the first step of HER is always Volmer step, following rection strongly depends on electrode material due to H_{ad}-M binding energy recognized as the Sabatier principal with expression of volcano plot.[5,103] Since each elementary step has different intermediate sates and activation energy, Tafel slope or reaction rate differ from each other.[104] For revealing the elementary step of HER, one of the ways is to evaluate the isotope effects for HER because the reaction rate of light-hydrogen gas shows faster than that of heavy-hydrogen gas from 1 to 13 times in each elementary steps.[105–108] It is noted that the difference of thermodynamic property of H_2O and D_2O have small value such as zero-point energy, $\Delta E \approx 5$ kJ/mol, or as standard electrode potential of the reduction below. However, the difference of electrolysis voltage has relatively large more than 100 mV between isotopes depending on surroundings such as electrolytes and pH.[107–109]

$$H^+ + e^- \rightarrow \frac{1}{2}H_2(g)\,, E = 0\ \text{V vs. SHE} \qquad \text{(Equation 1-20)}$$

$$D^+ + e^- \rightarrow \frac{1}{2}D_2(g)\,, E = -0.013\ \text{V vs. SHE} \qquad \text{(Equation 1-21)}$$

There are also isotope effects in hydrogen bonding, for example, hydrogen bonding between water is only observed in the same mass isotope, so OD and OH have never

hydrogen bonded.[110] This difference modulates the hydrogen bonding network, resulting in changes in its energy and dynamic structure.[111,112]

Electrochemical SERS has been used as a tool to elucidate the electrode reaction of water at the interface.[80,113,114]. An electrochemical SERS has been used as a tool to elucidate the electrode reaction of water at the interface. One example is electrochemical SERS measurements between an Au particle and an Au thin film electrode. The strong electric field causes an increment of Raman scattering intensity. The further increase in scattering intensity and change in peak position are observed when the electrochemical potential is swept negatively as seen in Figure 1-12.[115] This phenomenon is considered to reflect the structure of water molecules at the gold surface. In particular, the modulation of the state of water molecules absorbed on the Au surface with Na^+ was also adsorbed. On the negative potential side, in addition to the orientation of water molecules due to the potential gradient, water molecules at the interface are expected to adsorb on Au in a

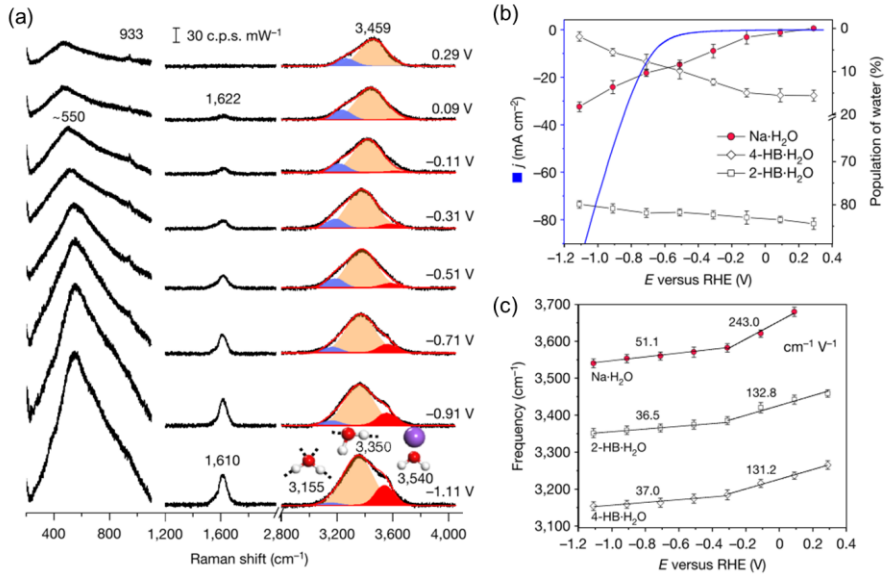

Figure 1-12. (a)Electrochemical SERS measurement of interfacial water on a Pd(111) in a 0.1 M NaClO4 aq. (pH 11). (b) Population of interfacial water from in spectral area and HER current density (c) Raman shift plots of the O–H stretching modes in Raman spectra of interfacial water are shown as a function of potential.[115]

different manner than usual during hydrogen evolution reaction. The orientation of adsorption is discussed here based on the aforementioned change in the water interfacial network structure from the shift of the peak position to the low wavenumber side. In addition, H-M and D-M, which are water reduction products after Volmer step (Equation 1-17), were observed in certain metals by performing spectroscopy during electrochemical reactions. Studies using core-shell structures, in which metals are stacked on noble metal nanoparticles to obtain electric field enhancement, have been reported for Pt and Rh with relatively strong metal-hydrogen bonding.[116,117] However, it is not observed for Ag and Au which have the weak metal-hydrogen bonding, despite their strong SERS enhancement intensity.[118]

Another influence on the in-situ measurement of water is the modulation of the electronic level of water molecules at the electrode surface. The energy for the electronic transition of water is about 7 eV for an isolated molecule, while it drops to about 5 eV in the clustered state adsorbed on a metal surface, as predicted by DFT calculations.[119] This means that the CT resonance condition can be satisfied in this adsorbed water with appropriate potential and visible wavelength. The effect of the presence of halogen ions has also been studied in a cluster model, and it has been reported that the energy required for the electronic transition is further reduced in a co-adsorbed system.[120] The change in reactivity associated with nanostructures is not limited to plasmons. Other effects such as decrease the overvoltage at the edges of crystals have also been observed.[121] Even at room temperature and in an atmosphere on the nanostructures, the ice and relatively free structure were simultaneously adsorbed at the interface[122] Thus, to achieve molecular polariton control after coupling of polaritons and water molecules, it is crucial to understand the interfacial water structure and energy states.

1.7 Aim of this thesis

As I mentioned in the above introductions, the control of electron transfer reactions at the solid-liquid interface has been discussed in recent years. However, at the present stage, the effect of the quantum nature of the field, which is another important degree of freedom in matter systems, is hardly considered, and the principle search and control of the field to modify chemical reactions is limited. I proposed that it is possible to modulate electronic states and reaction pathways by interacting with polariton modes and substances, we can achieve arbitral control of chemical reaction and selectivity in all material systems, not only catalytic metals and non-metallic catalysts. In this doctoral thesis, I focused on the polaritons and electrochemical reactions that can be correlated to investigate the control of translational and vibrational motions of molecules at the electrode interface as well as reaction modulation.

In Chapter 2, I systematically investigate the two-dimensional diffusion behavior of adsorbed bipyridine using large-area nanostructures and study the solvent, electrolyte, and electrochemical potentials. Efforts were made to establish the capture technology. The amount and state of the molecules were tracked by surface-enhanced Raman scattering (SERS) measurements, which showed that it is possible to control the translational motion of small organic molecules, which cannot be achieved by polarization control with ordinary light. I proposed the possibility of manipulating molecules in space by optical pressure.

In Chapter 3, to verify the light molecule trapping effect, a single bowtie structure was fabricated in which the local electric field is concentrated in the gap. As a result of verifying the plasmon molecular trapping effect depending on the

electrochemical potential, light intensity and light irradiation time. Moreover, the electrochemical potential sweep induced charge transfer resonance between the metal and the molecule by observing the characteristic scattering of the asymmetric vibration of the bipyridine molecule. I found that a unique optical pressure application is possible under the polariton formation. Furthermore, I clarified that a new molecular layer is formed in this resonance state, which cannot be achieved by thermodynamic adsorption equilibrium. I obtained knowledge on the formation of a specific molecular structure, which is the key to polariton electrochemical control.

In Chapter 4, I focused on the electrolysis reaction of water and designed a static pressure cell to perform SERS measurements during reaction at the Ag wire surface. I aim to apply the manipulation of molecular motion by the optical electric field achieved in Chapter 3 to the modulation of elementary step at the nanostructure interface where the electric field is concentrated. The water structure during hydrogen evolution reaction (HER) was verified by SERS measurement under hydrostatic pressure condition. As a result, it was clarified that the hydrated structure of electrolyte ions and structural changes of water molecules are induced when reduction reactions occur steadily. The results suggested the formation of polariton modes on the nanostructure surface. In addition, by mixing H_2O and D_2O, the elementary processes on the nanostructure based on isotope effects are also studied. By studying the Raman spectra of the reaction intermediates and the generated hydrogen-dissolved gases, it was possible to discuss that the selectivity of the electrochemical reaction is modulated depending on the molecular structure of the interface. Based on these results, I discussed the possibility of expressing catalytic activity in non-catalytic metals for hydrogen evolution reaction.

In Chapter 5, based on the results obtained above, structures were fabricated in which the plasmon mode was modulated from the visible to the infrared region. By substate, the hydrogen generation reaction efficiency depending on their optical modes was verified by microscopic video analysis of evolved hydrogen gas. Using Ag nanostructures, we quantitatively analyzed the rate of hydrogen gas bubble generation in a high hydrostatic pressure cell. The results revealed that the plasmonic properties of the nanostructures affect the rate of hydrogen generation, and provided structural design guidelines for controlling catalytic activity in non-catalytic metals.

Through these experiments, summarized in Chapter 6, I verified the interaction between the polariton mode of plasmon and electrochemical interface molecules. I also established the method for observing molecular behaviors and proposed the technique for controlling electrochemical reactions with polaritons. I achieved to understand the interaction of polaritons and chemical reactions for the improvement of not only catalyst metals but also a wide range of common materials.

1.8 References

(1) Jin, M.; Zhang, X.; Niu, S.; Wang, Q.; Huang, R.; Ling, R.; Huang, J.; Shi, R.; Amini, A.; Cheng, C. Strategies for Designing High-Performance Hydrogen Evolution Reaction Electrocatalysts at Large Current Densities above 1000 MA Cm –2. *ACS Nano* **2022**, *16* (8), 11577–11597.

(2) Wang, S.; Lu, A.; Zhong, C. J. Hydrogen Production from Water Electrolysis: Role of Catalysts. *Nano Converg.* **2021**, *8* (1).

(3) Bockris, J. O.; Reddy, A. K. N.; Vijh, A. K. *Modern Electrochemistry*; 1972; Vol. 119.

(4) Bard, A. J.; Faulkner, L. R. *ELECTROCHEMICAL METHODS Fundamentals and Applications*; 2001.

(5) McCrum, I. T.; Koper, M. T. M. The Role of Adsorbed Hydroxide in Hydrogen Evolution Reaction Kinetics on Modified Platinum. *Nat. Energy* **2020**, *5* (11), 891–899.

(6) Gonella, G.; Backus, E. H. G.; Nagata, Y.; Bonthuis, D. J.; Loche, P.; Schlaich, A.; Netz, R. R.; Kühnle, A.; McCrum, I. T.; Koper, M. T. M.; Wolf, M.; Winter, B.; Meijer, G.; Campen, R. K.; Bonn, M. Water at Charged Interfaces. *Nat. Rev. Chem.* **2021**, *5* (7), 466–485.

(7) Xue, S.; Garlyyev, B.; Watzele, S.; Liang, Y.; Fichtner, J.; Pohl, M. D.; Bandarenka, A. S. Influence of Alkali Metal Cations on the Hydrogen Evolution Reaction Activity of Pt, Ir, Au, and Ag Electrodes in Alkaline Electrolytes. *ChemElectroChem* **2018**, *5* (17), 2326–2329.

(8) Monteiro, M. C. O.; Goyal, A.; Moerland, P.; Koper, M. T. M. Understanding Cation Trends for Hydrogen Evolution on Platinum and Gold Electrodes in Alkaline Media. *ACS Catal.* **2021**, *11* (23), 14328–14335.

(9) Wang, P.-Y.; Zhou, J.-F.; Chen, H.; Peng, B.; Zhang, K. Activation of H 2 O Tailored by Interfacial Electronic States at a Nanoscale Interface for Enhanced Electrocatalytic Hydrogen Evolution . *JACS Au*. 2022.

(10) Singh, M. R.; Kwon, Y.; Lum, Y.; Ager, J. W.; Bell, A. T. Hydrolysis of Electrolyte Cations Enhances the Electrochemical Reduction of CO2 over Ag and Cu. *J. Am. Chem. Soc.* **2016**, *138*.

(11) Lv, F.; Feng, J.; Wang, K.; Dou, Z.; Zhang, W.; Zhou, J.; Yang, C.; Luo, M.; Yang, Y.; Li, Y.; Gao, P.; Guo, S. Iridium-Tungsten Alloy Nanodendrites as PH-Universal Water-Splitting Electrocatalysts. *ACS Cent. Sci.* **2018**, *4* (9), 1244–1252.

(12) Li, C.; Baek, J. B. Recent Advances in Noble Metal (Pt, Ru, and Ir)-Based Electrocatalysts for Efficient Hydrogen Evolution Reaction. *ACS Omega* **2020**, *5* (1), 31–40.

(13) Nagarajan, K.; Thomas, A.; Ebbesen, T. W. Chemistry under Vibrational Strong Coupling. *J. Am. Chem. Soc.* **2021**, *143* (41), 16877–16889.

(14) Chikkaraddy, R.; De Nijs, B.; Benz, F.; Barrow, S. J.; Scherman, O. A.; Rosta, E.; Demetriadou, A.; Fox, P.; Hess, O.; Baumberg, J. J. Single-Molecule Strong Coupling at Room Temperature in Plasmonic Nanocavities. *Nature* **2016**, *535* (7610), 127–130.

(15) Minamimoto, H.; Zhou, R.; Fukushima, T.; Murakoshi, K. Unique Electronic Excitations at Highly Localized Plasmonic Field. *Acc. Chem. Res.* **2022**, *55* (6), 809–818.

(16) Maier, S. A. *Plasmonics: Fundamentals and Applications*; Springer US: New York, NY, 2007.

(17) Hao, E.; Schatz, G. C. Electromagnetic Fields around Silver Nanoparticles and Dimers. *J. Chem. Phys.* **2004**, *120* (1), 357–366.

(18) Talley, C. E.; Jackson, J. B.; Oubre, C.; Grady, N. K.; Hollars, C. W.; Lane, S. M.; Huser, T. R.; Nordlander, P.; Halas, N. J. Surface-Enhanced Raman Scattering from Individual Au Nanoparticles and Nanoparticle Dimer Substrates. *Nano Lett.* **2005**, *5* (8), 1569–1574.

(19) Huang, J.-S.; Yang, Y.-T. Origin and Future of Plasmonic Optical Tweezers. *Nanomaterials* **2015**, *5* (2), 1048–1065.

(20) Rindzevicius, T.; Alaverdyan, Y.; Sepulveda, B.; Pakizeh, T.; Käll, M.; Hillenbrand, R.; Aizpurua, J.; García De Abajo, F. J. Nanohole Plasmons in Optically Thin Gold Films. *J. Phys. Chem. C* **2007**, *111* (3), 1207–1212.

(21) Zhang, G.; Wang, D.; Moehwald, H. Ordered Binary Arrays of Au Nanoparticles Derived from Colloidal Lithography. *Nano Lett.* **2007**, *7* (1), 127–132.

(22) Im, H.; Bantz, K. C.; Lee, S. H.; Johnson, T. W.; Haynes, C. L.; Oh, S.-H. Self-Assembled Plasmonic Nanoring Cavity Arrays for SERS and LSPR Biosensing. *Adv. Mater.* **2013**, *25* (19), 2678–2685.

(23) Denk, W.; Pohl, D. W. Near-Field Optics - Microscopy with Nanometer-Size Fields. *J. Vac. Sci. Technol. B* **1991**, *9* (2), 510–513.

(24) Xu, X. H. N.; Huang, S.; Brownlow, W.; Salaita, K.; Jeffers, R. B. Size and Temperature Dependence of Surface Plasmon Absorption of Gold Nanoparticles Induced by Tris(2,2 `-Bipyridine)Ruthenium(II). *J. Phys. Chem. B* **2004**, *108* (40), 15543–15551.

(25) Zhang, X.; Marocico, C. A.; Lunz, M.; Gerard, V. A.; Gun'Ko, Y. K.; Lesnyak, V.; Gaponik, N.; Susha, A. S.; Rogach, A. L.; Bradley, A. L. Experimental and Theoretical Investigation of the Distance Dependence of Localized Surface Plasmon Coupled Förster Resonance Energy Transfer. *ACS Nano* **2014**, *8* (2), 1273–1283.

(26) Wang, Q.; Liu, L.; Wang, Y.; Liu, P.; Jiang, H.; Xu, Z.; Ma, Z.; Oren, S.; Chow, E. K. C.; Lu, M.; Dong, L. Tunable Optical Nanoantennas Incorporating Bowtie Nanoantenna Arrays with Stimuli-Responsive Polymer. *Sci. Rep.* **2015**, *5* (September), 1–8.

(27) Hao, E.; Schatz, G. C. Electromagnetic Fields around Silver Nanoparticles and Dimers. *J. Chem. Phys.* **2004**, *120* (1), 357–366.

(28) Sprague-Klein, E. A.; McAnally, M. O.; Zhdanov, D. V.; Zrimsek, A. B.; Apkarian, V. A.; Seideman, T.; Schatz, G. C.; Van Duyne, R. P. Observation of Single Molecule Plasmon-Driven Electron Transfer in Isotopically Edited 4,4′-Bipyridine Gold Nanosphere Oligomers. *J. Am. Chem. Soc.* **2017**, *139* (42), 15212–15221.

(29) Choi, H. K.; Lee, K. S.; Shin, H. H.; Koo, J. J.; Yeon, G. J.; Kim, Z. H. Single-Molecule Surface-Enhanced Raman Scattering as a Probe of Single-Molecule Surface Reactions: Promises and Current Challenges. *Acc. Chem. Res.* **2019**.

(30) Minamimoto, H.; Toda, T.; Futashima, R.; Li, X.; Suzuki, K.; Yasuda, S.; Murakoshi, K. Visualization of Active Sites for Plasmon-Induced Electron Transfer Reactions Using Photoelectrochemical Polymerization of Pyrrole.

(31) Kazuma, E.; Jung, J.; Ueba, H.; Trenary, M.; Kim, Y. Direct Pathway to Molecular Photodissociation on Metal Surfaces Using Visible Light. *J. Am. Chem. Soc.* **2017**, *139* (8), 3115–3121.

(32) Lather, J.; Bhatt, P.; Thomas, A.; Ebbesen, T. W.; George, J. Cavity Catalysis by Cooperative Vibrational Strong Coupling of Reactant and Solvent Molecules. *Angew. Chemie - Int. Ed.* **2019**, 10635–10638.

(33) Thomas, A.; George, J.; Shalabney, A.; Dryzhakov, M.; Varma, S. J.; Moran, J.; Chervy, T.; Zhong, X.; Devaux, E.; Genet, C.; Hutchison, J. A.; Ebbesen, T. W. Ground-State Chemical Reactivity under Vibrational Coupling to the Vacuum Electromagnetic Field. *Angew. Chemie - Int. Ed.* **2016**, *55* (38), 11462–11466.

(34) 梶川浩太郎; 岡本隆之. プラズモニクスー基礎と応用; 講談社, 2010.

(35) Jackson, J. D. *Classical Electrodynamics*, 3rd ed.; Wiley, 1999.

(36) Castellanos, G. W.; Bai, P.; Gómez Rivas, J. Lattice Resonances in Dielectric Metasurfaces. *J. Appl. Phys.* **2019**, *125* (21).

(37) Hamdad, S.; Diallo, A. T.; Chakaroun, M.; Boudrioua, A. The Role of Rayleigh Anomalies in the Coupling Process of Plasmonic Gratings and the Control of the Emission Properties of Organic Molecules. *Sci. Rep.* **2022**, *12* (1), 1–11.

(38) Kravets, V. G.; Kabashin, A. V.; Barnes, W. L.; Grigorenko, A. N. Plasmonic Surface Lattice Resonances: A Review of Properties and Applications. *Chem. Rev.* **2018**, *118* (12), 5912–5951.

(39) Khlopin, D.; Laux, F.; Wardley, W. P.; Martin, J.; Wurtz, G. A.; Plain, J.; Bonod, N.; Zayats, A. V.; Dickson, W.; Gérard, D. Lattice Modes and Plasmonic Linewidth Engineering in Gold and Aluminum Nanoparticle Arrays. *J. Opt. Soc. Am. B* **2017**, *34* (3), 691.

(40) Li, G. H. Y.; Li, G. Necessary Conditions for Out-of-Plane Lattice Plasmons in Nanoparticle Arrays. *J. Opt. Soc. Am. B* **2019**, *36* (4), 805.

(41) Ashkin, A.; Dziedzic, J. M.; Bjorkholm, J. E.; Chu, S. Observation of a Single-Beam Gradient Force Optical Trap for Dielectric Particles. *Opt. Lett.* **1986**, *11* (5), 288–290.

(42) Misawa, H.; Sasaki, K.; Koshioka, M.; Kitamura, N.; Masuhara, H. Multibeam Laser Manipulation and Fixation of Microparticles. *Appl. Phys. Lett.* **1992**, *60* (3), 310–312.

(43) Dienerowitz, M.; Mazilu, M.; Dholakia, K. Optical Manipulation of Nanoparticles : A Review Optical Manipulation of Nanoparticles : A Review. **2008**, *2* (September), 1–32.

(44) Osborne, M. A.; Balasubramanian, S.; Furey, W. S.; Klenerman, D. Optically Biased Diffusion of Single Molecules Studied by Confocal Fluorescence Microscopy. *J. Phys. Chem. B* **1998**, *102* (17), 3160–3167.

(45) Ashkin, A.; Dziedzic, J. M. Optical Trapping and Manipulation of Viruses and Bacteria. *Science* **1987**, *235* (4795), 1517–1520.

(46) Xu, H.; Käll, M. Surface-Plasmon-Enhanced Optical Forces in Silver Nanoaggregates. *Phys. Rev. Lett.* **2002**, *89* (24), 246802.

(47) Plonsey, R.; Collin, R. E. *Principles and Applications of Electromagnetic Fields*; McGraw-Hill series in electrical engineering: Electromagnetics; McGraw-Hill, 1961.

(48) Grigorenko, A. N.; Roberts, N. W.; Dickinson, M. R.; Zhang, Y. Nanometric Optical Tweezers Based on Nanostructured Substrates. *Nat. Photonics* **2008**, *2* (6), 365–370.

(49) Zhang, W.; Huang, L.; Santschi, C.; Martin, O. J. F. Trapping and Sensing 10 Nm Metal Nanoparticles Using Plasmonic Dipole Antennas. *Nano Lett.* **2010**, *10* (3), 1006–1011.

(50) Urban, A. S.; Carretero-Palacios, S.; Lutich, A. A.; Lohmüller, T.; Feldmann, J.; Jäckel, F. Optical Trapping and Manipulation of Plasmonic Nanoparticles: Fundamentals, Applications, and Perspectives. *Nanoscale* **2014**, *6* (9), 4458.

(51) Berthelot, J.; Acimovic, S. S.; Juan, M. L.; Kreuzer, M. P.; Renger, J.; Quidant, R. Three-Dimensional Manipulation with Scanning near-Field Optical Nanotweezers. *Nat. Nanotechnol.* **2014**, *9* (4), 295–299.

(52) Jiao, J.; Wang, X.; Wackenhut, F.; Horneber, A.; Chen, L.; Failla, A. V.; Meixner, A. J.; Zhang, D. Polarization-Dependent SERS at Differently Oriented Single Gold Nanorods. *Chemphyschem* **2012**, *13* (4), 952–958.

(53) Pang, Y.; Gordon, R. Optical Trapping of a Single Protein. *Nano Lett.* **2012**, *12* (1), 402–406.

(54) Shoji, T.; Kitamura, N.; Tsuboi, Y. Resonant Excitation Effect on Optical Trapping of Myoglobin: The Important Role of a Heme Cofactor. *J. Phys. Chem. C* **2013**, *117* (20), 10691–10697.

(55) Pin, C.; Ishida, S.; Takahashi, G.; Sudo, K.; Fukaminato, T.; Sasaki, K. Trapping and Deposition of Dye–Molecule Nanoparticles in the Nanogap of a Plasmonic Antenna. *ACS Omega* **2018**, *3* (5), 4878–4883.

(56) Kitahama, Y.; Funaoka, M.; Ozaki, Y. Plasmon-Enhanced Optical Tweezers for Single Molecules on and near a Colloidal Silver Nanoaggregate. *J. Phys. Chem. C* **2019**, *123* (29), 18001–18006.

(57) Jensen, R. A.; Huang, I. C.; Chen, O.; Choy, J. T.; Bischof, T. S.; Lončar, M.; Bawendi, M. G. Optical Trapping and Two-Photon Excitation of Colloidal Quantum Dots Using Bowtie Apertures. *ACS Photonics* **2016**, *3* (3), 423–427.

(58) Xu, Z.; Crozier, K. B. All-Dielectric Nanotweezers for Trapping and Observation of a Single Quantum Dot. *Opt. Express* **2019**, *27* (4), 4034–4045.

(59) Djorović, A.; Meyer, M.; Darby, B. L.; Le Ru, E. C. Accurate Modeling of the Polarizability of Dyes for Electromagnetic Calculations. *ACS Omega* **2017**, *2* (5), 1804–1811.

(60) McDonald, P. J.; Korb, J. P.; Mitchell, J.; Monteilhet, L. Surface Relaxation and Chemical Exchange in Hydrating Cement Pastes: A Two-Dimensional NMR Relaxation Study. *Phys. Rev. E - Stat. Nonlinear, Soft Matter Phys.* **2005**, *72* (1).

(61) Nabika, H.; Sasaki, A.; Takimoto, B.; Sawai, Y.; He, S.; Murakoshi, K. Controlling Molecular Diffusion in Self-Spreading Lipid Bilayer Using Periodic Array of Ultra-Small Metallic Architecture on Solid Surface. *J. Am. Chem. Soc.* **2005**, *127* (48), 16786–16787.

(62) Juan, M. L.; Righini, M.; Quidant, R. Plasmon Nano-Optical Tweezers. *Nat. Photonics* **2011**, *5* (6), 349–356.

(63) Huidobro, P. A.; Ota, S.; Yang, X.; Yin, X.; Garcia-Vidal, F. J.; Zhang, X. Plasmonic Brownian Ratchet. *Phys. Rev. B* **2013**, *88* (20).

(64) Motegi, T.; Nabika, H.; Murakoshi, K. Enhanced Brownian Ratchet Molecular Separation Using a Self-Spreading Lipid Bilayer. *Langmuir* **2012**, *28* (16), 6656–6661.

(65) Bjerneld, E. J.; Johansson, P.; Käll, M. Single Molecule Vibrational Fine-Structure of Tyrosine Adsorbed on Ag Nano-Crystals. *Single Mol.* **2000**, *1*, 239–248.

(66) Palma, A.; Baumberg, J. J.; Carnegie, C.; Sigle, D. O.; Scherman, O. A.; de Nijs, B.; Barrow, S. J.; Sundararaman, R.; Kamp, M.; Narang, P.; Chikkaraddy, R.; Benz, F. Plasmonic Tunnel Junctions for Single-Molecule Redox Chemistry. *Nat. Commun.* **2017**, *8* (1), 1–8.

(67) Braun, D.; Libchaber, A. Trapping of DNA by Thermophoretic Depletion and Convection. *Phys. Rev. Lett.* **2002**, *89* (18), 2–5.

(68) Braibanti, M.; Vigolo, D.; Piazza, R. Does Thermophoretic Mobility Depend on Particle Size? *Phys. Rev. Lett.* **2008**, *100* (10), 1–4.

(69) Liu, E.; Li, J.; Jiao, L.; Doan, H. T. T.; Liu, Z.; Zhao, Z.; Huang, Y.; Abraham, K. M.; Mukerjee, S.; Jia, Q. Unifying the Hydrogen Evolution and Oxidation Reactions Kinetics in Base by Identifying the Catalytic Roles of Hydroxyl-Water-Cation Adducts. *J. Am.*

Chem. Soc. **2019**, *141* (7), 3232–3239.

(70) Nie, S.; Emory, S. R. Probing Single Molecules and Single Nanoparticles by Surface-Enhanced Raman Scattering. *Science* **1997**, *275* (5303), 1102–1106.

(71) Kneipp, K.; Wang, Y.; Kneipp, H.; Perelman, L. T.; Itzkan, I.; Dasari, R.; Feld, M. S. Single Molecule Detection Using Surface-Enhanced Raman Scattering (SERS). *Phys. Rev. Lett.* **1997**, *78* (9), 1667–1670.

(72) Le Ru, E. C.; Etchegoin, P. G. Single-Molecule Surface-Enhanced Raman Spectroscopy. *Annual review of physical chemistry*. 2012, pp 65–87.

(73) Dodson, S.; Haggui, M.; Bachelot, R.; Plain, J.; Li, S.; Xiong, Q. Optimizing Electromagnetic Hotspots in Plasmonic Bowtie Nanoantennae. *J. Phys. Chem. Lett.* **2013**, *4* (3), 496–501.

(74) Wu, D.-Y.; Li, J.-F.; Ren, B.; Tian, Z.-Q. Electrochemical Surface-Enhanced Raman Spectroscopy of Nanostructures. *Chem. Soc. Rev.* **2008**, *37* (5), 1025.

(75) Zhao, L. L.; Jensen, L.; Schatz, G. C. Pyridine-Ag20 Cluster: A Model System for Studying Surface-Enhanced Raman Scattering. *J. Am. Chem. Soc.* **2006**, *128* (9), 2911–2919.

(76) Morton, S. M.; Jensen, L.; Park, U. V; Pennsyl, V. Understanding the Molecule - Surface Chemical Coupling In. **2009**, No. 23, 4090–4098.

(77) Seth Michael Morton, E. E.-A. and L. J.; Lee, T. R.; Lecomte, S.; De, M. A.; Hildebrandt, P.; Murgida, D. H.; Chem, P.; Tognalli, N. G.; Scodeller, P.; Flexer, V.; Ricci, A.; Tagliazucchi, M.; Calvo, E. J.; Morton, S. M.; Ewusi-annan, E.; Jensen, L.; Soto, J.; Ribeiro-claro, P.; Otero, J. C. Controlling the Non-Resonant Chemical Mechanism of SERS Using a Molecular Photoswitch. *Phys. Chem. Chem. Phys.* **2009**, *11* (34), 7348.

(78) Valley, N.; Greeneltch, N.; Van Duyne, R. P.; Schatz, G. C. A Look at the Origin and Magnitude of the Chemical Contribution to the Enhancement Mechanism of Surface-Enhanced Raman Spectroscopy (SERS): Theory and Experiment. *J. Phys. Chem. Lett.* **2013**, *4* (16), 2599–2604.

(79) Jensen, L.; Zhao, L. L.; Schatz, G. C. Size-Dependence of the Enhanced Raman Scattering of Pyridine Adsorbed on Ag n (N= 2 - 8 , 20) Clusters. *J. Phys. Chem. C* **2007**, *111*, 4756–4764.

(80) Wu, D. Y.; Li, J. F.; Ren, B.; Tian, Z. Q. Electrochemical Surface-Enhanced Raman Spectroscopy of Nanostructures. *Chem. Soc. Rev.* **2008**, *37* (5), 1025–1041.

(81) Kale, M. J.; Avanesian, T.; Xin, H.; Yan, J.; Christopher, P. Controlling Catalytic Selectivity on Metal Nanoparticles by Direct Photoexcitation of Adsorbate-Metal Bonds. *Nano Lett.* **2014**, *14* (9), 5405–5412.

(82) Gieseking, R. L.; Ratner, M. A.; Schatz, G. C. Theoretical Modeling of Voltage Effects

and the Chemical Mechanism in Surface-Enhanced Raman Scattering. *Faraday Discuss.* **2017**, *205*, 149–171.

(83) Gieseking, R. L. M.; Lee, J.; Tallarida, N.; Apkarian, V. A.; Schatz, G. C. Bias-Dependent Chemical Enhancement and Nonclassical Stark Effect in Tip-Enhanced Raman Spectromicroscopy of CO-Terminated Ag Tips. *J. Phys. Chem. Lett.* **2018**, *9* (11), 3074–3080.

(84) 濱口宏夫 平川暁子. ラマン分光法. 学会出版センター **1988**, 1988.

(85) Lombardi, J. R.; Birke, R. L.; Lu, T.; Xu, J. Charge-Transfer Theory of Surface Enhanced Raman Spectroscopy: Herzberg-Teller Contributions. *Journal of Chemical Physics*. 1986, pp 4174–4180.

(86) Albrecht, A. C. On the Theory of Raman Intensities. *J. Chem. Phys.* **1961**, *34* (5), 1476–1484.

(87) Lombardi, J. R.; Birke, R. L. A Unified Approach to Surface-Enhanced Raman Spectroscopy. *J. Phys. Chem. C* **2008**, *112* (14), 5605–5617.

(88) Lombardi, J. R.; Birke, R. L. A Unified View of Surface-Enhanced Raman Scattering. *Acc. Chem. Res.* **2009**, *42* (6), 734–742.

(89) Chen, Y. X.; Zou, S. Z.; Huang, K. Q.; Tian, Z. Q. SERS Studies of Electrode/Electrolyte Interfacial Water Part II—Librations of Water Correlated to Hydrogen Evolution Reaction. *J. Raman Spectrosc.* **1998**, *29* (8), 749–756.

(90) Luo, Z.; Loo, B. H.; Cao, X.; Peng, A.; Yao, J. Probing the Conformational Transition of 2,2′-Bipyridyl under External Field by Surface-Enhanced Raman Spectroscopy. *J. Phys. Chem. C* **2012**, *116* (4), 2884–2890.

(91) Wandlowski, T.; Ataka, K.; Mayer, D. In Situ Infrared Study of 4,4′-Bipyridine Adsorption on Thin Gold Films. *Langmuir* **2002**, *18* (11), 4331–4341.

(92) Brolo, A. G.; Irish, D. E.; Szymanski, G.; Lipkowski, J. Relationship between SERS Intensity and Both Surface Coverage and Morphology for Pyrazine Adsorbed on a Polycrystalline Gold Electrode. *Langmuir* **1998**, *14* (2), 517–527.

(93) Zong, D.; Hu, H.; Duan, Y.; Sun, Y. Viscosity of Water under Electric Field: Anisotropy Induced by Redistribution of Hydrogen Bonds. *J. Phys. Chem. B* **2016**, *120* (21), 4818–4827.

(94) Velasco-Velez, J. J.; Wu, C. H.; Pascal, T. A.; Wan, L. F.; Guo, J.; Prendergast, D.; Salmeron, M. The Structure of Interfacial Water on Gold Electrodes Studied by X-Ray Absorption Spectroscopy. *Science* **2014**, *346* (6211), 831–834.

(95) Li, C. Y.; Le, J. B.; Wang, Y. H.; Chen, S.; Yang, Z. L.; Li, J. F.; Cheng, J.; Tian, Z. Q. In Situ Probing Electrified Interfacial Water Structures at Atomically Flat Surfaces. *Nat.*

Mater. **2019**, *18* (7), 697–701.

(96) Marković, N. M.; Grgur, B. N.; Ross, P. N. Temperature-Dependent Hydrogen Electrochemistry on Platinum Low-Index Single-Crystal Surfaces in Acid Solutions. *J. Phys. Chem. B* **1997**, *101* (27), 5405–5413.

(97) Ishikawa, Y.; Mateo, J. J.; Tryk, D. A.; Cabrera, C. R. Direct Molecular Dynamics and Density-Functional Theoretical Study of the Electrochemical Hydrogen Oxidation Reaction and Underpotential Deposition of H on Pt(1 1 1). *J. Electroanal. Chem.* **2007**, *607* (1–2), 37–46.

(98) Roger, I.; Shipman, M. A.; Symes, M. D. Earth-Abundant Catalysts for Electrochemical and Photoelectrochemical Water Splitting. **2017**.

(99) Tong, W.; Forster, M.; Dionigi, F.; Dresp, S.; Erami, R. S.; Strasser, P.; Cowan, A. J.; Farràs, P. Electrolysis of Low-Grade and Saline Surface Water. **2020**, *5* (May), 367–377.

(100) Mccrory, C. C. L.; Jung, S.; Ferrer, I. M.; Chatman, S. M.; Peters, J. C.; Jaramillo, T. F. Benchmarking Hydrogen Evolving Reaction and Oxygen Evolving Reaction Electrocatalysts for Solar Water Splitting Devices. **2015**.

(101) Conway, B. E.; O'M Bockris, J. Electrolytic Hydrogen Evolution Kinetics and Its Relation to the Electronic and Adsorptive Properties of the Metal. *The Journal of Chemical Physics*. 1957, pp 532–541.

(102) Topley, B.; Eyring, H. The Separation of the Hydrogen Isotopes by Electrolysis. Part I. *J. Chem. Phys.* **1934**, *2* (5), 217–230.

(103) Trasatti, S. Work Function, Electronegativity, and Electrochemical Behaviour of Metals. III. Electrolytic Hydrogen Evolution in Acid Solutions. *J. Electroanal. Chem.* **1972**, *39* (1), 163–184.

(104) Shinagawa, T.; Garcia-Esparza, A. T.; Takanabe, K. Insight on Tafel Slopes from a Microkinetic Analysis of Aqueous Electrocatalysis for Energy Conversion. *Sci. Rep.* **2015**, *5* (May), 1–21.

(105) Bockris, J. O.; Srinivasan, S. Theoretical Calculations of the Separation Factors in the Hydrogen Evolution Reaction for the Slow Recombination Mechanism. *J. Electrochem. Soc.* **1964**, *111* (7), 858.

(106) Lozada-Hidalgo, M.; Hu, S.; Marshall, O.; Mishchenko, A.; Grigorenko, A. N.; Dryfe, R. A. W.; Radha, B.; Grigorieva, I. V.; Geim, A. K. Sieving Hydrogen Isotopes through Two-Dimensional Crystals. *Science* **2016**, *351* (6268), 68–70.

(107) Zhou, X.; Wang, L.; Fan, X.; Wilfong, B.; Liou, S. C.; Wang, Y.; Zheng, H.; Feng, Z.; Wang, C.; Rodriguez, E. E. Isotope Effect between H2O and D2O in Hydrothermal Synthesis. *Chem. Mater.* **2020**, *32* (2), 769–775.

(108) Cai, S.; Bai, T.; Chen, H.; Fang, W.; Xu, Z.; Lai, H.; Huang, T.; Xu, H.; Chu, X.; Ling, J.;

Gao, C. Heavy Water Enables High-Voltage Aqueous Electrochemistry via the Deuterium Isotope Effect. *J. Phys. Chem. Lett.* **2020**, *11* (1), 303–310.

(109) Haynes, W. M. *CRC Handbook of Chemistry and Physics*, 95th ed.; CRC Press: Hoboken, 2014.

(110) Eisenberg, D. S.; Kauzmann, W. *The Structure and Properties of Water*; Oxford University Press, 1969.

(111) Auer, B. M.; Skinner, J. L. IR and Raman Spectra of Liquid Water: Theory and Interpretation. *J. Chem. Phys.* **2008**, *128* (22).

(112) Kato, F.; Sugimoto, T.; Harada, K.; Watanabe, K.; Matsumoto, Y. Unveiling Two Deuteration Effects on Hydrogen-Bond Breaking Process of Water Isotopomers. *Phys. Rev. Mater.* **2019**, *3* (11), 1–7.

(113) Lu, T.; Cotton, T. M.; Birke, R. L.; Lombardi, J. R. Raman and Surface-Enhanced Raman Spectroscopy of the Three Redox Forms of 4,4′-Bipyridine. *Langmuir* **1989**, *5* (2), 406–414.

(114) Li, C.-Y.; Le, J.-B.; Wang, Y.-H.; Chen, S.; Yang, Z.-L.; Li, J.-F.; Cheng, J.; Tian, Z.-Q. In Situ Probing Electrified Interfacial Water Structures at Atomically Flat Surfaces. *Nat. Mater.* **2019**, *18* (7), 697–701.

(115) Wang, Y. H.; Zheng, S.; Yang, W. M.; Zhou, R. Y.; He, Q. F.; Radjenovic, P.; Dong, J. C.; Li, S.; Zheng, J.; Yang, Z. L.; Attard, G.; Pan, F.; Tian, Z. Q.; Li, J. F. In Situ Raman Spectroscopy Reveals the Structure and Dissociation of Interfacial Water. *Nature* **2021**, *600* (7887), 81–85.

(116) Li, J. F.; Anema, J. R.; Yu, Y. C.; Yang, Z. L.; Huang, Y. F.; Zhou, X. S.; Ren, B.; Tian, Z. Q. Core-Shell Nanoparticle Based SERS from Hydrogen Adsorbed on a Rhodium(111) Electrode. *Chem. Commun.* **2011**, *47* (7), 2023–2025.

(117) Jiang, Y. X.; Li, J. F.; Wu, D. Y.; Yang, Z. L.; Ren, B.; Hu, J. W.; Chow, Y. L.; Tian, Z. Q. Characterization of Surface Water on Au Core Pt-Group Metal Shell Nanoparticles Coated Electrodes by Surface-Enhanced Raman Spectroscopy. *Chem. Commun.* **2007**, No. 44, 4608–4610.

(118) Li, J. F.; Huang, Y. F.; Duan, S.; Pang, R.; Wu, D. Y.; Ren, B.; Xu, X.; Tian, Z. Q. SERS and DFT Study of Water on Metal Cathodes of Silver, Gold and Platinum Nanoparticles. *Phys. Chem. Chem. Phys.* **2010**, *12* (10), 2493–2502.

(119) Ranea, V. A.; Michaelides, A.; Ramírez, R.; Vergés, J. A.; De Andres, P. L.; King, D. A. Density Functional Theory Study of the Interaction of Monomeric Water with the Ag{111} Surface. *Phys. Rev. B - Condens. Matter Mater. Phys.* **2004**, *69* (20), 1–9.

(120) Pang, R.; Zhang, X. G.; Zhou, J. Z.; Wu, D. Y.; Tian, Z. Q. SERS Chemical Enhancement of Water Molecules from Halide Ion Coadsorption and Photoinduced Charge Transfer on

Silver Electrodes. *J. Phys. Chem. C* **2017**, *121* (19), 10445–10454.

(121) Takahashi, Y.; Kobayashi, Y.; Wang, Z.; Ito, Y.; Ota, M.; Ida, H.; Kumatani, A.; Miyazawa, K.; Fujita, T.; Shiku, H.; Korchev, Y. E.; Miyata, Y.; Fukuma, T.; Chen, M.; Matsue, T. High-Resolution Electrochemical Mapping of the Hydrogen Evolution Reaction on Transition-Metal Dichalcogenide Nanosheets. *Angew. Chemie Int. Ed.* **2020**, *59* (9), 3601–3608.

(122) Shin, D.; Hwang, J.; Jhe, W. Ice-VII-like Molecular Structure of Ambient Water Nanomeniscus. *Nat. Commun.* **2019**, *10* (1), 1–8.

Chapter 2

2D-difussion modulation on plasmonic arrays

2.1 Introduction

In various scientific interests such as molecular catalytic processes, [1] biological activity, [1] and crystalline growth technology,[2] the precise manipulation of targets at the interface is an important issue. Very small molecules with a few amounts, however, are difficult to detect in a conventional way, especially at interfacial regions which are known as the Langmuir layer or the Helmholtz layer. One of the tools to visualize their translational motion and vibrational motion in the vicinity of the surface is Raman scattering measurement supported by plasmon-excitation called as surface-enhanced Raman scattering measurement (SERS).[3] Recently, various SERS observations have achieved the single-molecule detection. The mechanism of the SERS, i.e. the enhancement of the electromagnetic field induced by the excitation of the localized surface plasmon resonance (LSPR) at the metal nano-structures, is well recognized and applied to various fields.[4] It has been known that the electromagnetic field confined in the vicinity of nanostructures can be up to 10^4 to 10^5 times higher than incident light.[5] Therefore, I have not only tried to optimize the SERS observation technique to follow the real 2D diffusion motion of tiny molecules and but also to evaluate the key factors of molecular motion in the plasmon field of Au nanostructure at room temperature.

2.2 Experimental method

2.2.1 Raman optical measurement combined electrochemical cell

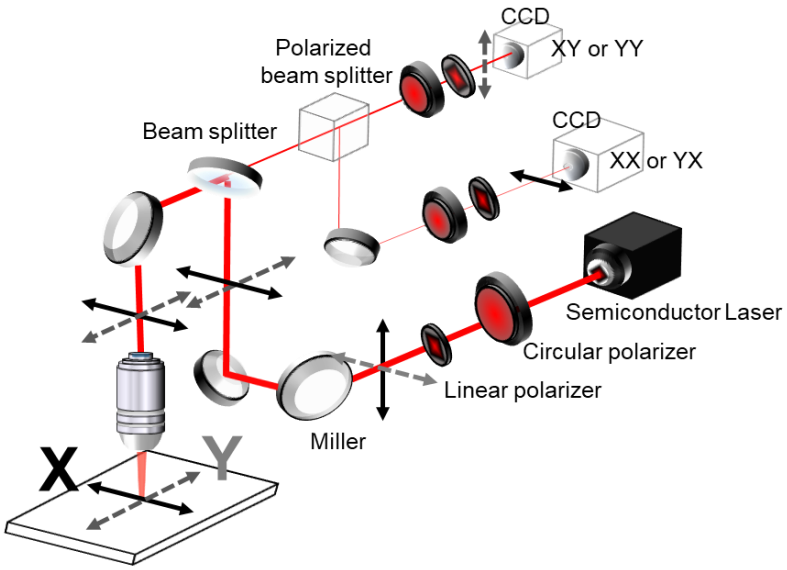

Figure 2-1. Polarization Raman Scattering spectroscopy set up. Main measurements were done with Z(XX)Z incident polarized light.

A schematic diagram of the linearly polarized Raman scattering measurement system is shown in Figure 2-1. In the experimental set up, circular polarization is converted to linear polarization by a polarizer, and the incident polarized light on the stage is defined as X polarization and Y polarization by rotating the polarizer. Scattered light from X polarization was separated to parallel to incident light as XX polarization and perpendicular to the incident light as XY polarization, thus obtaining two types of spectra for one incident polarization. Similarly, the light scattered parallel to the incident light with Y polarization was defined as YY polarization while the light scattered perpendicular to the incident light was designated as YX polarization. Due to the specifications of the equipment, the ratio of each polarization for elastic scattering in this experimental setup is expressed as follows.

XX: XY: YX: YY = 72: 100: 25: 35 (Equation 2-1)

The polarized Raman measurement is conduced as this condition with excitation laser: 785 nm continuous wave, acquisition time (t_{ex}): 1-30 s, number of acquisitions 1-120 times, excitation light: 0.25- 32 mW, objective lens: immersion lens x100 with N.A.=1.00 and WD=1.5 mm (OLYMPUS), laser spot size at glass/liquid interface: up to 3μm.

In the following experiments, the incident laser intensities were divided by the laser spot and expressed as light intensity per unit area (I_{ex}): 35 / 70 / 140 / 1400 / 4480 μW μm^{-2}. For the electrochemical SERS measurements, I used the homemade three electrodes electrochemical Raman cell as illustrated in Figure 2-2. As the substrates, the plasmonic structures were fabricated on the entire surface of the indium tin oxide (ITO) conductive glass substrate using angle-resolved nano-sphere lithography method.[6] In the case of electrochemical measurement, substrates are set to working electrode (WE) with Pt wire as counter electrode (CE) and Ag/AgCl filled capillary as reference electrode (RE).

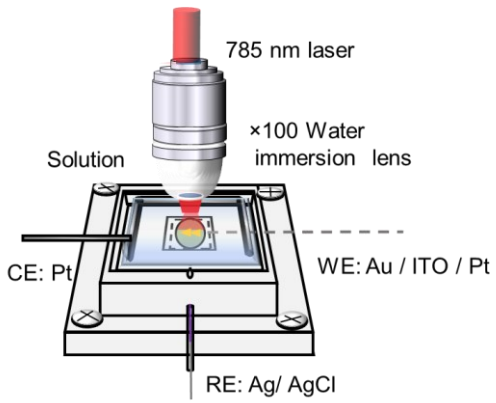

Figure 2-2. Schematic illustration of three electrodes electrochemical cell with NIR (λ=785nm) laser. The WE is prepared nano structure on ITO connected to Pt wire out of solution. The CE is Pt plate and the RE is Ag / AgCl with saturated KCl liquid junction.

2.2.2 Angle-resolved nanosphere lithography (AR-NSL)

A 400 μL solution of polystyrene beads (Polyscience, Inc.) approximately 200 nm in diameter was centrifuged and purified by removing the supernatant. Then 100 μL of Mill-Q water and 150 μL of ethanol were added and mixed. When this prepared solution was dropped into a Petri dish filled with water, the self-assembled monolayer was aggregated on the water surface. When the ITO glass was placed in the petri dish, the self-assembled monolayer was dried on the ITO surface as the water drained off. The Au nanoprism array substrate was formed by electron beam deposition of Au on the periodic vacancy of polystyrene beads in a vacuum chamber (ULVAC, Inc.). The deposition condition was Au thickness of 30 nm on +10 º tilt stage and deposition of 30 nm on −10 º tilt stage under deposition rate: 0.20 nm s^{-1}. After deposition, all polystyrene beads were removed by sonication in water. The Au nanoprism array structure was optimized to absorb light at 785 nm as a dimer shape by angle-resolved deposition. The structures were evaluated using an extinction spectrometer and atomic force microscopy (AFM, XE-7, Park Systems).

2.2.3 Solution preparation for molecular manipulation system

In order to reveal the 2D diffusion process in the plasmonic field, different solutions were used in the SERS measurement. The bipyridine and its analogs have good stability in various solvents and well known physical adsorption properties, where the adsorption isotherm on Au surface follows typical theory such as Langmuir or Temkin model.[7,8] Moreover, bipyridine structure isomers called as 4,4’-bipyridine (44bpy) and

2,2'-bipyridine (22bpy) have relatively high Raman activity in experimental conditions even though there is no adsorption band in the visible region. [10– 12] All of the solutions were prepared as in Table 2-1. I abbreviate each component as like follows, 4,4'-dimethyl -2,2'-bipyridine (44DMe22bpy), 4,4'-di-tert-butyl -2,2'-bipyridine (44DTBu22bpy), 4,4'-diamino -2,2'-bipyridine (44DA22bpy), 6,6'-diamino-2,2'-bipyridine (66DA22bpy), 6-amino -2,2'-bipyridine (6A22bpy), N, N'-dimethylformamide (DMF), acetonitrile (AN), isopropanol (IPA), n-hexane (Hex).

Table 2-1: Solution preparation for Raman measurement

Factor	Solvent	Molecule (1 mM)	$NaClO_4$ [mM]
Solvent	H_2O	44bpy	w/o
	DMF	44bpy	w/o
	AN	44bpy	w/o
	IPA	44bpy	w/o
	Hex	44bpy	w/o
Electrolyte	H_2O	44bpy	50
	H_2O	44bpy	100
	H_2O	44bpy	500
	H_2O	44bpy	1000
	AN	44bpy	100
	AN	44bpy	500
	AN	44bpy	1000
Molecules	AN	22bpy	100
	AN	44bpy	100
	AN	44DMe22bpy	100
	AN	44DTBu22bpy	100
	AN	44DA22bpy	100
	AN	66DA22bpy	100
	AN	66A22bpy	100

The basic physical properties of the solvents used in this study are shown in Table 2-2. Most of these solvents have a refractive index relatively close to the refractive index(n) of H_2O in the visible range as 1.33, while there is a good variety of dipole moment(μ), boiling point (b. p.), viscosity (η), and thermal conductivity (σ).

Table 2-2. Physical and thermal properties of pure solvents by literature

Solvent	μ [D]	b. p. [°C]	n [-] [b]	η at 298 K [mPa s^{-1}] [c]	σ at 298 K [W m^{-1} K^{-1}]
H_2O	1.85[12]	100[13]	1.33[14]	0.89[15]	0.606[16]
DMF	3.77 [a]	153[13]	1.43[17]	0.93[18]	0.187[19]
AN	3.61 [a]	82[13]	1.34[20]	0.35[21]	0.183[22]
IPA	1.75 [a]	83[13]	1.37[20]	2.01[23]	0.132[24]
Hex	0.00 [a]	60[13]	1.37[20]	0.31[25]	0.116[26]

a: Calculated value (gaussian16, DFT_B3LYP), b: refractive index in 500~700 nm light

2.3 Results and discussion

2.3.1 Optical mode of plasmonic arrays

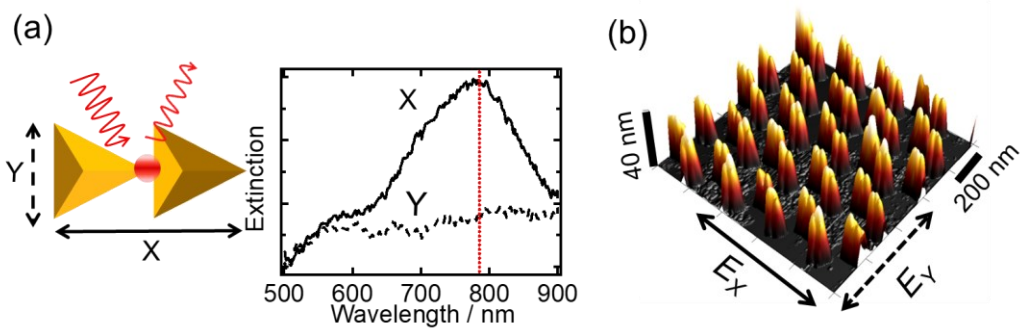

Figure 2-3. (a) Incident polarized light extinction spectra were obtained from Au dimer nanoprism array on ITO glass in the air. The broken and solid lines represent the X and Y polarizations, respectively. The vertical broken line at 785 nm corresponds to the laser wavelength for Raman measurements. (b) AFM image of Au dimer nanoprism array on ITO glass was displayed as a 3D perspective view.

The Au dimer nanoprism array substrate was analyzed by polarization dependence of extinction spectra and AFM measurements. From the extinction spectra, a certain peak of localized plasmon resonance was observed at around 785 nm under the illumination of light polarized to the long axis of the dimer shapes. By optimizing the LSPR with the excitation laser of the Raman setup, the *in-situ* observation system of molecular motion on the Au surface under ambient conditions was achieved.

2.3.2 Spectroscopic identification of adsorbed molecules by SERS

At first, I compared the Raman spectra of 44bpy and 22bpy, structure isomers, as crystalline phase and solution phase with/without Au dimer nanoprism arrays in water. Since Raman scattering is inelastic scattering originating from molecular vibration, the spectra show multiple vibration modes reflecting the symmetry of the vibration and the

scattering cross section. In the case of single crystal powder, the spectra were less dependent on the incident or scattering polarization as shown in Figs. 2-4a and d, because of the multiple scattering by the crystal particles in all scattering directions. On the other hand, since the scattering from diffusing molecules in solution depends on the scattering cross section for each vibration, usual depolarization ratio takes within 0~0.75 (Figure2-4b, e). The assignments of each band are given in Table 2-3.

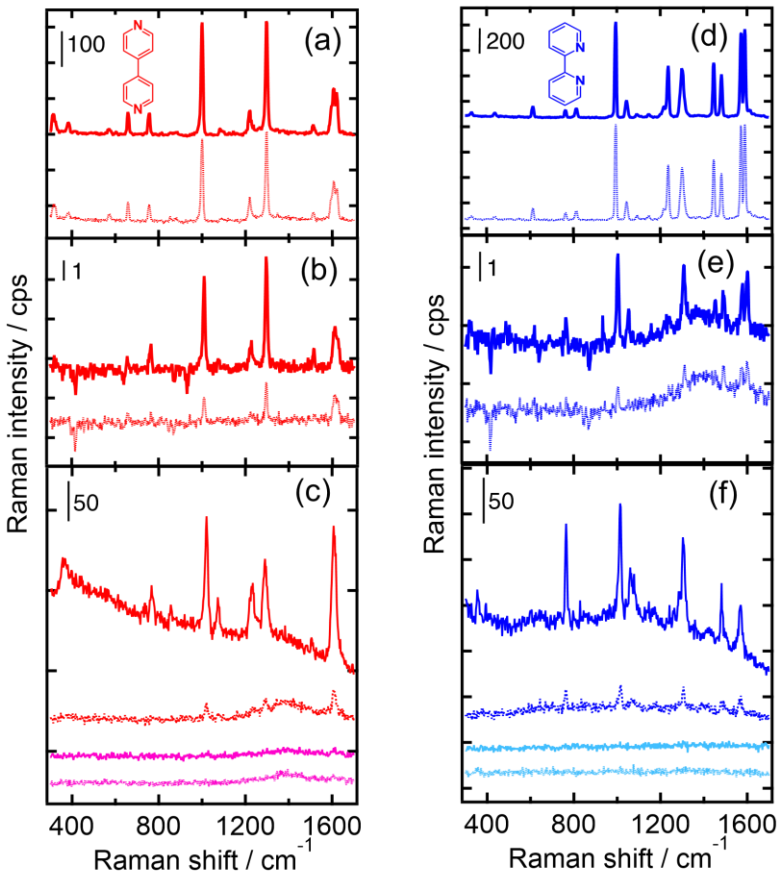

Figure 2-4. Raman spectra of (a, b, c) 44bpy or (d, e, f) 22bpy as (a, d) powder sample (t_{ex}: 1 sec. I_{ex}: 1400 μW μm^{-2}), (b, e) 10 mM concentration aq. with 0.1 M $NaClO_4$ (t_{ex}: 300 s. I_{ex}: 4480 μW μm^{-2}), and (c,f) 1 mM concentration aq.with 0.1 M $NaClO_4$ on the Au dimer nanoprism array (t_{ex}: 1 sec. I_{ex}: (c) 140 μWμm^{-2} or (f) 70 μW μm^{-2}). Solid lines are obtained from X-polarized scattering expressed as Z(XX)Z, and broken lines from Y-polarized scattering expressed as Z(XY)Z, while in bottom panels pink lines are corresponding to X-polarized incident light expressed as Z(Y-)Z.

Table 2-3. Raman band assignment (cm^{-1}) of 44bpy and 22bpy from experiment and references

Powder	SERS exp.	SERS ref.	Vibrational mode
44bpy		Au spheres[10]	
659	-	-	In-plane ring def.
755	-	766	Ring breathing
	790	856	C-H out-of-plane def.
997	1020	1017	Ring breathing
1084	1073	1080	In-plane ring def. + C-H def.
1219	1230	1227	C-H in-plane def.
1293	1295	1293	C-C inter-ring str.
1508	-	1510	Ring str. (C-C, C-N) + C-H in-plane bending
1607	1608	1608	Ring str. (C-C, C-N)
22bpy		Au crystal[9]	
613	650	649	In-plane ring def.
770	764	765	In plane ring def.
818	-	-	C-H out-of-plane def.
1000	1013	1013	Ring breathing
1050	-	1061	Ring breathing
	1172	1178	Ring str. + ring def. +C-H in-plane def.
1242	1275	-	Ring str. + C-C inter-ring str. + C-H in-plane def.
1306	1303	1306	C-C inter-ring str. + ring str.+ C-H in-plane def.
1453	-	-	Ring str. (C-C, C-N) + C-H in-plane def.
1486	1482	1484	Ring str.+ in-plane bending
1576	1572	1565	Ring str. (C-C, C-N)
1594	1600	1593	Ring str. + N-H in-plane def.

str.: stretching, def.: deformation.

In the case for SERS measurements using molecules adsorbed on metal nanostructures, the scattering vibrations are strongly linked to electromagnetic and chemical enhancement. Since the special anisotropy of molecular polarizability is determined by the adsorbed orientation, the apparent vibration modes are excited by the electric field coupled with plasmon, where an electric field is spatially distributed unlike

a homogeneous electric field of propagating light. Furthermore, on spatially anisotropic structures, where the plasmon resonance is excited with the polarized direction, the electric field enhancement at the incident and scattered polarization is only observed in a specific direction as shown in Figure 2-4c, f. SERS intensity is sensitive not only to the scattered polarization but also to the incident polarization, resulting in only scattering with the direction parallel to the dimer structure. It should be noted, however, that the light intensity at incident Y-polarization light is reduced by a factor of three in this optical system. Even in that case, SERS spectra were hardly observed for the excitation by Y-polarization. Therefore, it became possible to understand the molecular behavior under 2D-diffusion on metal surfaces for both 44bpy and 22bpy and other analogs through identifications of Raman spectral vibration.

2.3.3 Solvent and electrolyte dependence of interfacial molecular motion

SERS intensity of 44bpy in aqueous solution could be considered as adsorbed 44bpy at the metal surface because the spectrum is different from the solution phase and enormously enhanced by about 10^6 times than normal Raman spectra as shown in previous section with Figure 2-4. Therefore, by following the intensity changes over time, average molecular numbers under surface diffusion become obvious through Raman spectral series, such as fluctuations or decreases in intensity as a function of illumination time.[27] Here, I attempted to distinguish the diffusion behavior of 44bpy in the five solvents under illumination on the plasmonic substrate.

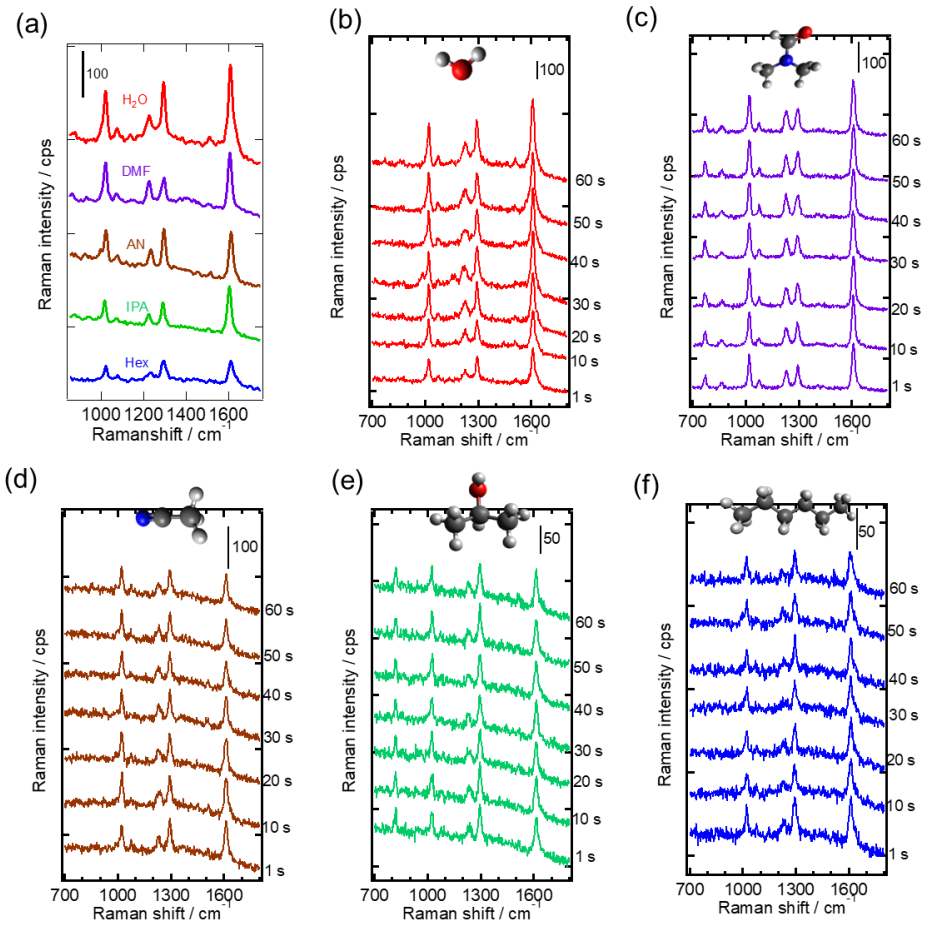

Figure 2-5. SERS spectra of 1mM 44bpy in various solvents with Au dimer nanoprism array. All spectra are obtained with 1 s under I_{ex}: 140 μW μm^{-2} at room temperature. (a) The spectra of each solution at with 1 s exposure are colored red, purple, brown, green or blue from top to down, which is H_2O, DMF, AN, IPA, or Hex, respectively. Inset figures show molecular structure. (b-f) Time-series SERS spectra under 60 s continuous illumination with t_{ex}: 1 s are taken in each solution with different solvents: (b) H_2O, (c) DMF, (d) AN, (e) IPA, and (f) Hex.

Upon initial illumination of the substrate, there is a variation for SERS intensity in different solvents as shown in Figure 2-5a, where H_2O appeared particularly strong, followed by DMF, AN, and then IPA and hexane, in that order. These initial state intensity distributions are correlated with surface coverage as discussed below. Figure 2-5b-c shows the SERS spectra obtained from 44bpy on Au dimer nanoprism array in various solvents. It can be seen that SERS spectra monotonically increase in time from 1 s to 60

s for H_2O, while the stable intensity was confirmed during laser illumination in others. This is considered as that the total amount of molecules through 2D-Diffusion in plasmonic field was effectively increased under illumination only in H_2O.

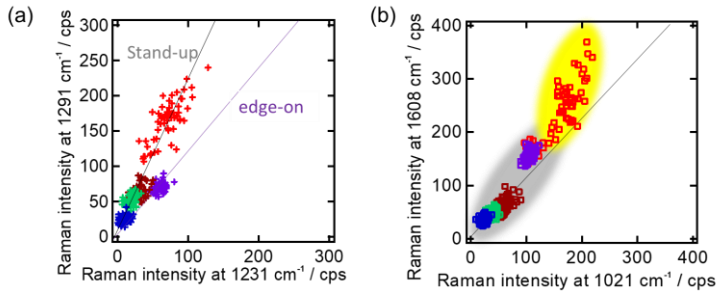

Figure 2-6. Intensity correlation plots are made by peaks at (a) 1231 cm^{-1} vs. 1291 cm^{-1} and (b) at 1021 cm^{-1} and 1608 cm^{-1} from background subtracted SERS spectra of 1mM 44bpy in various solvents with Au dimer nanoprism array in Figure 2-5 with same color manner for solvents: red as H_2O, purple as DMF, brown as AN, green as IPA, and blue (f) Hex. Colored lines represent extrapolation line for edge-on orientation as grey and flat-on as purple. Black line and shaded area stable region for some solvents while yellow region corresponding condensed case in H_2O.

Peak intensity ratio of SERS spectra is defined by adsorption orientation corresponding to Raman tensor shown in Equation 1-14.[28] For analysis of molecular orientation, the peak intensity ratio plot, called correlation plot, between the intensity at 1231 and 1291 cm^{-1} and 1021 and 1608 cm^{-1} are made for five solutions. Special attention should be paid to the ratio of 1231 and 1291 cm^{-1} in different solutions as in Figure 2-6a, because the intensity ratio of these is mainly due to the molecular orientation. [29] The correlation plot in DMF looks like a relatively smaller slope or tilted orientation than others while other solutions gave almost the same slope value assigned as a stand-up orientation to Au surface. Moreover, by the correlation between 1021 and 1608 cm^{-1} in Figure 2-6b, the 44bpy in H_2O shows the rise of its slope in illumination, in other words, the condensation of adsorbed 44bpy modulated the vibrational motion via domain formation or molecular interaction, triggered by a plasmon-enhanced electric field.

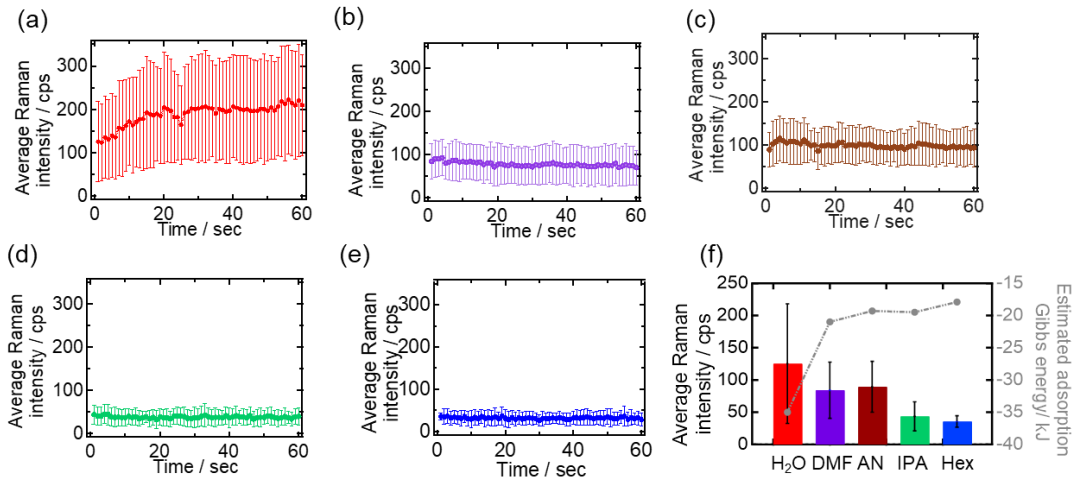

Figure 2-7. SERS spectral intensity at 1608 cm $^{-1}$ of 1 mM 44bpy in various solvents with Au dimer nanoprism array. All original spectra are obtained under I_{ex}: 140 μW μm^{-2} at room temperature. (a-e) Average Raman intensity plot at 1608 cm^{-1} is plotted as a function of time which each sample number is more than 5 trials with standard deviation. These plots are colored with red, purple, brown, green and blue for H_2O, DMF, AN, IPA, and Hex, respectively. (f) Average spectral intensity and deviation at 1 s of each solution with more than 5 trials are extracted from intensity plot with same manner as plot color of (a-e). Grey circles show the estimated adsorption Gibbs energy of 44bpy in each solvent from SERS intensity.

Considering the different solvents, the initial adsorption amount can be listed by the difference in solvation energy based on the comparison of the initial SERS intensities in Figure 2-7. Here, considering the Temkin-model adsorption isotherm,[7]

$$\frac{\theta}{1-\theta}\exp(-2\alpha\theta) = \exp(-\Delta G^0/RT)a_{sol} \qquad \text{(Equation 2-2)}$$

where each is defined as $G^0 = \bar{\mu}^0_{ads} - \bar{\mu}^0_{sol}$, $a_{sol} = c_{44bpy}/c_{solvent}$, and α=1.3, respectively. The coverage of 1 mM 44bpy on the gold surface in water is estimated to be 99.7%. Based on this coverage, the coverage in each solvent can be roughly estimated from the ratio of SERS intensities: 67% in DMF, 71% in AN, 35% in IPA, 28% in Hex. From these intensities as surface coverage, since the surface coverage of 44bpy is strongly dependent on solvation, this can be attributed to the fact that 44bpy is more stabilized by solvation in organic solvents than in water or the Gibbs energy change upon adsorption

is smaller. [31, 32] The saturation position of the increase in SERS intensity in water is 99.7% × (210/125) = 167 %, which predicts that optical molecular condensation also reduces the intermolecular distance or disorder as domain parts, resulting in a high density above the expected coverage of the Temkin model. This is correlated with the increase in the Raman intensity at 1608 cm^{-1} relative to the intensity at 1021 cm^{-1} discussed in Figure 2-6 during illumination. It is also caused by molecular interaction between adsorbed 44bpys, which is why condensation behavior is only observed in H_2O, otherwise, they are almost stable. Note that the intensity deviation is also larger in H_2O than in other solvents since the condensation of 44bpy is mainly the result of modulated balance of motions associated with thermal fluctuations and Brownian motion as lateral hopping at the interface.

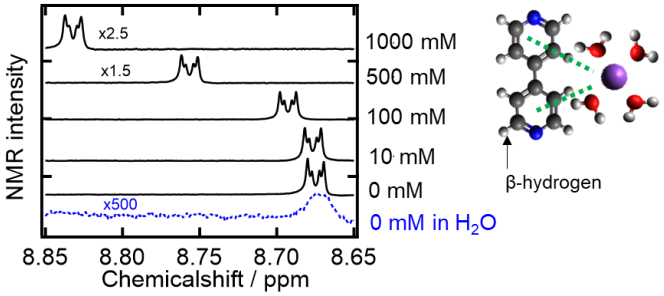

Figure 2-8. Chemical shit spectra (black) of β -hydrogen of 44bpy are measured by NMR in D_2O with different $NaClO_4$ concentration; 0, 10, 100, 500, 1000 mM from bottom to top. These solutions prepared as adding 50 μL TMS to 450 μL of 1 mM 44bpy containing $NaClO_4$ D_2O solution. The bottom blue spectrum of 1 mM 44bpy containing $NaClO_4$ H_2O solution has very low signal. Inset figure shows the scheme of solved 44bpy and Na^+.

Since there may also be solution differences in the interactions of 44bpy at the interface, we examine this intermolecular interaction as a function of salt concentration. To verify the interaction of 44bpy and $NaClO_4$ in solution, I checked the chemical shift by NMR with a variety of electrolyte concentrations. Figure 2-8 shows that the amount of Na^+ bound to 44bpy changes linearly with the salt concentration in the D_2O without

any isolated 44bpy. The electrostatic interaction of Na^+ ions with aromatic rings, especially when they have electron-donating groups, is called "cation-π interaction," which causes a Gibbs energy change, e.g. −28 kJ mol^{-1} for Na^+ and benzene. [32-33] In the present system, Na^+ is expected to bridge the 44bpy, which is thought to further stabilize the addition at the interface.

The molecular aggregation behavior changed with increasing salt concentration. The average Raman intensities achieved maximum at 100 mM in both H_2O and AN as in Figure 2-9a, b. This result suggests that the molecular aggregation process is determined in both the form of optical modulation of 2D-diffusion and intermolecular attraction. However, in the region of even higher salt concentrations, it was no longer possible to condense the molecules. This phenomenon is thought to be that the binding of cation to 44bpy adds an attractive interaction to adsorbed molecules even in the case of AN, where no condensation behavior was observed without electrolyte. On the other hand, the electrical repulsion of cations seems to be dominant above 100 mM at the interface, causing the intermolecular interaction to switch to a repulsive behavior. The effects of electrolyte concentration and light illumination are discussed from the estimated surface coverage in Figure 2-9c. The standard deviations in the equilibrium region during light illumination are largest at 100 mM for both solvents, which may correspond to a large number of molecules moving to in the localized electric field and to fluctuations in the number of molecules after molecular aggregation. The most condensation happened at 100 mM electrolyte while 44bpy is constantly diffusing at the same time. On the other hand, in 0 and 1000 mM, the number of molecules is small, and therefore, the increase or decrease within the observation region is small (Figure 2-9a, b). In H_2O, the coverage increased with a plasmon-enhanced electric field even without the addition of electrolyte,

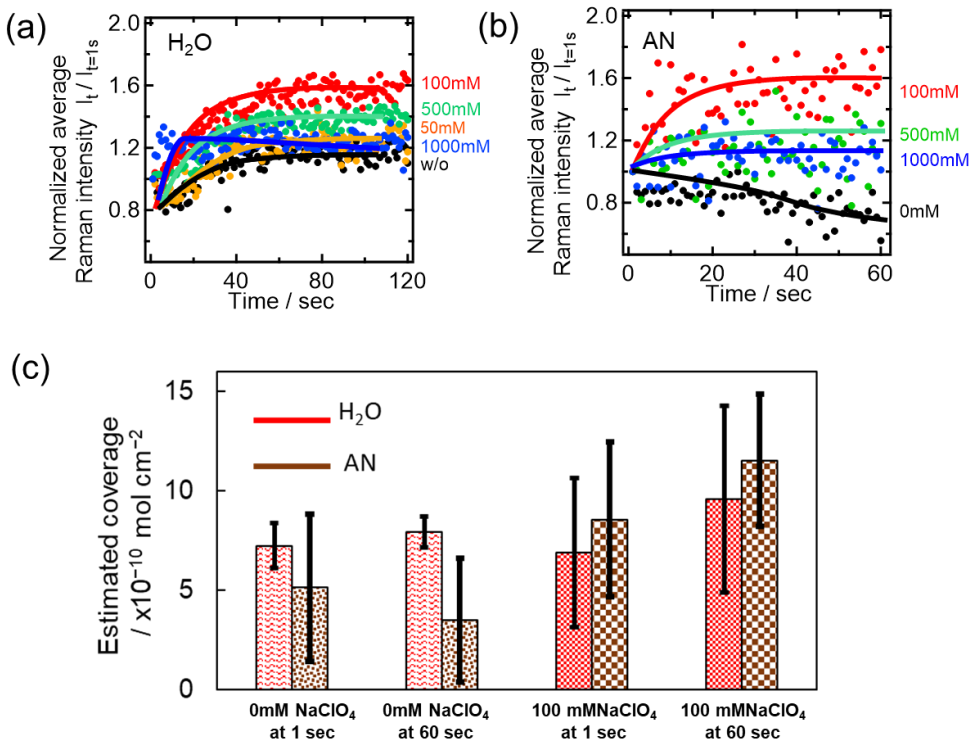

Figure 2-9. Time dependent normalized average intensity plot from 1608 cm^{-1} mode of 1mM 44bpy in various electrolyte density in(a) H_2O and (b)AN solution with more than 5 trials: black (0 mM), orange (50 mM), red (100 mM), green (500 mM), and blue (1000 mM) with approximation line. Each dot is plotted from spectra obtained under I_{ex}: 140μW μm^{-2} with 1 sec exposure time. (c) Bars are corresponding the estimated coverage from SERS intensity of (a, b) for with and without 100 mM $NaClO_4$ at initial and 60 s later.

and I observed aggregations beyond the thermodynamic equilibrium states. On the other hand, when electrolyte was added, the displacement before and after illumination is increasing from 6.89 to 9.60 × 10^{-10} mol cm^{-2}, which indicates strong molecular aggregation in 100 mM electrolyte solution, where packed 44bpy coverage takes the typical value of 9.60 × 10^{-10} mol cm^{-2} by STM study.[34] In the case of AN, as the addition of 100 mM salt significantly modulated the initial coverage and increased the intensity with light illumination, the coverage changed from 8.57 to 11.5 × 10^{-10} mol cm^{-2}. This may be due to the lower volume concentration of AN compared to water, H_2O: 55.3 mol

L^{-1}, AN: 19.0 mol L^{-1}, which effectively affects the ion coupling to 44bpys at the interface. It is also suggested that the optical modulation of the molecular motion could have originated from correlation with the collective molecules.

Finally, I discuss key factors of solvent dependent molecular motion modulation. There are several parameters related to thermal effects: the temperature at the plasmon interface under illumination (T_I) using thermal conductivity in Table 2-2, dynamic viscosity at T_I, diffusion constant (D), the drift velocity by thermophoresis (v_T), and estimated adsorption Gibbs energy from SERS intensity (ΔG^0_{Ads}). Although the diffusion velocity at the interface differs from that in the bulk defined by the Stokes-Einstein equation, I estimated the v_T by the relationship in here.

The increase in surface temperature due to plasmon resonance is nearly 25 K for solutions other than water, which has the highest thermal conductivity. As a result, the drift velocity, one of the parameters to move along the temperature gradation, is smallest for water. Here, the Soret coefficient, which determines thermal diffusion, decreases in proportion to the salt concentration, which suppresses the effect of thermal diffusion.[36] These estimates suggest that molecular aggregation under light illumination depends on Brownian motion, thermophoresis and Fick's law of diffusion. In other words, water has the relatively small diffusion constant and thermal diffusion at the surface,

Table 2-4. Thermal diffusion property of pure solvents by literature and estimated values for the present experiment

Solvent	T_I [K] [a]	η (at T_I) [mPa s^{-1}] [b]	D $\times10^{-10}$ [m^2 s^{-1}] [c]	v_T $\times10^{-3}$ [m s^{-1}] [d]	ΔG^0_{Ads} [kJ] [e]
H_2O	307.4	0.72[18]	7.1	8.1	−35.0
DMF	322.1	0.71[18]	7.1	19	−21.0
AN	325.5	0.24[21]	22	64	−19.3
IPA	324.6	0.59[23]	6.9	20	−19.5
Hex	325.4	0.24[25]	22	63	−17.9
H_2O + $NaClO_4$ (100 mM)	307.4	0.72[f]	7.1	8.1	-
AN + $NaClO_4$ (100 mM)	325.5	0.26[g]	20	58	-

a: $\Delta T\ mW^{-1}\ \mu m^{-2} = -143\sigma + 122.14$ (ref[35]), T_I=296 + ΔT, incident power: 0.28$mW\ \mu m^{-2}$.
b: The dynamic viscosity at T_I is estimated value as an assumption of liner relationship for references.
c: Storks-Einstein equation. $D = kT_i/6\pi a\eta$, a: 0.439 nm (short axis of 44bpy, gaussian16_SCRF_water) or a: 0.463 nm (SCRF_acetonitrile) for AN, DMF, IPA, and Hex.
d: $v_T = D_T\nabla T$, $D_T = S_T D$, (S_T~0.01),[36] $\nabla T = \Delta T/\Delta x = (T_I - 296)/(1.0 \times 10^{-8})$.
e: Estimated from SERS intensity at 1s with Equation 2-2 from Figure 2-7a.
f: For 0.1 M $NaClO_4$ aq. has 1.0038 times higher viscosity to pure water. [37]
g: It is roughly estimated by analog for 1.1 times increment of experimentally measured viscosity with 0.1 M NaCl. [38]

while other solvents are more affected by the thermophoretic effect. These thermodynamic effects partially explain the modulation of molecular condensation (Figure 2-6 and Figure 2-7) during illumination because the thermophoretic effect causes the reduction of molecules in the hotspot. The tendency to increase the number of molecules in the hotspot can be attributed to the fact that temporarily decelerated molecules come into contact with each other and are further stabilized by intermolecular forces. In the case of 44bpy, the dispersion forces between molecules without dipole moments are expected to be attractive within ~1 nm distance. In particular, the stacking of aromatic rings induces a stabilization equivalent to room temperature energy (2.5 kJ

mol^{-1}), which also causes substantial changes in polarizability on a stacked structure.[39] In an enhanced electric field, the induced polarization slows the speed of the molecule, so the difference in diffusion speed can be considered to be the number of molecules entering the enhanced electric field per unit time. It is expected that the velocity and number of molecules would depend on the diffusion constant, as seen in the different saturation times between H_2O and AN, about 60 s and 20 s, respectively, in Figure 2-9, which corresponds to the difference of this value 7.1 and 22 $\times 10^{-10}$ m^2 s^{-1}, respectively in Table 2-4. It should be noted that the adsorption energy is specific to the change in binding energy from solvation in solution to adsorption on the metal. Since the solvation energy is solvent-dependent, the coverage of the molecular surface is usually considered to be solvent-dependent. This is represented by the energy change from the solvent to the gold surface, G^0_{Ads}. The estimated ΔG^0_{Ads} from the SERS intensity in Table 2-4, derived from Figure 2-7, is reasonable to describe the solvent dependence of the variation of the experimental SERS intensity, but the molecular interaction between 44bpys or 44bpy and cations still needs to be discussed. Therefore, in the next section, I verified the molecular dependence of 2D diffusion modulation with different analogs of 44bpy to clarify the molecular interaction for optical condensation.

2.3.4 Evaluation of molecular property for diffusion modulation

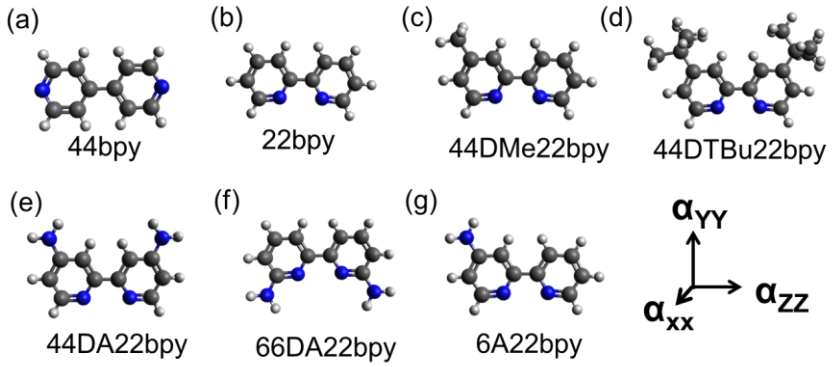

Figure 2-10. Schematic diagram of bipyridine analogs with polarization coordinate. (a) 4,4'-bipyridine(44bpy), (b) 2,2'-bipyridine(22bpy), (c) 4,4'-dimethyle -2,2'-bipyridine(44DMe22bpy), (d) 4,4'-di-tert-butyl-2,2'-bipyridine (44DTBu22bpy), (e) 4,4'-diamino -2,2'-bipyridine (44DA22bpy), (f.) 6,6'-diamino -2,2'-bipyridine (66DA22bpy), (g) 6-amino-2,2'-bipyridine (6A22bpy).

The structural equations and polarizabilities in Cartesian coordinates for each 22bpy analog are shown in Figure 2-10 and Table 2-6. The black, blue, and white spheres represent carbon, nitrogen, and hydrogen atoms, respectively. The polarizabilities of the bpy analogs in each coordinate direction were calculated by density functional theory (DFT) using Gaussian09 and summarized in Table 2.6.

Table. 2-6. Simulated polarizability of each bpy analog

molecules	α_{XX} $\times 10^{-40}$ [$Cm^2\ V^{-1}$]	α_{YY} $\times 10^{-40}$ [$Cm^2\ V^{-1}$]	α_{ZZ} $\times 10^{-40}$ [$Cm^2\ V^{-1}$]
44bpy	6.56	21.4	29.5
22bpy	6.53	19.7	32.5
44DMe22bpy	9.81	24.4	35.2
44DTBu22bpy	20.3	35.8	48.6
44DA22bpy	7.36	24.7	36.0
66DA22bpy	7.30	25.8	36.1
6A22bpy	6.91	22.2	35.2

a: Calculated polarizability (gaussian09, DFT_B3LYP) by 785 nm incident wavelength.

The polarizability tends to increase with more substituent, especially (d) 44DTBu22bpy has a value of 48.6×10^{-40} Cm^2V^{-1} in the Z-axis direction, which is almost 1.5 times higher than that of 44bpy and 22bpy. Thus, based on the polarizability as a factor of the optical force (Equation 1-4), the trapping behavior would vary in the polarizability orders of each bpy analog. Note that, any optical force predicted from these simple polarizabilities under 785 nm laser is smaller than in typical optical trapping experiments.[40]

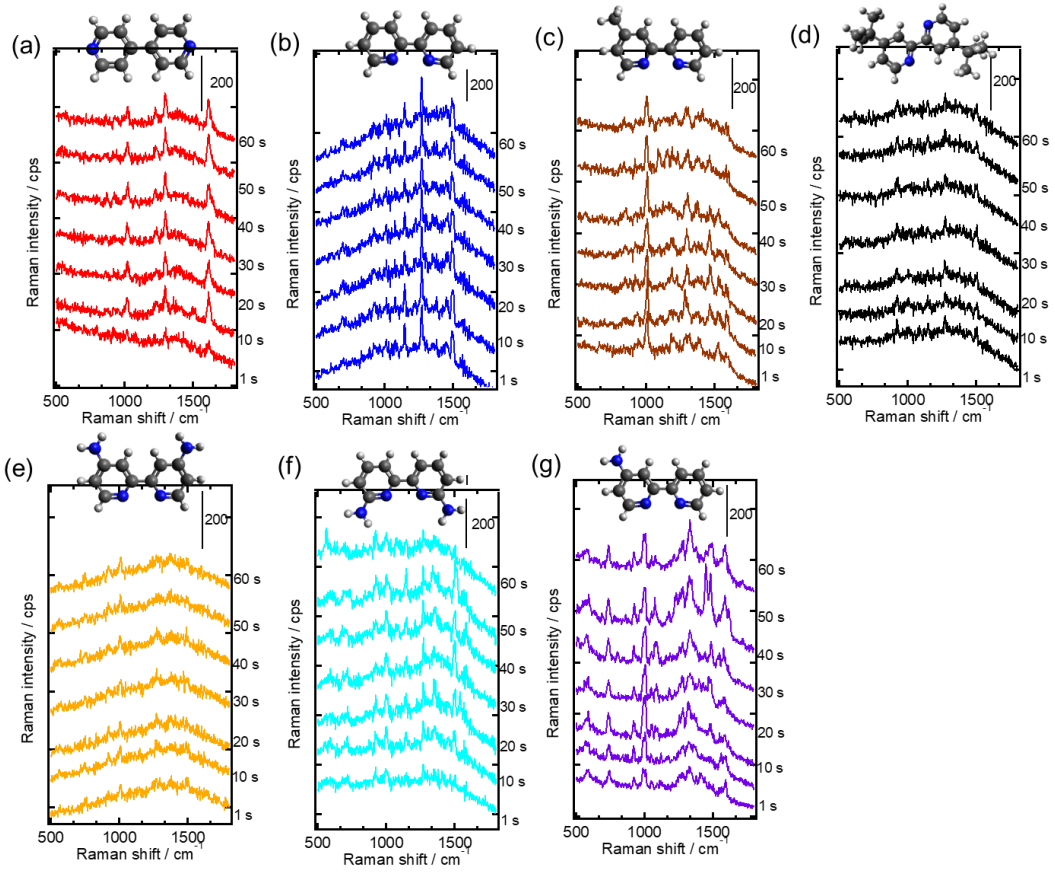

Figure 2-11. SERS spectra of 1mM bpy analogs + 0.1 M $NaClO_4$ acetonitrile solution on Au dimer nanoprism array under I_{ex}: 280 μW μm^{-2} at room temperature. Time-series SERS spectra under 60 s continuous illumination with t_{ex}: 1 s are taken in each bpy analogs dissolved solution; (a) 44bpy (red), (b) 22bpy(blue), (c) 4DMe22bpy (brown), (e) 4DTBu22bpy (black), (d) 44DA22bpy (orange), (e) 66A22bpy (turquoise), and (f) 66A22bpy (purple).

The following experiments are the time-course SERS analysis for each molecule in 0.1 M $NaClO_4$ added acetonitrile solution under I_{ex}: 280 μW m^{-2} on Au dimer nanoprism array. The colored spectra in Figure 2-11 show vertically aligned time-variation spectra. In contrast, the 44bpy spectra in Figure 2-11(a) show an increasing trend similar to the results in the previous section. 22bpy and its analogs showed low scattering intensity and large fluctuations in the spectra during the observation time. Although 44DTBu22bpy has the highest polarization, the lowest Raman signal and the smallest intensity change were observed as for other 22bpy analogs. In addition, the scattering intensity for the two substituted amino groups (e, f) was low and stable with time, while for the monosubstituted group (g), the intensity was higher than that of 44bpy and a significant increasing trend was observed. To get more insight, I normalized their intensity change over each specific peak intensity as shown in Figure 2-12 by dividing all peak intensities by the intensity at 1s. In the standardized intensity plots, only 44bpy (red line) and 6A22bpy (purple line) show a significant increase in illumination as the signal-to-noise ratio is exceeded as evidence of the correlation between molecular interaction and optical condensation, which is difficult to separate in the case of 66DA22bpy.

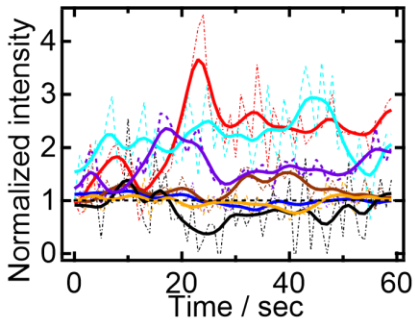

Figure 2-12. Normalized SERS intensity plot of 1mM bpy analogs + 0.1 M $NaClO_4$ acetonitrile solution from Figure 2-11. Intensity date ware plot as dotted lines and smoothed line for (a) 44bpy (red), (b) 22bpy(blue), (c) 4DMe22bpy (brown), (e) 4DTBu22bpy (black), (d) 44DA22bpy (orange), (e) 66A22bpy (turquoise), and (f) 66A22bpy (purple).

molecules are bulky such as 66DA22bpy, 44DMe22bpy, 44DA22bpy and 44DTBu22bpy. This steric hindrance to alignment on the metal surface is also affected by orientation, as is the case for 22bpy with planer conformation adsorption, and thus electrochemical control can be effective to improve the trapping behavior. Although these results cannot be easily compared because they reflect the chemical properties of the substance and the physical properties of light pressure, they indicate that intermolecular interactions are strongly effective by aligning on the Au surface with its π-π interaction between each bpy.

2.3.5 Electrochemical control of adsorbed molecules

The electrochemical SERS measurements were performed out using plasmonic dimer structures immersed in the solution of 1mM 44bpy + 0.1 M $NaClO_4$ aq. or 1mM 22bpy + 0.1 M $NaClO_4$ aq. at the different electrochemical potentials. In both cases, SERS spectra change depending on the electrochemical potential and are reversible against the potential scan. From relative peak intensity ratio for 44bpy, mainly between 1231 and 1291 cm^{-1} or 1291 and 1608 cm^{-1} as discussed in section 2.3.3, the orientation changes from stand-up to edge-on as a negative sweep. For the 22bpy case, the relative peak intensity ratio between 1180 and 1480 cm^{-1} is changed, when they are oriented from trans or cisoid to cis formation as a negative sweep.[41,42] Another point of electrochemical SERS of 44bpy / 22bpy is the reduction / enhancement of intensity as a negative potential sweep. Then, I experienced a mixed solution of 44bpy and 22bpy as 1mM aq. containing 0.1 M $NaClO_4$, called a bi-analyte solution, for comparing adsorbed stability and interaction between structural isomers.

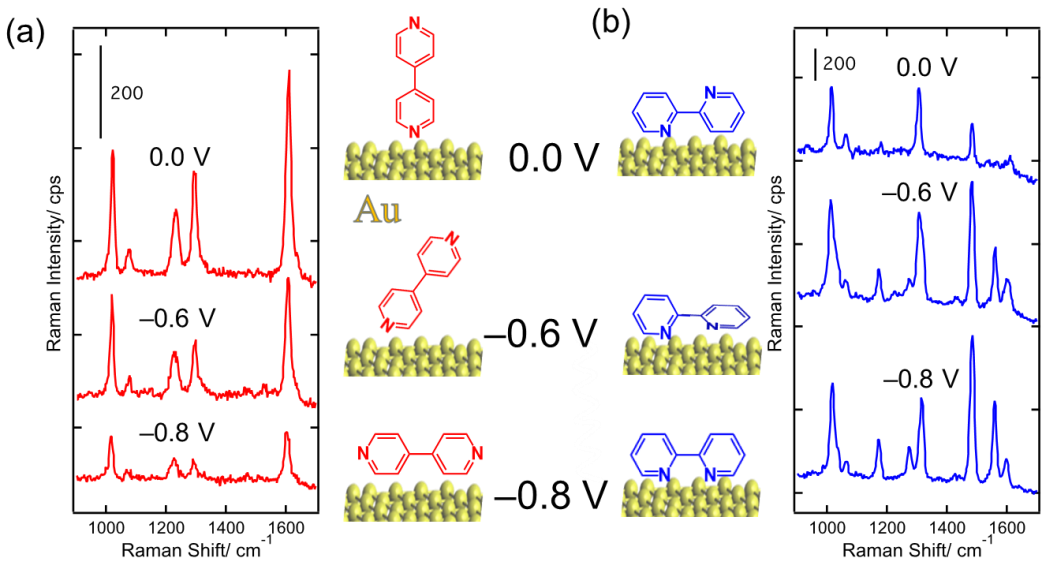

Figure 2-13. Potential dependent series SERS spectra of (a) 1mM 44bpy + 0.1 M NaClO4 aq. and (a) 1mM 44bpy + 0.1 M NaClO4 aq. with t_{ex}: 1 s under I_{ex}: (a) 140 μW μm^{-2} or (b) 70 μW μm^{-2}, potential range from +0.0 V to –0.8 V vs Ag/ AgCl. Inset configurations are confirmed by relative peak intensity ration for each spectrum.

When the potential scanned from positive to negative of 44bpy and 22bpy mixed solution, the intensity of the peak at 1609 cm^{-1}, which is assigned to the C-N and C-C stretching of the pyridyl ring of 44bpy, gradually decreased while the same band of 22bpy at 1572 cm^{-1} emerged in Figure 2-14. These results imply that the dominant adsorption species with a positive potential is 44bpy, while it changes to 22bpy with a negative potential. Since the coverage is almost full, the change in the relative SERS intensity of 44bpy between 22bpy reflects the ratio of them in a mono-molecular layer. The dominant adsorbate reflects relatively stronger adsorption of 44bpy for positive at the potential above 0 V and 22bpy for negative below −0.6 V. For further discussion, the intensity correlation plot of SERS bands was also shown in Figure 2-15. To discuss the molecular orientation, it is important to confirm the stability of certain adsorption states. In Figure

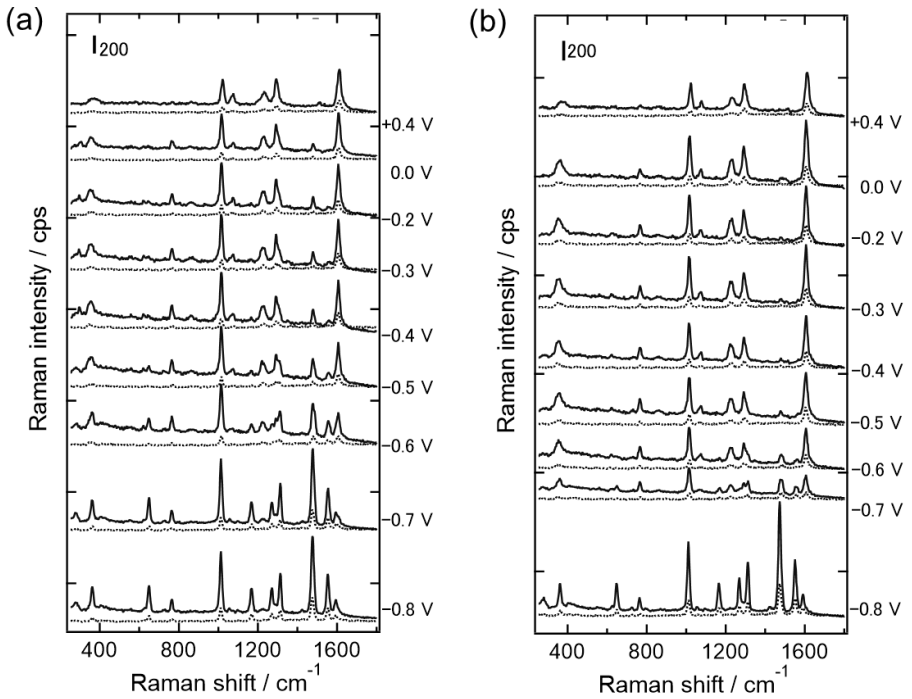

Figure 2-14. Potential dependent series SERS spectra of (a) 1mM 44bpy and 1mM 22bpy containing 0.1 M NaClO4 aq. with t_{ex}: 1 s under I_{ex}: 70 μW μm^{-2}. Potential was controlled with (a) the cathodic scan from −0.8 to 0.4 V and, then anodic scanned (b) from 0.4 to −0.8 V. The solid and broken lines correspond to longitudinal and transverse polarization to Au dimer, respectively.

2-15a, the SERS band intensities of 44bpy at 1608 cm^{-1} (ring stretching mode, left) and the 1230 cm^{-1} (C-H in-plane deformation mode, right) are plotted against at 1291 cm^{-1} (C-C inter-ring stretching), which observed in the bi-analyte solution at 0.4 V and −0.4 V because the Au surface is almost fully covered with 44bpy according to Figure 2-14. The blue circle and red rectangle represented the data obtained at −0.4 and 0.4 V, respectively. To evaluate the characteristics of the bi-analyte system, the SERS correlation regions in pure 1 mM 44bpy or 1 mM 22bpy were also noted as color-filled areas.

Through electrochemical SERS measurements in pure 44bpy or 22bpy systems, it was confirmed that the data points of pure 44bpy or 22bpy are distributed within the

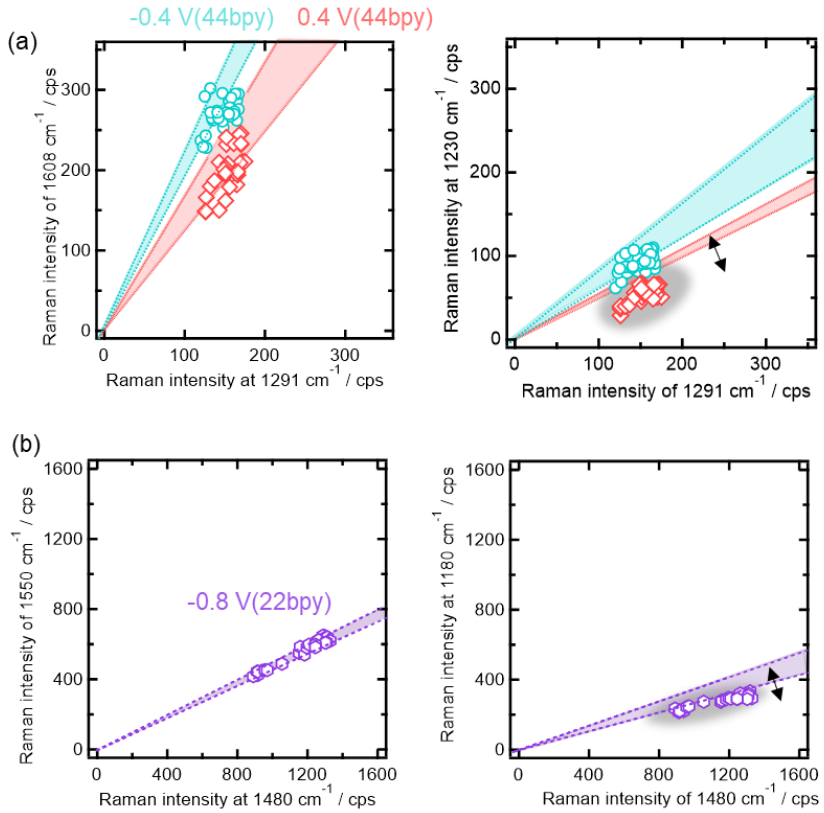

Figure 2-15. Correlation plots of the SERS intensities were made from (a) 1291 vs. 1608 cm−1 in left panel and 1230 vs. 1291 cm−1 in right of 44bpy or (b) to 1480 vs. 1550 cm−1 in left and 1180 vs. 1480cm−1 in right of 22bpy in the bi-analyte solution of 1 mM 44bpy and 1mM 22bby containing 0.1 M NaClO4 aq. with tex: 1 s under Iex: 70 μW μm−2 in 30 s illumination The electrochemical potential is 0.4 (red), −0.4 (blue), and −0.8 V (purple), respectively. Filled region in triangles with the distinct colors indicates the dispersion of the correlation plots obtained in the solution of pure 1 mM 44bpy (red, blue) or 1 mM 22bpy (purple) containing 0.1 M $NaClO_4$ aq.

filled blue and red colored regions at −0.4 and 0.4 V, respectively. According to the discussion in Figure 2-12, the 44bpy molecules absorbed on the metal surface with stand-up and edge-on orientations at 0.4 and −0.4 V in a pure condition, respectively. While this orientation was also confirmed in the bi-analyte solution since in that range, the specific band intensity such as 1230 cm^{-1} in the bi-analyte solution shows displacement from pure solution as in the right panel of Figure 2-15a, even though there is no 22bpy SERS signal from the hot spot of Au dimer surface. Therefore, the electrochemical potential can define

the molecular orientation even in the bi-analyte system, but these molecules seem to be influenced by surrounding isomers. Similar behavior is recognized for 22bpy at −0.8 V as demonstrated in Figure 2-15b. For the 22bpy, the correlations between 1550 (ring stretching + in-plane bending) and 1480 cm^{-1} (in-plane deformation) of 22bpy in the bi-analyte system at −0.8 V agree well with those of the pure 22bpy shown as the purple region, the 1180 cm^{-1} (ring stretching + ring deformation + C-H in-plane deformation) in the bi-analyte solution was different from that in a pure state. These deviations of the bi-analyte system compared to the pure systems suggest the formation of unique molecular orientations or interactions in the mixed monomolecular layer. In particular, the modes of the C-H in-plane deformation for both 44bpy and 22bpy were influenced by the presence of the structural isomers. It should be noted that the linear intensity increments in Figure 2-15 represent the molecular condensation in the bi-analyte solution. From these results, the introduction of electrochemical control to the plasmon optical trapping system gives precise control of the condensed behavior via modulating 2D diffusion, since 44bpy and 22bpy are hardly trapped unless at negative potential as in Figure 2-11 and 12.

2.4 Conclusion

In this chapter, the observation of interfacial molecules by SERS was considered to be suitable for analyzing the adsorption stability of molecules and the modulation of molecular motion at the plasmon field. The observation of the solvent dependence of the molecular motion revealed not only the different optical condensation behavior of each molecule, but also the electrolyte-related induced motion modulation. The importance of molecular interactions at the interface is explored in Figure 2-9. Through experiments with bpy analogs to verify the factor of optical condensation behavior, even for molecules with similar structures in the substituents, the bulkiness of molecules has a significant effect on the modulation of 2D diffusion. Thus, the selection of target molecules and solutions is one of the key points for molecular manipulation. Not only due to molecular aggregation, vibrational modulation was observed in the one-component system as shown in Figure 2-6, but also in the two-component system, the surrounding isomer, even though it does not dominantly cover the surface, has an influence on the specific vibrational mode discussed in Figure 2-15.

Finally, I have shown that the combination of electrochemical control and optical trapping system can be an important tool to discuss the interfacial molecular property at the solid-liquid interface with an insight into their total motions, where the modulation of vibrational motion may have possibilities in reaction control. However, it is still under discussion that the in-situ observation directly corresponds to the identical molecular motion, because the SERS signal in the present system originates from many hot spots of the array structure. In the next chapter, I will try the single hot-spot SERS measurement and improve the plasmon-assisted molecular aggregation process for a more precise understanding.

2.5 References

(1) Nel, A. E.; Mädler, L.; Velegol, D.; Xia, T.; Hoek, E. M. V.; Somasundaran, P.; Klaessig, F.; Castranova, V.; Thompson, M. Understanding Biophysicochemical Interactions at the Nano-Bio Interface. Nat. Mater. 2009, 8 (7), 543–557.

(2) Hao, F.; Stoumpos, C. C.; Liu, Z.; Chang, R. P. H.; Kanatzidis, M. G. Controllable Perovskite Crystallization at a Gas–Solid Interface for Hole Conductor-Free Solar Cells with Steady Power Conversion Efficiency over 10%. J. Am. Chem. Soc. 2014, 136 (46), 16411–16419.

(3) Lombardi, J. R.; Birke, R. L. A Unified View of Surface-Enhanced Raman Scattering. Acc. Chem. Res. 2009, 42 (6), 734–742.

(4) Schlücker, S. Surface-Enhanced Raman Spectroscopy: Concepts and Chemical Applications. Angew. Chemie - Int. Ed. 2014, 53 (19), 4756–4795.

(5) Hao, E.; Schatz, G. C. Electromagnetic Fields around Silver Nanoparticles and Dimers. J. Chem. Phys. 2004, 120 (1), 357–366.

(6) Haynes, C. L.; Van Duyne, R. P. Nanosphere Lithography: A Versatile Nanofabrication Tool for Studies of Size-Dependent Nanoparticle Optics. J. Phys. Chem. B 2001, 105 (24), 5599–5611.

(7) Uosaki, K.; Allen, H.; Hill, O. Absorption Behaviour of 4,4′-Bipyridyl at a Gold/Water Interface and Its Role in the Electron Transfer Reaction between Cytochrome c and a Gold Electrode. J. Electroanal. Chem. Interfacial Electrochem. 1981, 122, 321–326.

(8) Yang, D.; Bizzotto, D.; Lipkowski, J.; Pettinger, B.; Mirwald, S. Electrochemical and Second Harmonic Generation Studies of 2,2'-Bipyridine Adsorption at the Au(111) Electrode Surface. J. Phys. Chem. 1994, 98 (28), 7083–7089.

(9) Brolo, A. G.; Jiang, Z.; Irish, D. E. The Orientation of 2,2′-Bipyridine Adsorbed at a SERS-Active Au(111) Electrode Surface. J. Electroanal. Chem. 2003, 547 (2), 163–172.

(10) Suzuki, M.; Niidome, Y.; Yamada, S. Adsorption Characteristics of 4,4′-Bipyridine Molecules on Gold Nanosphere Films Studied by Surface-Enhanced Raman Scattering. Thin Solid Films 2006, 496 (2), 740–747.

(11) Sprague-Klein, E. A.; Ho-Wu, R.; Nguyen, D.; Coste, S. C.; Wu, Y.; McMahon, J. J.; Seideman, T.; Schatz, G. C.; Van Duyne, R. P. Modulating the Electron Affinity of Small Bipyridyl Molecules on Single Gold Nanoparticles for Plasmon-Driven Electron Transfer. J. Phys. Chem. C 2021, 125 (40), 22142–22153.

(12) Aminabhavi, T. M.; Gopalakrishna, B. Density, Viscosity, Refractive Index, and Speed of Sound in Aqueous Mixtures of N,N-Dimethylformamide, Dimethyl Sulfoxide, N,N-Dimethylacetamide, Acetonitrile, Ethylene Glycol, Diethylene Glycol, 1,4-Dioxane, Tetrahydrofuran, 2-Methoxyethanol, and 2-Ethox. J. Chem. Eng. Data 1995, 40 (4), 856–

861.

(13) Green, D. W.; Perry, R. H. Perry's Chemical Engineers' Handbook, Eighth Edi.; McGraw Hill professional; McGraw-Hill Education, 2007.

(14) Hale, G. M.; Querry, M. R. Optical Constants of Water in the 200-Nm to 200-Mm Wavelength Region. 1989, 12 (3), 555–563.

(15) Korson, L.; Drost-Hansen, W.; Millero, F. J. Viscosity of Water at Various Temperatures. J. Phys. Chem. 1969, 73 (1), 34–39.

(16) Ramires, M. L. V; Nieto de Castro, C. A.; Nagasaka, Y.; Nagashima, A.; Assael, M. J.; Wakeham, W. A. Standard Reference Data for the Thermal Conductivity of Water. J. Phys. Chem. Ref. Data 1995, 24 (3), 1377–1381.

(17) Haynes, W. M. CRC Handbook of Chemistry and Physics, 95th ed.; CRC Press: Hoboken, 2014.

(18) Alam, M. S.; Ashokkumar, B.; Siddiq, A. M. The Density, Dynamic Viscosity and Kinematic Viscosity of Protic and Aprotic Polar Solvent (Pure and Mixed) Systems: An Experimental and Theoretical Insight of Thermophysical Properties. J. Mol. Liq. 2019, 281, 584–597.

(19) Shokouhi, M.; Jalili, A. H. Thermo Physical Properties of Some Physical and Chemical Solvents at Atmospheric Pressure. 2013, 10 (4), 43–54.

(20) Kozma, I. Z.; Krok, P.; Riedle, E. Direct Measurement of the Group-Velocity Mismatch and Derivation of the Refractive-Index Ultraviolet. 2005, 22 (7), 1479–1485.

(21) Ritzoulis, G.; Papadopoulos, N.; Jannakoudakis, D. Densities, Viscosities, and Dielectric Constants of Acetonitrile + Toluene at 15, 25, and 35 .Degree.C. J. Chem. Eng. Data 1986, 31 (2), 146–148.

(22) Hulse, R. J.; Anderson, M. W.; Bybee, M. D.; Gonda, D. D.; Miller, C. A.; Oscarson, J. L.; Rowley, R. L.; Wilding, W. V. Liquid Thermal Conductivities of Acetonitrile, Diethyl Sulfide, Hexamethyleneimine, Tetrahydrothiophene, and Tetramethylethylenediamine. J. Chem. Eng. Data 2004, 49 (5), 1433–1435.

(23) Aminabhavi, T. M.; Aralaguppi, M. I.; Harogoppad, S. B.; Balundgi, R. H. Densities, Viscosities, Refractive Indices, and Speeds of Sound for Methyl Acetoacetate + Aliphatic Alcohols (C1–C8). J. Chem. Eng. Data 1993, 38 (1), 31–39.

(24) OGIWARA, K.; ARAI, Y.; SAITO, S. THERMAL CONDUCTIVITIES OF LIQUID ALCOHOLS AND THEIR BINARY MIXTURES. J. Chem. Eng. Japan 1982, 15 (5), 335–342.

(25) Sharma, A.; Rani, M.; Maken, S. Thermodynamics of Haloarenes with N-Hexane at 298.15–318.15 K: Density, Ultrasonic Speed and Viscosity. J. Mol. Liq. 2021, 321, 114366.

(26) Neindre, B. Le; Lombardi, G.; Desmarest, P.; Kayser, M.; Sabirzianov, A. N.; Gabitov, F.

R.; Gumerov, F.; Garrabos, Y. Fluid Phase Equilibria Thermal Conductivity of Gaseous and Liquid N-Hexane. Fluid Phase Equilib. 2018, 474, 60–75.

(27) Futamata, M.; Maruyama, Y.; Ishikawa, M. Metal Nanostructures with Single Molecule Sensitivity in Surface Enhanced Raman Scattering. Vib. Spectrosc. 2004, 35 (1–2), 121–129.

(28) Noda, I.; Ozaki, Y. Two-Dimensional Correlation Spectroscopy - Applications in Vibrational and Optical Spectroscopy; John Wiley & Sons, Ltd: Chichester, UK, 2004.

(29) Zhang, Y.; Zhang, R.; Jiang, S.; Zhang, Y.; Dong, Z. C. Probing Adsorption Configurations of Small Molecules on Surfaces by Single-Molecule Tip-Enhanced Raman Spectroscopy. ChemPhysChem 2019, 20 (1), 37–41.

(30) Tirado, J. D.; Acevedo, D.; Bretz, R. L.; Abruña, H. D. Adsorption Dynamics of Electroactive Self-Assembling Molecules. Langmuir 1994, 10 (6), 1971–1979.

(31) Gould, N. S.; Li, S.; Cho, H. J.; Landfield, H.; Caratzoulas, S.; Vlachos, D.; Bai, P.; Xu, B. Understanding Solvent Effects on Adsorption and Protonation in Porous Catalysts. Nat. Commun. 2020, 11 (1), 1–13.

(32) Ma, J. C.; Dougherty, D. A. The Cation−π Interaction. Chem. Rev. 1997, 97 (5), 1303–1324.

(33) Dougherty, D. A. The Cation-π Interaction. Acc. Chem. Res. 2013, 46 (4), 885–893.

(34) Mayer, D.; Dretschkow, T.; Ataka, K.; Wandlowski, T. Structural Transitions in 4,4′-Bipyridine Adlayers on Au(111)—an Electrochemical and in-Situ STM-Study. J. Electroanal. Chem. 2002, 524–525, 20–35.

(35) Takase, M.; Nabika, H.; Hoshina, S.; Nara, M.; Komeda, K.; Shito, R.; Yasuda, S.; Murakoshi, K. Local Thermal Elevation Probing of Metal Nanostructures during Laser Illumination Utilizing Surface-Enhanced Raman Scattering from a Single-Walled Carbon Nanotube. Phys. Chem. Chem. Phys. 2013, 15 (12), 4270–4274.

(36) Braibanti, M.; Vigolo, D.; Piazza, R. Does Thermophoretic Mobility Depend on Particle Size? Phys. Rev. Lett. 2008, 100 (10), 1–4.

(37) Nightingale, E. R. Viscosity of Aqueous Sodium Perchlorate Solutions. J. Phys. Chem. 1959, 63 (5), 742–743.

(38) Hawlicka, E. Acetonitrile-Water Solutions of Sodium Halides: Viscosity and Self-Diffusion of CH3CN and H2O. Zeitschrift für Naturforsch. A 1988, 43 (8–9), 769–773.

(39) Israelachvili, J. N. Intermolecular and Surface Forces; Intermolecular and Surface Forces; Elsevier Science, 2015; Vol. 46.

(40) Xu, H.; Käll, M. Surface-Plasmon-Enhanced Optical Forces in Silver Nanoaggregates. Phys. Rev. Lett. 2002, 89 (24), 246802.

(41) Wandlowski, T.; Ataka, K.; Mayer, D. In Situ Infrared Study of 4,4‘-Bipyridine Adsorption

on Thin Gold Films. Langmuir 2002, 18 (11), 4331–4341.

(42) Luo, Z.; Loo, B. H.; Cao, X.; Peng, A.; Yao, J. Probing the Conformational Transition of 2,2′-Bipyridyl under External Field by Surface-Enhanced Raman Spectroscopy. J. Phys. Chem. C 2012, 116 (4), 2884–2890.

Chapter 3

Molecular selective condensations at the localized electric field of single bowtie gap

3.1 Introduction

In addition to the diffusion modulation discussed in Chapter 2, the enhancement of light-molecular interactions could also open up various possibilities for novel applications of protoscience for energy conversion, ultrasensitive detection, and materials manipulation.[1–4] Since the optical properties of metal nanostructures are tuned by controlling their size, shape, or metal species, the bowtie structure with a gap distance of less than 5 nm generates a relatively strong optical field, the so-called hotspot at the gap.[5] Within such a plasmonic field, a detailed understanding of molecular condensation is achieved by retarding diffusion and polariton-molecule interaction in the single hotspot.

In this chapter, I have challenged molecular manipulation using localized electric field via single hotspot plasmon resonance to overcome the physical limitation of laser trapping. By adding electrochemical potential control to the plasmon resonance, I achieved the more precise control of interfacial molecules. Using Au nano bowtie structures combined with electrochemical potential control, it is possible to observe plasmon-modulated trapping behavior, orientation change, and molecule-metal interaction known as CT resonance at a single hot spot. Well-defined nanostructures such as narrow-gap bowtie not only enable selective trapping and concentration of molecules with in-situ tracking, but also reveal to understand the role of intermolecular interactions in modulating 2D diffusion and molecular states under CT resonance at room temperature.

3.2 Experimental method

3.2.1 Electric field evaluation by FDTD method

To evaluate the electric field intensity in the vicinity of metal, the electromagnetic model simulation by finite difference time domain method (FDTD) was applied to the present experimental model of nano-bowtie structure on glass substrate in water by the software (Lumerical, Ansys Inc.). The simulated electric field intensity is used to estimate Raman enhancement and optical force on molecules.

To overcome the molecular Brownian motion under the ambient condition, it is necessary for the optical force (Equation 3-1) to be stronger than the kinetic energy (k_BT). The F_{opt} can be described by the following equation in the z direction in one dimension;[6]

$$U = \int < \mathbf{F_{opt}} > \mathrm{dZ} \qquad \text{(Equation 3-1)}$$

To calculate F_{opt}, the polarizability value with a specific molecular orientation that is When the target molecule has no absorption or is in a non-resonant state, the imaginary part is negligible ($\alpha = \alpha' + \mathrm{i}\alpha'' \fallingdotseq \alpha'$) and then the static polarizability (calculated by gaussian16, B3LYP, 6-31g(d,p): Gaussian, Inc. with λ = 785 nm) is nearly equal to real polarizability at 785 nm excitation ($\alpha(785nm) = \alpha'(\lambda) + \mathrm{i}\alpha''(\lambda) \fallingdotseq \alpha'(785nm)$).

3.2.2 Fabrication of single bowtie structure

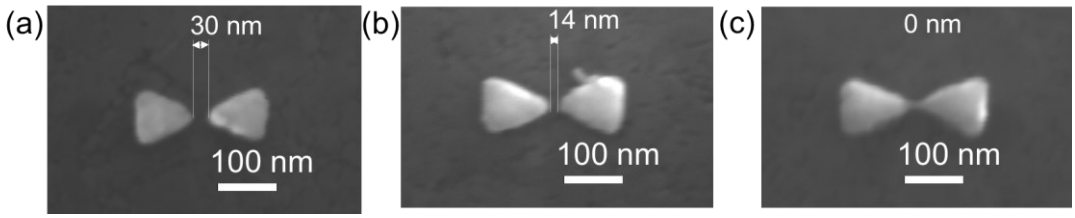

Figure 3-1. The image of Au bowtie (triangle: 100 nm × 120 nm × 30 nm) structures are obtained by SEM. Applied voltage: 10 kV. Preset gap distance is set as (a) 30 nm, (b) 15nm, and (c) 1.25 nm. Inset gap value are measured from SEM image.

For *in-situ* electrochemical SERS measurements of plasmon-induced optical manipulation, plasmonic structures were prepared on the conductive glass by electron beam drawing.[7] After spin-coating a resist solution (ZEP-520A: ZEPA = 2: 1) on the cleaned indium tin oxide (ITO) glass surface, it was heated at 140 °C for 3 min. The electron beam lithography was performed with an electron source scanning electron microscope (ELS-F125: Elionix Inc.) with the applied voltage of 125 kV and current of 50 pA under less than 10^{-4} Pa. The design for the electron beam irradiation was triangular with three types: 100 nm × 120 nm, 100 nm×150 nm, and 100 nm×200 nm. After electron beam irradiations, substrates were immersed in ZED-N50 for 60 sec and rinsed in ZMD-B for 10 sec. A sputtering machine (PMS-4000C1/HC1: ULVAC, Inc.) was used to deposit a 3 nm Ti layer as an adhesion layer on the ITO surface, and then a 30 nm Au layer was deposited on the Ti layer. The resist layer was removed in ZDMAC solution for 3 min and sonicated for 10 sec, then the substrates were cleaned in acetone and methanol for 10 sec each. The prepared Au structures were examined by the scanning electron microscopy using same equipment as for lithography. It is noted that the actual values of the gap spacing for each structure have variations from the default value as shown in Figure 3-1, especially for smaller gap spacing.

3.2.3 Electrochemical control of adsorbed molecules at single hot spot

To evaluate the molecular dynamics, electrochemical SERS measurements were performed using a home-made three-electrode electrochemical Raman cell as shown in Figure 2-2 and the same setup, the three-electrode electrochemical cell was composed of Au bowtie / Ti / ITO substrate, Pt wire and Ag/AgCl electrodes as the working and counter electrode and a reference electrode, respectively. The electrochemical potential of the Au bowtie structures was controlled by a potentiostat (HZ-7000: Hokuto Denko Corpration). The electrolyte solution was 0.1 M $NaClO_4$ aq. containing 44bpy and / or 22bpy. The concentrations of 44bpy and 22bpy were adjusted to 1 μM and 1 mM, respectively. Raman spectra were collected with a 785 nm laser polarized parallel to the long axis of the bowtie structures. The significantly enhanced electric field strength at the gap is given only when the laser is polarized parallel to the long axis.8 In addition, since there is such a single structure in the laser west of the incident light, it is assumed that the entire SERS signal originates from a hot spot in the gap. All of the Raman experiments were carried out under atmospheric conditions at 296 °C.

3.2.4 Time tracing of molecular condensation in bi-analyte solution

With the aim of quantitative analyses of the molecular number changes, the SERS intensities at the specific Raman band under different light intensity was traced in illumination time. The number of molecules can be estimated from the Raman intensity ($I_{\omega_{Raman}}$) as described in the following equation: [9,10]

$$I_{\omega_{Raman}} = \mathrm{C} \times \mathrm{M} \times (\omega_0 - \omega_{Raman})^4 N_{sca} t_{det} I_{in} \left(\rho \alpha_{\rho\sigma} \sigma\right)^2 \quad \text{(Equation 3-2)}$$

where C is the constant defined by the cell condition, optical set up, and some physical constants while M is the magnitude of plasmon enhanced electric field intensity determined by substrate. The term of $\alpha_{\rho\sigma}$ is the scattering tensor which is the static at the present electrochemical potential. All spectra were obtained with the same CCD detection time (t_{det}) of 1 sec under continuous exposure for 30 to120 sec. Since the incident intensity (I_{in}) has been kept constant during laser illumination, the N_{sca} can be given as the number of molecules at the hot spot.

3.3 Results and discussion

3.3.1 Estimation of optical force

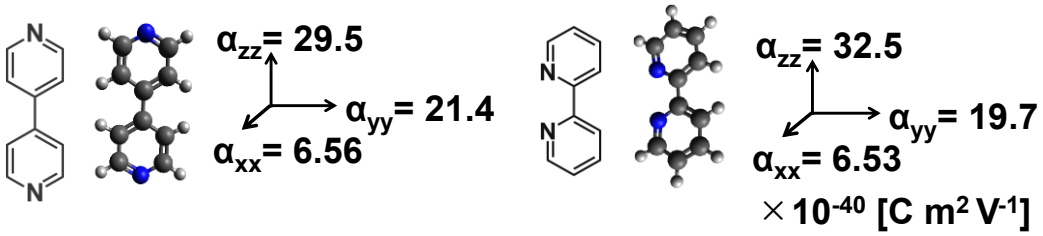

Figure 3-2. (a) Each polarizability of 44bpy / 22bpy is calculated as dipole momentum of isolated single molecule calculated for each Cartesian coordinate by density function theory (gaussian 16) with molecular formula.

DFT calculation gave 44bpy and 22bpy polarizability to each direction along to cartesian axis as single isolated molecules. For the case of localized electric field with adsorbed molecules on metal, the direction of polarization by electric field is defined to certain oriented molecules as shown in Figure3-2. FDTD simulation shows the highest electric intensity at bowtie gap region with up to E_{loc}: 150 V/m with E_0: 1 V/m in Figure 3-3 because this bowtie structure resonance at nearly 785 nm (excitation laser).

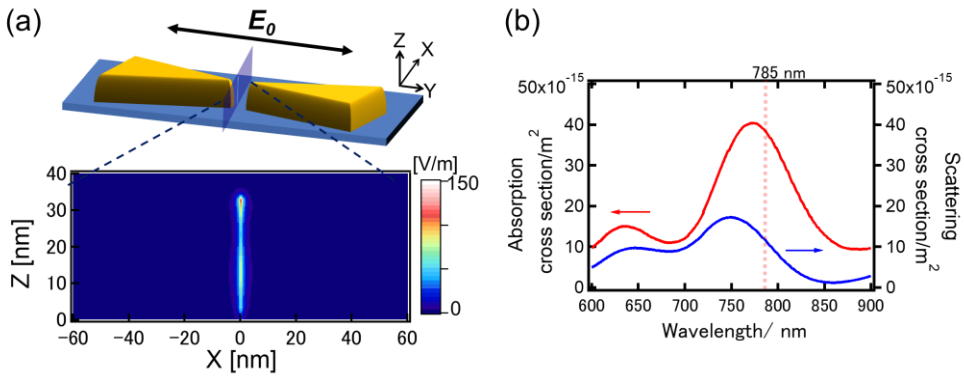

Figure 3-3. (a) Schematic picture of Au bowtie (triangle: 100 nm × 150 nm × 30 nm and 1 nm gap) on Ti layer and ITO layer with estimated electric field in the round edge plane and (b) scattering/absorption cross section by FDTD simulation (Lumerical FDTD package).

An optical force for non-resonant molecules is determined gradient force of Equation 3-1 while being proportional to the incident intensity of laser. In here, below 140 μW μm^{-2} intensity 785 nm laser, optical force of Z direction of Figure 3-3a on the Au surface of gap edge with parallel to 44bpy α_{yy} is estimated as 3.11 fN or for α_{xx} 0.953 fN with stand-up adsorbates at 0 V. Once 44bpy orientation is tilted until edge-on at −0.8 V, the maximum optical force is defined by α_{zz} as 4.29 fN. While, when 2,2'-bipyridine has cis edge-on orientation at −0.8V, α_{zz} is parallel to Z direction with 4.72 fN or 0.949 fN for α_{xx}. Optical potential was obtained by integral F_{opt} in Au surface, where calculated region is defined in one dimension edge of gold. The optical potential calculation with approximation of Equation 3-1 gave optical potential as -2.08×10^{-22} J for adsorbed 4,4'-bipyridine with α_{zz} orientated or 0.0697 k_BT. This value is 20 times lower than usually reported available trapping potential because of small polarizability and lower light intensity, the threshold at room temperature; 0.1 pN or 1 k_BT.[11,12] It should be noted that these estimations were based on the polarizability obtained from a simple isolated molecule model. In other words, I did not consider about the effect of the adsorption onto the metal surface as well as the interaction between molecules and metals to induce the charge transfer effect based on the resonant electronic excitation, leading to the increase of the polarizability.

3.3.2 Raman certification of plasmon-enhanced electric field

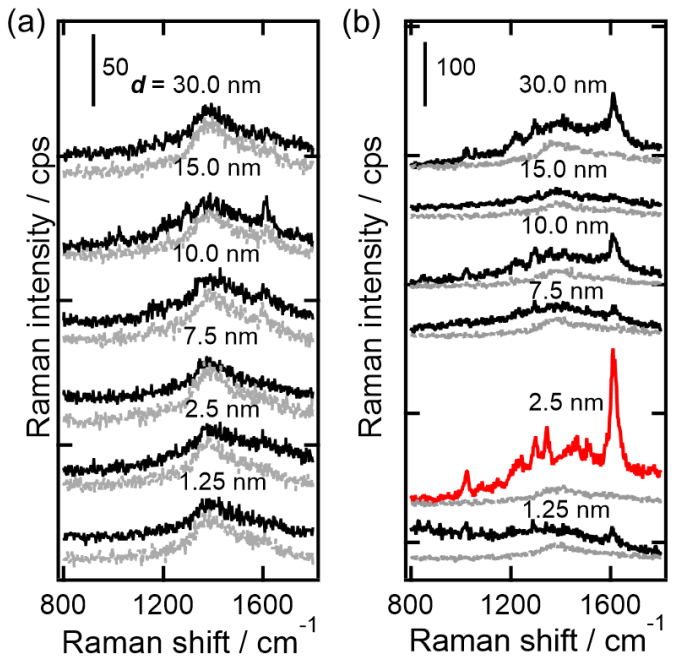

Figure 3-4. Linear polarized Raman spectra obtained by single Au bowtie with varied gap distance: *d* immersed in the electrolyte solution of 1 mM 44bpy and 22bpy containing 0.1 M $NaClO_4$ as the supporting electrolyte. The laser intensity and incident wavelength were 140 μW $μm^{-2}$. The polarized directions of the incident and scattered light were (a) YY (black) / YX (gray) or (b) XX (black) / XY (gray). A red spectrum remarks highest scattering intensity as XX direction.

SERS spectra were obtained from hotspot of single Au bowtie (triangle: 100 nm × 120 nm × 30 nm) with distinct gap distance values (*d*) immersed in the mixed solution of 1 mM 44bpy and 1 mM 22bpy. The values of the gap distance in Figure 3-4 are the drawing design preset for electron beam lithography. The incident light was polarized with parallel (X-direction) or vertical (Y-direction) relative to the long axis of the bowtie structure. In Figure 3-4a, the configurations of the incident light were Y-excitation and Y-scattering directions (black) / Y-excitation and X-scattering directions (gray), while spectra shown in Figure 3-4b were collected with the direction of X-excitation and X-scattering (black) / X-excitation and Y-scattering (gray).

These spectra apparently show *d* value dependence of the scattering intensities of Raman band at 1609 cm^{-1} under the condition of X-excitation and X-scattering (Figure 3-5). The SERS intensity at 1609 cm^{-1} was derived from C-N and C-C stretching vibration of the pyridyl ring of 44bpy.[13] As can be seen clearly, the *d* value of 2.5 nm provides the highest enhancement of Raman scattering. And also, it is known that the scattering intensity increases with decreasing of the *d* value because of the enhancement of the electromagnetic field.[8] It should be mentioned that the reason for the very low scattering intensity for $d = 1.25$ nm is due to the resolution limitation of the electron beam lithography technique, which may lead to the failure in the formation of the gap structure. Based on this fact, I have been performed electrochemical SERS measurements using the well-defined structure with the *d* value of 2.5 nm under the condition of X-excitation and X-scattering direction.

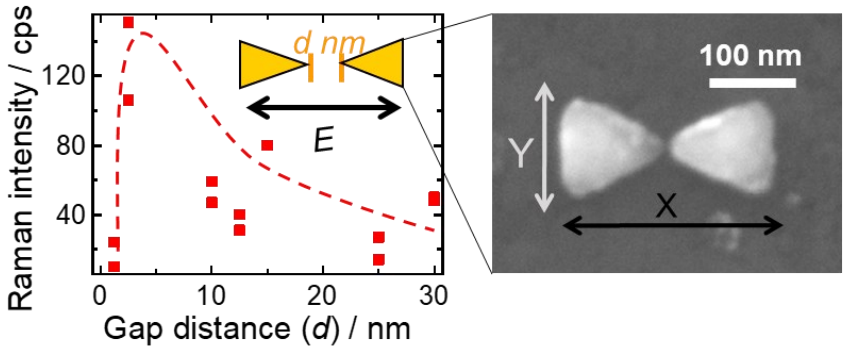

Figure 3-5. The relationship between the *d* values and the scattering intensity at 1609 cm^{-1}. Inset figure shows SEM image with polarized direction.

3.3.3 *In-situ* probing of switching behavior from single hotspot

EC-SERS measurements of 44bpy have been carried out using the Au bowtie (triangle: 100 nm × 120 nm × 30 nm) as shown in Figure 3-6a. Raman bands at 1021, 1229, and 1296 cm^{-1} are assigned to totally symmetric modes of 44bpy are derived from the ring breathing, C-H in-plane deformation, and ring stretching respectively. The scattering intensities gradually increased as the potential became negative. The SERS intensity is correlated with not only the intensity of the electromagnetic field but also the

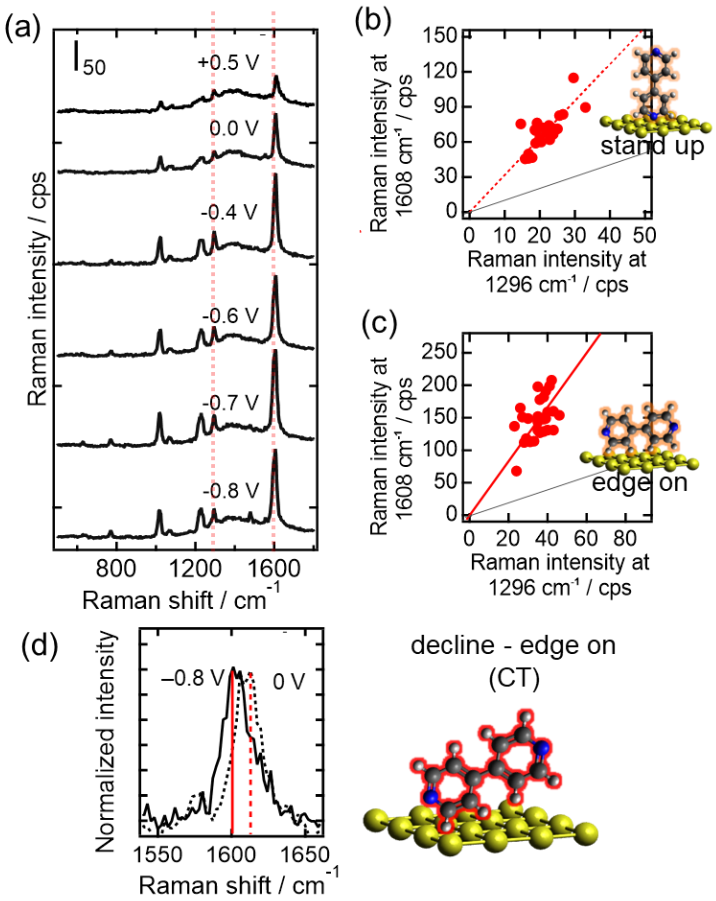

Figure 3-6. Potential dependent series SERS spectra of (a) 1mM 44bpy + 0.1 M $NaClO_4$ aq.. Exposure time is 5 s, incident intensity is 140 μW $μm^{-2}$, potential range from +0.5 V to –0.8 V vs Ag/ AgCl. Correlation plots are made from peak intensity of 1608 cm^{-1} vs 1296 cm^{-1} at (b) 0.0 V and (c) –0.8 V. Black line of reference ($y = x$). (d)The peak position of 1608 cm−1 is slightly shifted to negative at –0.8 V with schematic picture.

resonance contribution of CT effect induced by the electronic excitation between the Fermi level of the metal and the molecular orbitals.[14]

Correlation plots between vibration peaks can determine the molecular orientation of 44bpy against the metal surface from the linear relationship of the relative SERS band intensity at 1608 cm^{-1} to that at 1296 cm^{-1}, because those ratios are sensitively influenced by the change in the molecular orientation.[13] The 44bpy molecules coordinate via the N atoms with the stand-up orientation at the positively charged and, then, tilted to the edge-on orientation with the negative potential scan (Figure 3-6b,c).[15] It should be noteworthy that the surface coverage of the molecules on Au surface becomes close to unity in the concentration of 1 mM solution as confirmed by previous studies using EQCM, STM, and SIRAS. [19-21] The Langmuir isotherm of 44bpy and 22bpy also supports the formation of full coverage under the positive region. The observed changes in the SERS intensity dependence clearly show the contribution of the CT process as a function of the electrochemical potential. Indeed, the Raman band at 1608 cm^{-1} (the C-H symmetric vibrational mode of the pyridyl ring, A_g symmetry) slightly shifted to 1598 cm^{-1} at the negative potential of –0.8 V, as shown in Figure 3-6d. This shifted Raman band can be assigned to the excitation of the non-totally symmetric vibration mode (B_{3u}) of 44bpy which is usually Raman inactive vibration mode[19–21] The appearance of the non-totally symmetric mode is based on the CT effect between metal surface kept at negative potential where adsorbed 44bpy molecules orientation.[13]

For the case of 22bpy, SERS intensity of Raman bands at 1013, 1172, 1480, 1572 cm^{-1} derive from ring stretching of C-C and C-N and C-H in-plane deformation, and C-C and C-N ring stretching, respectively, also raised as negative sweep (Figure 3-7a).

Molecular orientation of 22bpy against the metal surface were also analyzed from the linear relationship of the relative SERS band intensity at 1310 with 1480 cm^{-1} (Figure 3-7b,c), respectively.[22] The structure of 22bpy changed from cisoid form to the cis form by the negative potential scan as shown in Figure 3-7b.

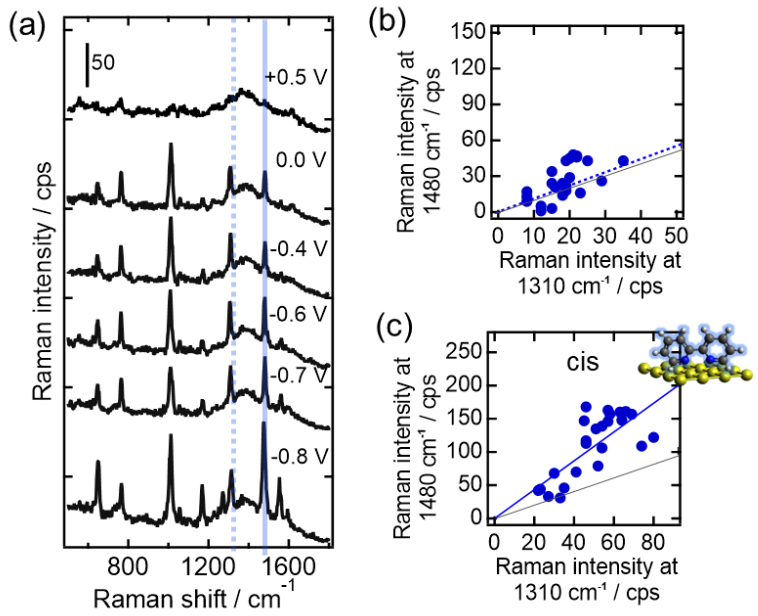

Figure 3-7. Potential dependent series SERS spectra of (a) 1mM 22bpy + 0.1 M $NaClO_4$ aq.. Exposure time is 5 s, incident intensity is 140 μW $μm^{-2}$, potential range from +0.5 V to –0.8 V vs Ag/ AgCl. Correlation plots are made from peak intensity of 1480 cm^{-1} vs 1310 cm^{-1} at (b) 0.0 V and (c) –0.8 V.

As the next step, EC-SERS measurements have been performed in the mixed bi-analyte solution of 44bpy and 22bpy in Figure 3-8. It is interesting that the dominant adsorbate was switched with the potential scan as indicated by the changes in the SERS intensities of 44bpy and 22bpy. Importantly, these changes in the adsorbate species induced by the potential scan have the reversibility with intrinsic orientation for potential as single component (Figure 3-8b, c). The solid and broken lines in the figures correspond to the negative and positive potential, respectively. In the present mixed system, the correlation plots show scattering, which indicates the fluctuation of the orientation in the

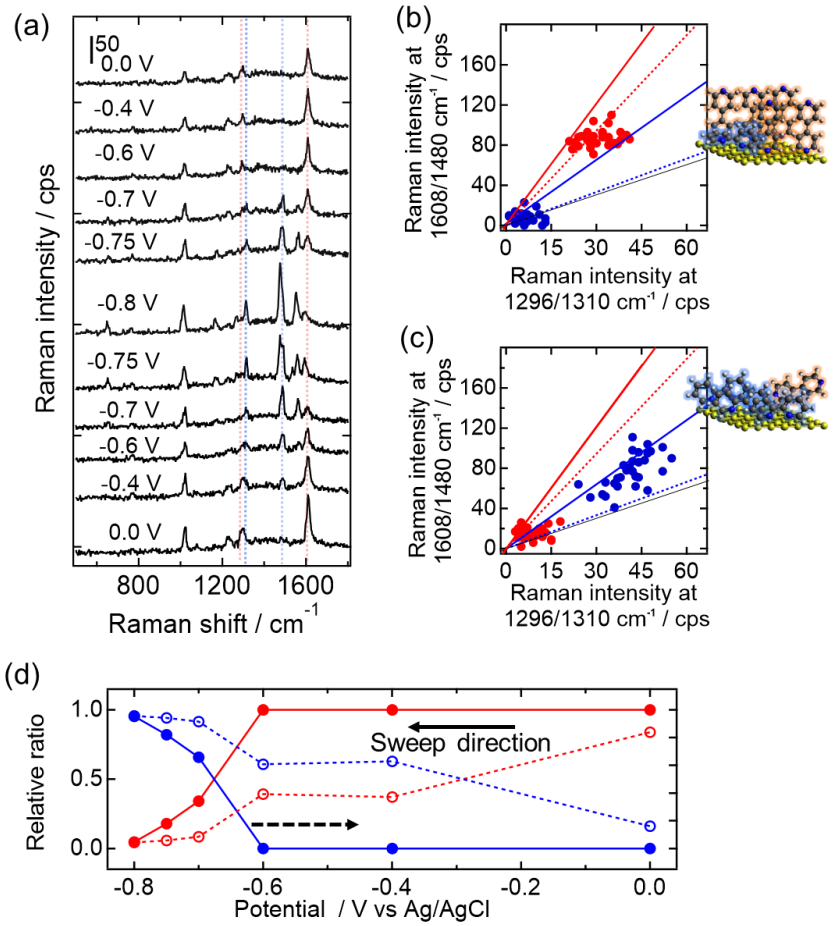

Figure 3-8. (a) Potential dependent series SERS spectra of 1mM 44bpy + 1mM 22bpy + 0.1 M $NaClO_4$ aq. are lined along sweep direction from top to bottom. Exposure time is 1 s, incident intensity is 70 μW μm^{-2}. (b, c) Correlation plots are showed between the peak intensity of 1608 cm^{-1} between 1296 cm^{-1} assigned for 44bpy as red circle. For the 22bpy, correlation plot also made between 1310 cm^{-1} and 1480 cm^{-1} 22bpy as blue circle at (b) 0.0 V and (c) –0.8 V. (d) Relative ratio corresponding to adsorbates on the hot spot Au surface was estimated from peak intensity 1608 cm^{-1} of 44bpy and 1480 $cm^{-1}$of 22bpy which obtained from (a) which contain cathodic scan (solid line) and anodic scan (broken line).

adsorbate of bi-analyte molecules. From the scattering, in such adsorbate of bi-analyte molecular layer, 44bpy and 22bpy would sensitively interact with each other, resulting in the fluctuation of the adsorbed states of molecules. The adsorbed states showing the CT effect could contribute to cause fluctuation with relatively high distribution of intensity at –0.8 V. Thus, it was found that the existence of the isomeric molecules can trigger the characteristic molecular adsorption state beyond the pure system. This phenomenon

implies that the electrochemical control method can selectively control relative ratio of the surface coverage.

From these EC-SERS spectra, the estimate of the coverage ratio of each molecule as the function of electrochemical potential was shown in Figure 3-8d. Each value for Raman ratio of 44bpy and 22bpy was calculated from following Equations with correcting each intensity from single component measurement.

$$Relative\ ratio_{\ 44bpy}$$

$$= \frac{I_{1608\ cm^{-1}} \times \frac{I_{1021 cm^{-1} in\ 1\ mM44bpy}}{I_{1608 cm^{-1} in\ 1\ mM44bpy}}}{I_{1480\ cm^{-1}} \times \frac{I_{1013 cm^{-1} in\ 1\ mM22bpy}}{I_{1480 cm^{-1} in\ 1\ mM22bpy}} + I_{1608 cm^{-1}} \times \frac{I_{1021 cm^{-1} in\ 1\ mM44bpy}}{I_{1608 cm^{-1} in\ 1\ mM44bpy}}} \quad \text{(Equation 3-3)}$$

$$Relative\ ratio_{\ 22bpy}$$

$$= \frac{I_{1480\ cm^{-1}} \times \frac{I_{1013 cm^{-1} in\ 1\ mM22bpy}}{I_{1480 cm^{-1} in\ 1\ mM22bpy}}}{I_{1480\ cm^{-1}} \times \frac{I_{1013 cm^{-1} in\ 1\ mM22bpy}}{I_{1480 cm^{-1} in\ 1\ mM22bpy}} + I_{1608 cm^{-1}} \times \frac{I_{1021 cm^{-1} in\ 1\ mM44bpy}}{I_{1608 cm^{-1} in\ 1\ mM44bpy}}} \quad \text{(Equation 3-4)}$$

In the positive potential region, the dominant surface adsorbate is 44bpy. As reported before, 44bpy molecules show much stronger adsorption characters compared to that for 22bpy. However, it was revealed that adsorbed molecules selectively switching to the Au surface in the potential region more negative than −0.6 V. Interestingly, at the potential was scanned from positive to negative, the hysteresis was observed, reflecting that the contribution of over potential to desorb 22bpy from the Au surface.

3.3.4 Condensation behavior depending on the molecular concentration

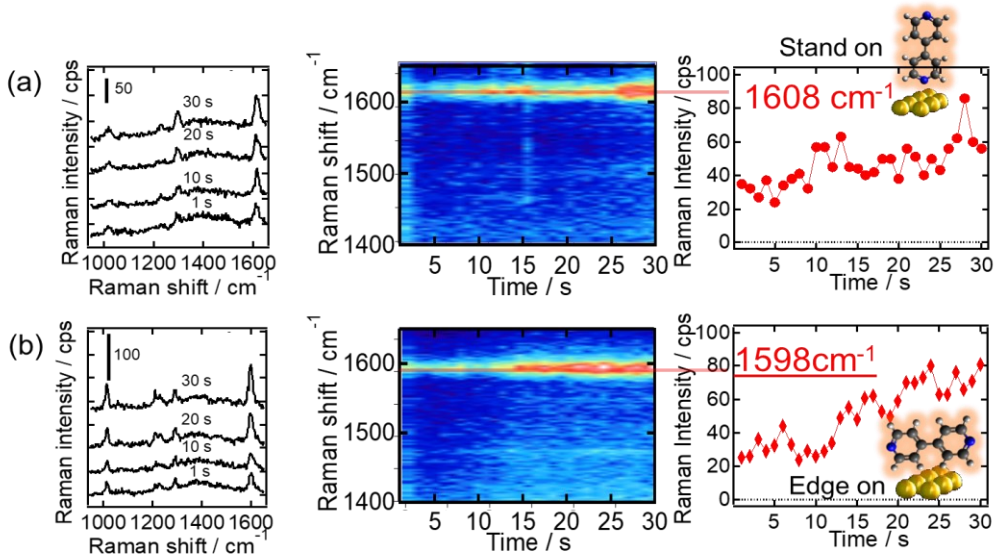

Figure 3-9. Time series SERS spectra with 2D-expression (from 1400 to 1650 cm^{-1}) of 1 mM 44bpy + 0.1 M $NaClO_4$ aq. at (a) 0 V and (b) –0.8 V vs. Ag/ AgCl. The higher intensity area is colored as red and the lower intensity area as blue. RiThe rightanels show Raman intensity of 1608 cm^{-1} (assigned for 44bpy) for a time as a red maker. t_{ex}: 30 s, I_{ex}: 140 μW $μm^{-2}$.

In order to probe detailed behavior of molecules on the surface at the gap of the single bowtie structure, time-series EC-SERS measurements have been conducted at 0 and −0.8 V. The 2D-expression of SERS spectra as the function of the laser light illumination time under the electrochemical potential control are also indicated. The time dependent changes in the scattering intensities at 1608 cm^{-1}, corresponding to the edge-on state of 44bpy, show linear increment with illumination time and stable orientation at both potential. This phenomenon is expected to be due to the suppression of surface diffusion motion in the localized electric field as a result of the molecules affected by plasmon induced electric field. In addition, at a negative potential of -0.8 V, the scattering intensity showed a steeper increase than that observed at 0 V. It is suggested that in the negative potential region, there may be a strong modulation of molecular

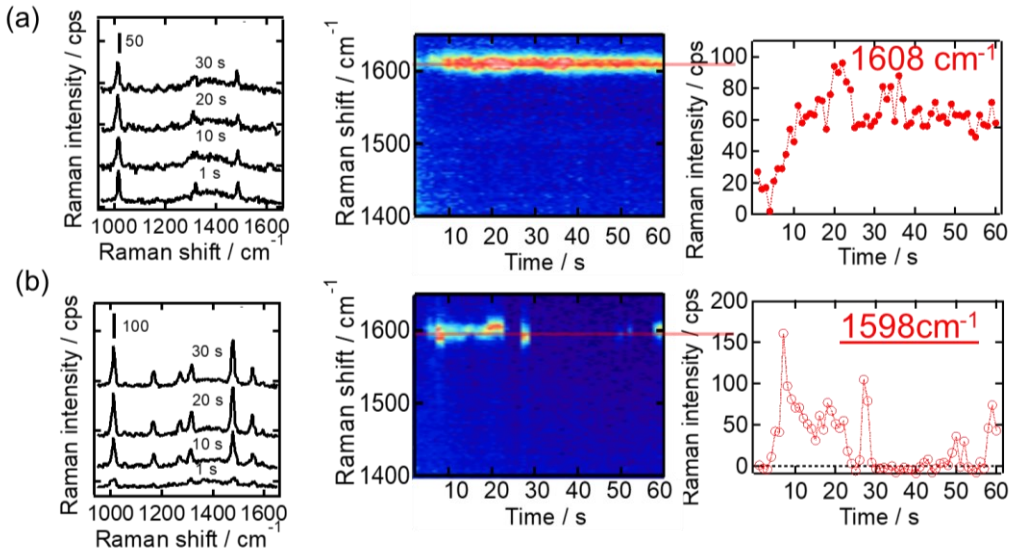

Figure 3-10. Time series SERS spectra with 2D-expression (from 1400 to 1650 cm^{-1}) of 1 μM 44bpy + 0.1 M $NaClO_4$ aq. at (a) 0 V and (b) –0.8 V vs. Ag/ AgCl. The higher intensity area is colored as red and the lower intensity area as blue. RiThe rightanels show Raman intensity of 1608 cm^{-1} (assigned for 44bpy) for a time as a red maker. t_{ex}: 30 s, I_{ex} : 140 μW $μm^{-2}$.

motion due to the effect of resonance processes. To confirm this modulation of molecular motion in the presence of light, the same experiment with a solution diluted to 1/1000 of the concentration condition is performed with same experimental condition.

Even under dilute solution conditions, SERS originating from 44bpy was observed, and although the intensity fluctuated widely, especially at 0 V, an increase in scattering intensity was observed within the light illumination. In contrast, at -0.8 V, molecular motion by two-dimensional diffusion was dominant, and the scattering intensity was not stable and did not show a constant increase during the irradiation time. The vibrational mode appearing at 1608 cm^{-1} at -0.8 V switched with that at 1598 cm^{-1} in second by second. Even in the CT resonance state at -0.8 V, the 44bpy molecule is not completely trapped and leaves the hot spot. Intermolecular interactions are the main cause of the difference between the high concentration solution and the dilute solution. I also examined the potential change in the single-component system of the 22bbpy molecule.

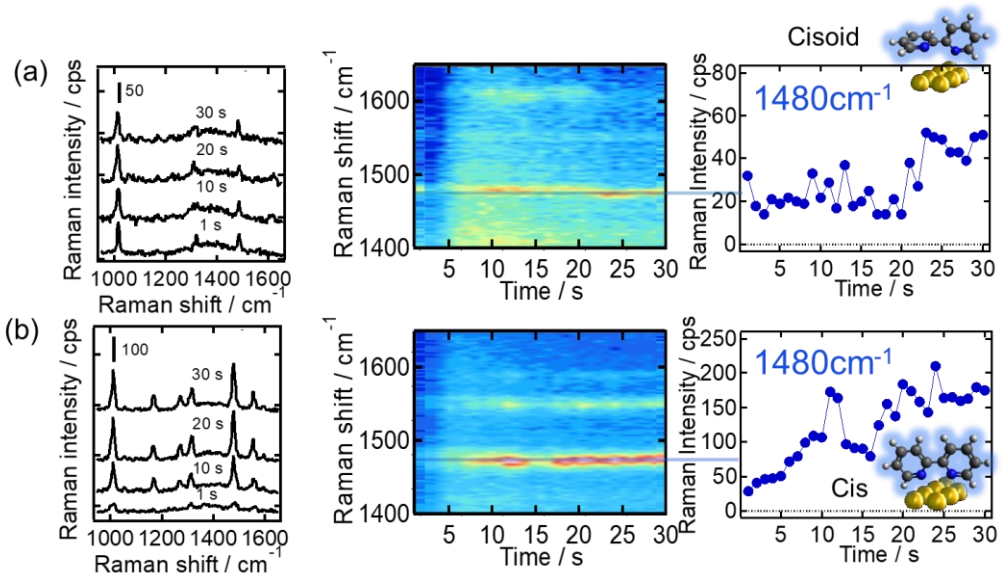

Figure 3-11. Time series SERS spectra with 2D-expression (from 1400 to 1650 cm^{-1}) of 1 mM 22bpy + 0.1 M $NaClO_4$ aq. at (a) 0 V and (b) –0.8 V vs. Ag/ AgCl. Higher intensity area is colored as red and lower intensity area as blue. Right panels show Raman intensity of 1608 cm^{-1} (assigned for 44bpy) for time as a red maker. t_{ex} : 30 s, I_{ex} : 140 μW $μm^{-2}$.

Time series SERS in high concentration condition of 1 mM 22bpy (Figure 3-11) show a slight increase in the number of surface adsorbed molecules with illumination time as like as 1 mM 44bpy solution. The increase in scattering intensity at the positive potential is relatively less than at negative potential as expected from switching behavior in Figure 3-8. For the case of 1 μM 22bpy it is found that at 0 V, almost no spectra were observed, and at -0.8 V, although a strong scattering intensity was observed momentarily, the diffusion was dominated with strong fluctuations in the illumination in Figure3-12. Similar to 44bpy, the trapped molecules do not stop at negative potentials, indicating that the low molecular coverage in dilute solution needs to be considered.

The results obtained for the two types of bpy at different concentrations prove that it is possible to modulate the effect of light pressure on molecules by modulating the electrochemical potential, especially negative potential, intermolecular interaction is also

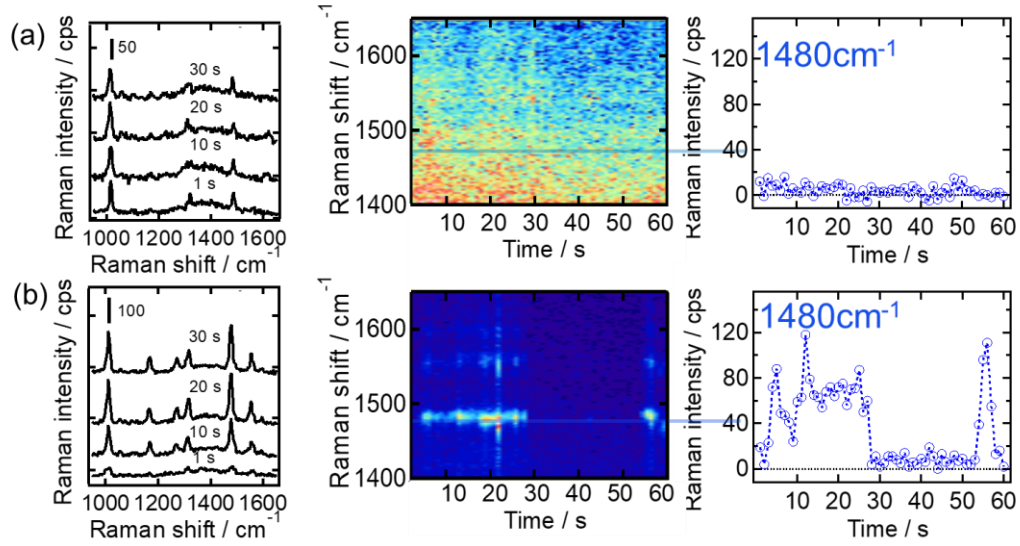

Figure 3-12. Time series SERS spectra with 2D-expression (from 1400 to 1650 cm^{-1}) of 1 μM 22bpy + 0.1 M $NaClO_4$ aq. at (a) 0 V and (b) –0.8 V vs. Ag/ AgCl. Higher intensity area is colored as red and lower intensity area as blue. Right panels show Raman intensity of 1608 cm^{-1} (assigned for 44bpy) for time as a red maker. t_{ex} : 30 s, I_{ex} : 140 μW $μm^{-2}$.

important to stable trapping. In order to achieve selective molecular manipulation and more precise understanding of plasmonic molecular trapping, In the next experiment a bi-analyte system with a dilute mixture of each molecule was examined.

3.3.5 Molecular number estimation of trapped molecules

Time series SERS spectra have been obtained by using the different light intensity in the bi-analyte solution of 1 μM 44bpy and 1 μM 22bpy in 0.1 M $NaClO_4$ aq. under the constant potential at −0.8 V from Au single bowtie (triangle: 100 nm × 120 nm × 30 nm) in Figure 3-13. In the bottom columns of figure, the time series changes in the Raman intensity at 1597 cm^{-1} (44bpy) and 1478 (22bpy) cm^{-1} are plotted in the laser illumination time. For the discussion about the incident light intensity dependence,

intensity plots have been standardized by dividing scattering intensity with incident intensity based on the assumption that Stokes Raman intensities linearly increase with increasing the incident intensity. [24-25] In the bi-analyte solution, the 22bpy is preferably adsorbed to the Au surface but, considering the present low concentration, the Au surface is not fully covered with 22bpy and several amounts of 44bpy also exist at the surface. Interestingly, not only the increase of number of molecules with the time for the illumination, but also the selective increase of 22bpy were clearly observed under the relatively stronger light illumination. It is noted that such SERS intensity increments were not observed under the lower intensity than 35 μW μm^{-2} and even though 140 μW μm^{-2}

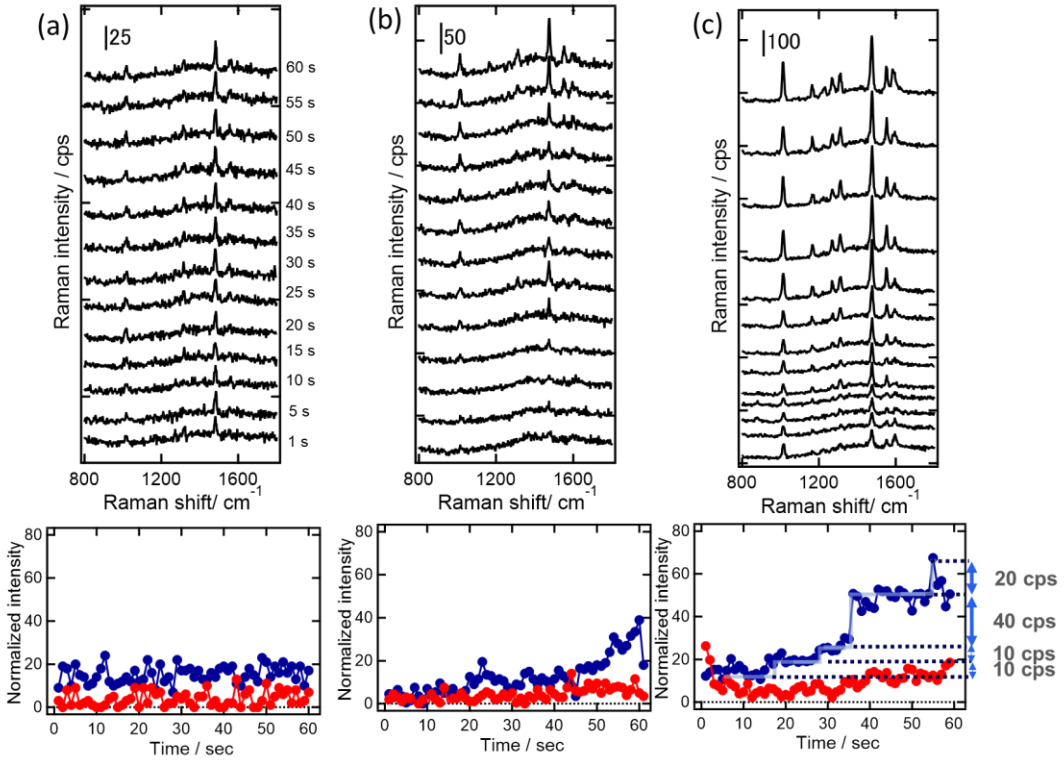

Figure 3-13. Time series spectra of 1μM 44bpy + 1μM 22bpy 0.1 M $NaClO_4$ aq. are obtained each 1 s at –0.8 V vs. Ag / AgCl under illumination in 60 s with incident intensity: I_{ex} (a) 35, (b) 70 and (c) 140 μW μm^{-2}, from bottom to top. Bottom intensity plot is extracted from these spectra with standardization as dividing intensity by incident intensity.

in the only single component shown in Figure3-12. This SERS intensity increase would imply the changes in the number of molecules at the observation site induced by the light illumination. Considering this fact and the light intensity dependence, it can be expected that observed results would be correlated with the effect of the plasmonic field because the F_{opt} is linearly increasing depending on the incident light intensity (Equation 1-4).

From Figure 3-13, the intensity plot looks like stepwise increment, then the histogram distribution was conducted to estimate amount change under illumination. To support quantitative analyses, the standard deviations were calculated in the background regions without any significant peak of 22bpy (σ_{22}) and 44bpy (σ_{44}) from 1400 - 1470 cm^{-1} and 1630 - 1700 cm^{-1}, respectively. Normalized deviations were also calculated by dividing deviations by incident intensity ratio (σ_{22}' and σ_{44}'). These normalized background deviations show that spread of the peak interval (Figure 3-13c) is more significant than the fluctuation of the background (σ').

Table 3-1. Background standard deviation (σ) near each characteristic vibration mode (1400-1470 cm^{-1} region for 22bpy / 1630-1700 cm^{-1} region for 44bpy) and normalized deviation (σ') divided by incident intensity ratio at −0.8 V

Incident intensity [μW μm^{-2}]	σ_{22} [cps]	σ_{44} [cps]	σ'_{22} [cps]	σ'_{44} [cps]
35	3.79	1.41	3.79	1.41
70	6.19	5.49	3.09	2.74
140	10.7	8.13	2.67	2.03

The x-axis in Figure 3-14 represents the Raman intensity of the specific Raman band and the y-axis indicates how many times the specific intensity was observed in 60

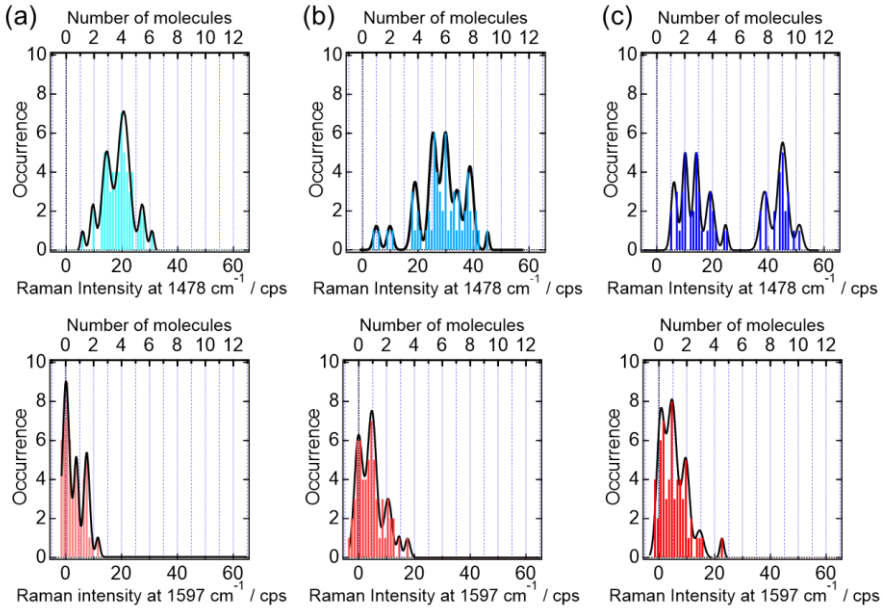

Figure 3-14. Intensity histograms were extracted from time series SERS spectra in Figure 3-13. These occurrences are described as a function of the peak intensity of (a) 1478 cm^{-1} (upper panels)and (b) 1597 cm^{-1} (bottom panels) in 60 s exposure time. Panels are arranged in order of incident intensity I_{ex} : (a) 35, (b) 70, (c) 140 μW μm^{-2}, from left to right, In the histogram, lines show intensity dispersion plotted with Gaussian fitting curve.

s. In Figure 3-14a, b the Raman band intensities at 1478 cm^{-1} (22bpy) are dispersed at around 20 and 30 cps with the intensity of 35 and 70 μW μm^{-2}, respectively. On the other hand, in the case for the relatively strong incident intensity with 140 μW μm^{-2} (Figure 3-13c), two dispersion centers appeared at around 10 and 45 cps corresponding to the initial and latter parts of observations or intensity jump in Figure 3-13c.From these quantitative estimations of number of molecules at the hot spot, the occurrence of selective 22bpy condensations in the bi-analyte solution under the electrochemical potential control was successfully implied. From the above calculations and the Lorentz fitting shown as the black lines, it was found that about five counts for each peak were equivalent to the signal from the single molecule. Thus, it allows us to evaluate that the number of 22bpy molecules verified from 4 to 9 as intensity changes from 35 to 140 μW μm^{-2}. At the same time, the slight increment of the number of 44bpy molecules can be recognized from the

same estimation. At the present experiments, I have observed the small size region with around 100 nm^2 shown in Figure 3-3a as hot spot, which was expected main source to SERS signals from the FDTD calculations. Previously documented results showed the respective surface coverage of 22bpy and 44bpy was less than 10% in 1 μM solution at room temperature under the dark condition. Thus, considering the concentration, size of molecules, and the Langmuir adsorption isotherm, the number of molecules at 100 nm^2 region could be estimated as around 1 molecule, promised by the estimated number of increased molecules in experimental results.

3.3.6 Condensation by adsorbate interaction and charge transfer resonance

For the distinguish charge transfer effect and molecular interaction under condensation in bi-analyte solution, the spectral fitting was conducted. As discussed above, the gradual increase of the scattering intensity, indicating the increment of the changes in the number of molecules at the hot spot of Au single bowtie (triangle: 100 nm × 150 nm × 30 nm), were confirmed in 22bpy cases especially under the stronger light intensity condition with longer illumination at −0.8 V in Figure 3-15.

In Figure 3-15b, SERS spectra collected at 100 s with different laser intensity were depicted with Lorentz fitting. In the case for 22bpy molecules, the spectrum shape was independent on the laser intensity while the Raman band for 44bpy at 1600 cm^{-1} became broaden with increasing light intensity. This broadening peak can be deconvoluted into two peaks, corresponding to 1608 cm^{-1} (brown area) and 1597 cm^{-1}

(red area) assigned to ring stretching (C-C, C-N) modes and non-totally symmetric mode. Especially, the non-totally symmetric mode at 1597 cm^{-1} is the characteristics to the occurrence of the resonant charge transfer (CT) between the Fermi level of Au and molecules. It was found that light illumination with relatively strong intensity leads to the effective CT condition. Previous report show that the α' of the molecule under the resonant condition is almost ten times larger than that with the non-resonant state, resulting in ten times higher efficiency of molecular trapping.[6] Taking this facts into considerations, when the distinct condensation of 22bpy occurs, at the same time the F_{opt} to 44bpy is enhanced up to ten times because of the CT state. In other words, 22bpy molecules which preferably absorbed to the negatively charged surface were condensed with the help by 44bpy molecules feeling much stronger F_{opt}, comparably to Figure 3-12.

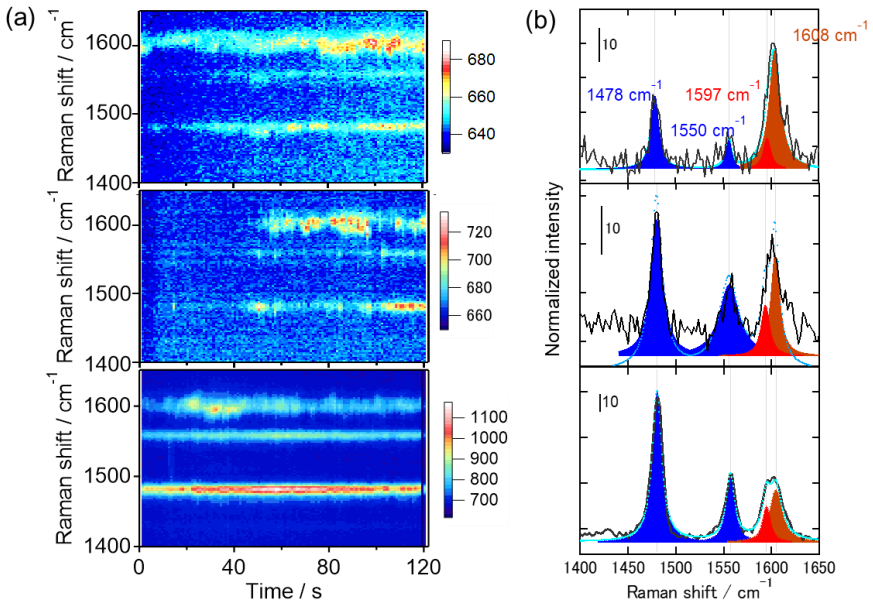

Figure 3-15. 2D-expression of time series SERS spectra of 1 μM 44bpy + 0.1 M $NaClO_4$ aq. at -0.8 V vs. Ag/ AgCl. 1608 cm^{-1} (assigned for 44bpy) as red solid line, 1480 cm^{-1} (assigned for 22bpy) as a blue broken line. t_{ex}: 60 s, I_{ex}: 35, 70, 140 μW μm^{-2} from top to bottom. (b) Normalized SERS spectra by incident laser intensity collected at laser illumination time of 100 s. Lorentz fitting peaks at 1608 and 1597 cm^{-1} are represented as brown and red areas(44bpy). The fitting peaks at 1478 and 1550 cm^{-1} (22bpy) are shown as blue. Light blue dots show total fitting area of these fitting peaks.

These facts would imply that the actual F_{opt} applied to 22bpy and 44bpy molecules in the mixed solution could be higher than those estimated from the values of polarizability of isolated molecule. When the molecules interact with each other, the domain like structure often forms. In the case for the bipyridine molecules, it is need to take account that π-π stacking results in the formation of the molecular layer.[26-28] It is known that the domain structures lead to the improvement of the α' compared to that of single molecule, leading to the relatively large trapping potential.[28] The domain like structure formation can be expected during the condensation. Note that, because of the present dilute condition, the molecular interaction would be less at the initial stage of the light illumination, however, at the condensed stage by illumination it is never ignorable to interact with each other. Here, repetitive long-time exposure experiment with dark interval can be the answer to this question. Because the surface diffusion of the domain structure at Au surface is much suppressed under the thermal equilibrium condition without light, the repetitive light illumination with dark intervals enables to vitalize effects of the domain structures on the molecular condensation at single Au bowtie gap (triangle: 100 nm × 200 nm × 30 nm).

The upper parts of Figure 3-16 show the 2D-expression SERS intensity collected by the four times continuous laser illumination for 60 s with the dark interval of 60 s as black square in figure, which images is colored with respective intensity at each illumination. The electrochemical potential was kept at −0.8 V, enabling the resonant charge transfer for 44bpy. The middle parts of Figure 3-16 indicate the scattering intensities at 1478 cm^{-1} (blue bars) and 1597 cm^{-1} (red bars). The band intensities at 1608 cm^{-1} (brown bars) are also indicated at the opposite sides to them for the comparison of

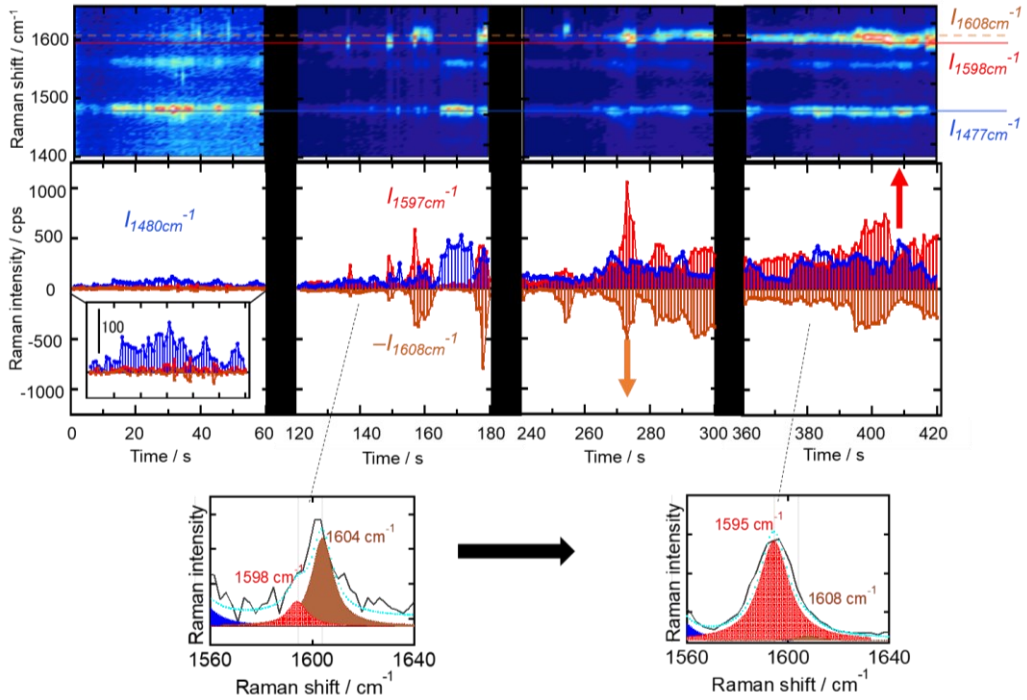

Figure 3-16. Time series SERS spectra of 1 μM 44bpy + 1 μM 22bpy + 0.1 M $NaClO_4$ aq. at –0.8 V vs. Ag/ AgCl, t_{ex} : 60 s, I_{ex} : 140 μW μm^{-2}. The middle panels show peak intensity of 1597 cm^{-1} (assigned for 44bpy charge transfer state corresponding to solid red line in 2D-expression) as red sticks, 1608 cm^{-1} (assigned for 44bpy corresponding to dashed red line) as brown bars for down direction, and 1478 cm^{-1} (assigned for 22bpy corresponding to solid blue line) as blue makers. The black squares correspond to the time without illumination. Bottom spectra are taken from second illumination and fourth illumination, respectively with peak decomposition.

changing 44bpy adsorbed states under illumination. In the left column corresponding to the first-time illumination, 22bpy molecules seem to be selectively trapped, which is good agreement with above results. In the dark condition, the condensed 22bpy molecules formed by the light illuminations would be partially dispersed from hot spot and 44bpy molecules get the space to adsorb. Thus, early parts in the second illumination, both 22bpy and 44bpy exist on the SERS hot spot as can be seen intensity. On the other hand, in the latter parts of the second panel, the intensities for both molecules become gradually stronger than those in the first-time illuminations, originating from the increments of the molecular interactions. As evidence for the formation of the domain structure, the SERS

intensities for both 22bpy and 44bpy are maintained at the biggening of the third time laser illumination even after the dark interval. In the third and fourth illumination, it was observed that the repeated light and dark process gave further condensation. Especially for the 44bpy molecule, although the 44bpy fluctuates, the intrinsic vibration of the 44bpy molecule (1597 cm^{-1}) excited under the CT resonance appears mainly in the condensed phase in the fourth illumination compared to the spectrum in the second illumination shown at the bottom of Figure 3-16. The CT resonance caused the 44bpys to suppress surface diffusion due to the large dipole and large polarizability, as can be seen in the intensity plots. Incidentally, the fourth time illumination, although the SERS intensity is much more fluctuated, more than 10 times the number of molecules were condensed at the hot spot in both 22bpy and 44bpy Therefore, it can be said that the molecular behavior in the bi-analyte solution is determined not only by the effect of F_{opt} on each molecule, but also by the interaction between the molecules in the domain structures, resulting in stable adsorption. This means that the unique molecular condensation was achieved by the synergistic influence of F_{opt} and the attractive force between molecules at the electrified interface.

3.4 Conclusion

Consequently, I have proved that it is possible to achieve the small size molecular trapping under ambient conditions and electrochemical conditions at a single hotspot. The adsorbed molecules on the metal surface can be controlled by the electrochemical potential, which defines the molecular orientation and adsorption stability, even though two components are dissolved in water. Molecular switching occurs rapidly on the Au surface in 1 mM solution (Figure 3-8). In addition, for 1 mM single component solution of 44bpy or 22bpy, the number of molecules is linearly increased by illumination on plasmon structure at specific electrochemical potential. In particular, although the single-component experiment did not show a clear linearity for the intensity increment with illumination in the 1000-fold diluted solution (1 μM), in the bi-analyte condition up to 90-fold increment of the initial number of adsorbates was achieved. Considering the fact that the binding energy of π-π stacking in pyridine dimer reached the 32 / 16 kJ mol^{-1} for antiparallel / parallel configuration, respectively, the control of the molecular orientation by the electrochemical potential control should be the key factor for the realization of the small size molecular trapping as monolayer aggregation. As a proof of this point, the molecular trapping behaviors have the difference between in the single-component solution under the much higher concentration condition (1 mM) and lower concentration (1 μM). This is because under such higher concentration conditions, the metal surface is completely covered with the molecules, leading to strong interaction with each other.

It was also found that charge transfer resonance plays an important role in molecular condensation. The plasmon-assisted molecular condensation overcomes the adsorption equilibrium defined by the thermal isotherm. In other words, plasmon-assisted molecular condensation under ambient conditions is established in the present manner.

Moreover, curious behaviors are observed for the bi-analyte system as a unique condensation phase, where many effectively break the physical limit for molecular manipulation.

3.5 References

(1) Bradac, C. Nanoscale Optical Trapping: A Review. Adv. Opt. Mater. 2018, 6 (12), 1–26.

(2) Ebbesen, T. W. Hybrid Light-Matter States in a Molecular and Material Science Perspective. Acc. Chem. Res. 2016, 49 (11), 2403–2412.

(3) Sonntag, M. D.; Klingsporn, J. M.; Zrimsek, A. B.; Sharma, B.; Ruvuna, L. K.; Van Duyne, R. P. Molecular Plasmonics for Nanoscale Spectroscopy. Chem. Soc. Rev. 2014, 43 (4), 1230–1247.

(4) Kravets, V. G.; Kabashin, A. V.; Barnes, W. L.; Grigorenko, A. N. Plasmonic Surface Lattice Resonances: A Review of Properties and Applications. Chem. Rev. 2018, 118 (12), 5912–5951.

(5) Alpeggiani, F.; D'Agostino, S.; Sanvitto, D.; Gerace, D. Visible Quantum Plasmonics from Metallic Nanodimers. Sci. Rep. 2016, 6 (1), 34772.

(6) Xu, H.; Käll, M. Surface-Plasmon-Enhanced Optical Forces in Silver Nanoaggregates. Phys. Rev. Lett. 2002, 89 (24), 246802.

(7) Oikawa, S.; Minamimoto, H.; Murakoshi, K. Reversible Electrochemical Tuning of Optical Property of Single Au Nano-Bridged Structure via Electrochemical under Potential Deposition. Chem. Lett. 2017, 46 (8), 1148–1150.

(8) Dodson, S.; Haggui, M.; Bachelot, R.; Plain, J.; Li, S.; Xiong, Q. Optimizing Electromagnetic Hotspots in Plasmonic Bowtie Nanoantennae. J. Phys. Chem. Lett. 2013, 4 (3), 496–501.

(9) Albrecht, A. C. On the Theory of Raman Intensities. J. Chem. Phys. 1961, 34 (5), 1476–1484.

(10) Kneipp, K.; Kneipp, H.; Manoharan, R.; Itzkan, I.; Dasari, R. R.; Feld, M. S. Surface-Enhanced Raman Scattering (SERS)-a New Tool for Single Molecule Detection and Identification. Bioimaging 1998, 6 (2), 104–110.

(11) Ashkin, A.; Dziedzic, J. M. Optical Trapping and Manipulation of Viruses and Bacteria. Science 1987, 235 (4795), 1517–1520.

(12) Misawa, H.; Koshioka, M.; Sasaki, K.; Kitamura, N.; Masuhara, H. Three-dimensional Optical Trapping and Laser Ablation of a Single Polymer Latex Particle in Water. J. Appl. Phys. 1991, 70 (7), 3829–3836.

(13) Yonezawa, Y.; Minamimoto, H.; Nagasawa, F.; Takase, M.; Yasuda, S.; Murakoshi, K. In-Situ Electrochemical Surface-Enhanced Raman Scattering Observation of Molecules Accelerating the Hydrogen Evolution Reaction. J. Electroanal. Chem. 2017, 800, 7–12.

(14) Park, W.-H.; Kim, Z. H. Charge Transfer Enhancement in the SERS of a Single Molecule. Nano Lett. 2010, 10 (10), 4040–4048.

(15) Wandlowski, T.; Ataka, K.; Mayer, D. In Situ Infrared Study of 4,4'-Bipyridine Adsorption

on Thin Gold Films. Langmuir 2002, 18 (11), 4331–4341.

(16) Yang, D.; Bizzotto, D.; Lipkowski, J.; Pettinger, B.; Mirwald, S. Electrochemical and Second Harmonic Generation Studies of 2,2'-Bipyridine Adsorption at the Au(111) Electrode Surface. J. Phys. Chem. 1994, 98 (28), 7083–7089.

(17) Mayer, D.; Dretschkow, T.; Ataka, K.; Wandlowski, T. Structural Transitions in 4,4′-Bipyridine Adlayers on Au(111)—an Electrochemical and in-Situ STM-Study. J. Electroanal. Chem. 2002, 524–525, 20–35.

(18) Brolo, A. G.; Jiang, Z.; Irish, D. E. The Orientation of 2,2′-Bipyridine Adsorbed at a SERS-Active Au(111) Electrode Surface. J. Electroanal. Chem. 2003, 547 (2), 163–172.

(19) Konishi, T.; Kiguchi, M.; Takase, M.; Nagasawa, F.; Nabika, H.; Ikeda, K.; Uosaki, K.; Ueno, K.; Misawa, H.; Murakoshi, K. Single Molecule Dynamics at a Mechanically Controllable Break Junction in Solution at Room Temperature. J. Am. Chem. Soc. 2013, 135 (3), 1009–1014.

(20) Topaçli, A.; Akyüz, S. 4,4′-Bipyridyl: Vibrational Assignments and Force Field. Spectrochim. Acta Part A Mol. Spectrosc. 1995, 51 (4), 633–641.

(21) Mayer, D.; Dretschkow, T.; Ataka, K.; Wandlowski, T. Structural Transitions in 4,4′-Bipyridine Adlayers on Au(111) - An Electrochemical and in-Situ STM-Study. J. Electroanal. Chem. 2002, 524–525, 20–35.

(22) Luo, Z.; Loo, B. H.; Cao, X.; Peng, A.; Yao, J. Probing the Conformational Transition of 2,2′-Bipyridyl under External Field by Surface-Enhanced Raman Spectroscopy. J. Phys. Chem. C 2012, 116 (4), 2884–2890.

(23) Kneipp, K.; Kneipp, H. SERS Signals at the Anti Stokes Side of the Excitation Laser in Extremely High Local Optical Fields of Silver and Gold Nanoclusters. Faraday Discuss. 2006, 132, 27–33.

(24) Lombardi, A.; Schmidt, M. K.; Weller, L.; Deacon, W. M.; Benz, F.; de Nijs, B.; Aizpurua, J.; Baumberg, J. J. Pulsed Molecular Optomechanics in Plasmonic Nanocavities: From Nonlinear Vibrational Instabilities to Bond-Breaking. Phys. Rev. X 2018, 8 (1), 011016.

(25) Mishra, B. K.; Sathyamurthy, N. π-π Interaction in Pyridine. J. Phys. Chem. A 2005, 109 (1), 6–8.

(26) Hohenstein, E. G.; Sherrill, C. D. Effects of Heteroatoms on Aromatic π-π Interactions: Benzene-Pyridine and Pyridine Dimer. J. Phys. Chem. A 2009, 113 (5), 878–886.

(27) Dougherty, D. A. The Cation-π Interaction. Acc. Chem. Res. 2013, 46 (4), 885–893.

(28) Ghanty, T. K.; Ghosh, S. K. Correlation between Hardness, Polarizability, and Size of Atoms, Molecules, and Clusters. J. Phys. Chem. 1993, 97 (19), 4951–4953.

Chapter 4

Control of interfacial water at electrified nanostructure interface

4.1 Introduction

At present, the efficient controls of the electrochemical reactions are based on the investigations of high catalytic electrode materials. If the control of the interfacial structure of water molecules was achieved, the innovation of chemical reactions pathways would be realized. From this point of view, the precise manipulation of water molecules at the electrode interface including polariton states could be a breakthrough to chemical reaction control. The structure of water network consists of hydrogen bonds. Many researchers have used electronic excitation spectroscopy with X-rays and vibrational spectroscopies of infrared absorption and Raman scattering to observe the complex structure of water at both the microscopic and macroscopic levels.[1–4] In addition to the variety of structures formed by hydrogen bonding, changes in orientation and density with potential gradient depending on morphologies and solvated ions at the interface have also been studied..[5–8] In these areas, the behavior of water molecules at metal interfaces and their modulations by electrochemical SERS have been studied. Control of the electrochemical potential changes the orientation of water molecules to the electrode surface, and polarization rates from one to several molecular layers have been observed from Raman scattering spectra..[9,10] In these previous studies, not only the stretching vibration (about 3200-3600 cm^{-1}) of water, but also bending vibrations (about 1600 cm^{-1}) and libration (about 400-1000 cm^{-1}) were observed, especially in the overpotential region above the hydrogen evolution potential. This phenomena is considered as CT resonant

Raman because the bending mode and libration are difficult to observe due to the low Raman scattering intensity.[11] These facts suggest that a potential-dependent change in the interfacial water structure and states is essential for understanding electrochemical reactions. In addition, according to the previous study, there would be a possibility for the formation of unique interfacial structures of water molecules on the nanostructured Ag surface, resulting in the changes in isotope selectivity.[12] On the other hand, there are still many unclear points regarding to the effects of localized electric field strength under polarized surface. In this chapter, I describe the results of experiments conducted in the initial and high overpotential region of the hydrogen evolution reaction (HER) and the bubble generation region to clarify these issues. To verify the response of the formation of unique water structures on nanostructured Ag surfaces in isotopic mixtures to the electrochemical potential, high static pressure in-situ electrochemical Raman scattering measurements were performed.

4.2 Experimental method

4.2.1 Set-up of static pressured electrochemical Raman cell

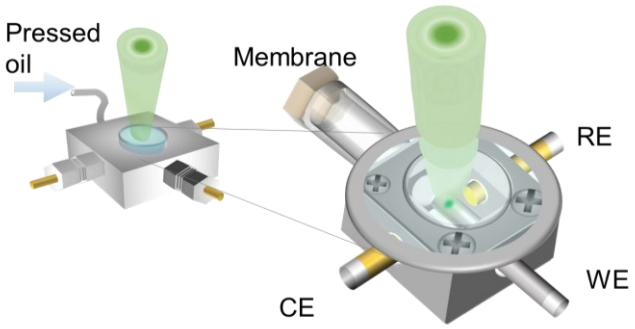

Figure 4-1. Schematic illustration of the static pressured electrochemical cell in the outer cell with transparent window for spectroscopy

To perform electrochemical measurements under high pressure using an inverted Raman spectroscopy setup (Nanofinder30, Tokyo Instruments Inc.), I constructed the pressure tunable electrochemical cell system with a transparent window to observe the interfacial structure at the hydrogen evolution potential (Figure 4-1). A 514 nm laser (exit intensity of 5.0 -8.3 mW) was used with a 50x long-range objective lens to focus the light on the electrode surface through the transparent windows and pressure oil. The electrochemically roughened Ag wire and two Au wire electrodes are connected with outer wires as working, counter, and reference electrodes, respectively. The membrane tube is inserted into the cell to adjust the hydrostatic pressure in the inner cell to the external oil. The solution volume was about 100 μL and the pressure range was 0.1 MPa to 75 MPa. In this system, the maximum solubility of hydrogen was calculated to be nearly 0.5 mol/L at 296 K under 75 MPa, up to about 50 μmol of hydrogen gas in the cell.[13] The Au electrodes (CE and RE as quasi-reference electrode) were washed by immersing in a 1:1 mixture of sulfuric (95% mass) acid and nitric acid (60 % mass) for at least 15 minutes, followed by washing with mill-Q water and boiling to remove

adsorbed ions. The Ag WE were immersed in sulfuric acid for at least 15 minutes and then washed with mill-Q water and boiled as same as case for Au. The process of electrochemical roughening of the Ag electrode is shown in the next section. Sample solutions with supporting electrolytes of $NaClO_4$, Na_2SO_4 and Cs_2SO_4 are prepared with different water isotope compositions as in Table 4-1.

Table 4-1: Solution preparation for isotope mixed Raman measurement

Prepared ratio H_2O : D_2O	$NaClO_4$ [mM]
1 : 0	100
1 : 0	500
1 : 1	500
1 : 5	500
1 : 10	100
1 : 10	500
0 : 1	500
Prepared ratio H_2O : D_2O	Na_2SO_4 [mM]
1 : 1	250
Prepared ratio H_2O : D_2O	Cs_2SO_4 [mM]
1 : 1	250

4.2.2 Sample fabrication of Ag electrode by oxidation-reduction cycle

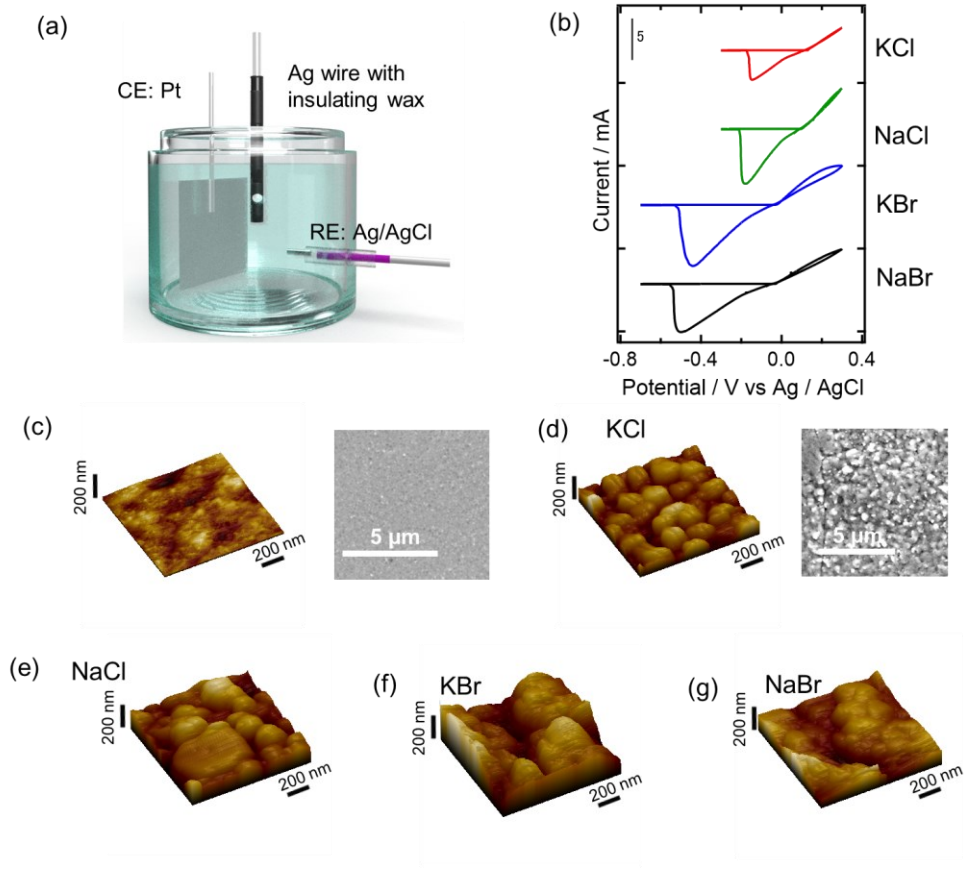

Figure 4-2. (a) Schematic picture and (b) cyclic voltammogram of waxed Ag electrode in 4 different solutions with Pt as counter electrode and Ag/AgCl as reference electrode. From top to bottom, the CV are taken in 0.1 M KCl, 0.1 M NaCl, 0.1 M KBr, 0.1 M NaBr aq. (c) AFM topology image of (c)Ag (after washed by H_2SO_4), Ag roughened by redox cycle in (d) 0.1 M KCl, (e) 0.1 M NaCl, (f) 0.1 M KBr, (g) 0.1 M NaBr aq.. Inset SEM pictures of (c) and (d) shows roughness of Ag surface.

To roughen the Ag surface, an electrochemical oxidation-reduction cycle (ORC) treatment was performed in various 0.1 M alkali halide solutions (Figure 4-2a). The Ag wire was covered with insulating solid wax (Apiezon W, M&I Materials Ltd.) and partially exposed with an area of about 1 mm^2 before the electrochemical roughening process. In the cyclic voltammogram (CV), the oxidation peak was observed on the positive potential side in Figure 4-2b, while the reduction peak was on the negative

potential side. As shown in the AFM images in Figure 4-2c-g, the size and depth of the Ag grains were distributed from the scale of a few nm to that of 100 nm before and after the ORC treatments. Due to the distribution of the island shape diameter of several 100 nm, the generation of a localized electric field in the vicinity of each of these islands via the plasmon resonance in the visible light region could be expected. Since the roughened Ag in KCl aq. has uniformly smaller size, which was expected to resonate to 514 nm layer for Raman measurement, the Ag wire with 10 cycles of oxidation-reduction process in 0.1 M KCl aq. was used in the subsequent experiments.

4.3 Results and discussion

4.3.1 Pressure-dependent water oxidation and reduction

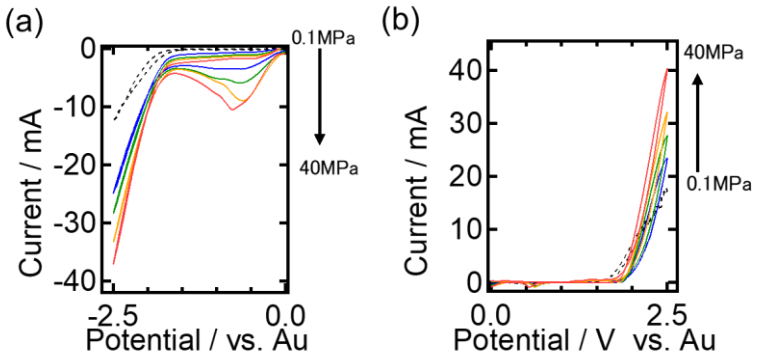

Figure 4-3. Cyclic voltammogram of 0.1 M $NaClO_4$ aq. on Au working electrode vs Au reference electrode with Au counter electrode. Sweep range is from -2.5 V to +2.5 V with 100mV/sec under various static pressure. Expanded cyclic voltammogram (a) from -2.5 V to 0 V and (b) from 1.5 V to +2.5 V under 0.1(broken black), 10(blue), 20(green), 30(yellow), and 40 MPa(red).

The CVs shown in Figure 4-3 correspond to the hydrogen and oxygen evolution under each static pressure from 0.1 MPa to 40 MPa. Note that no particular dependence on sweep rate was confirmed, and the total value of product hydrogen is up to 1 μmol less than the maximum solubility of hydrogen of about 50 μmol in the cell. The diffusion limit due to mass transport also increases exponentially up to −4.0V on the hydrogen generation potential side. This means that electron transfer is the only rate limiting factor. The figures also show that the current values for oxygen evolution and hydrogen evolution increase with static pressure, which is predicted to accelerate charge transfer due to the proximity of water to the interface and the desorption of product molecules from the surface.[14,15] The reduction wave at about −0.8 V is attributed to a reduction of dissolved oxygen molecules generated in the oxygen evolution reactions in the positive potential region. The generation of oxygen molecules at the counter electrode also contributes to the generation of hydrogen at the working electrode.

4.3.2 Electrochemical SERS measurement under static pressures

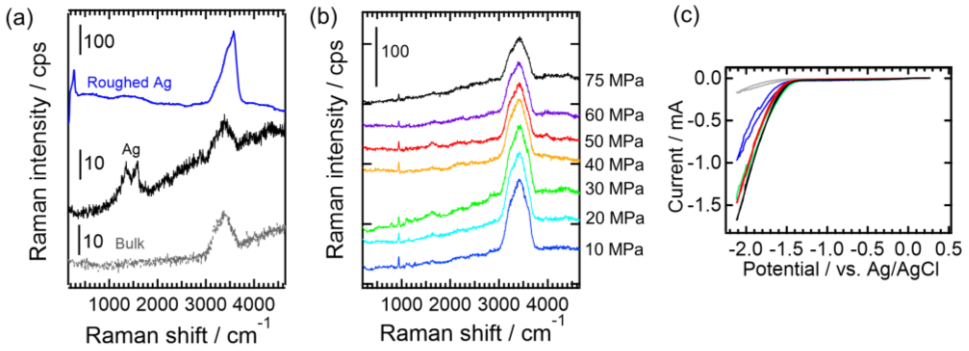

Figure 4-4. (a) Raman spectra of 0.1 M $NaClO_4$ aq. were taken in solution, on Ag surface, and on roughened Ag surface, respectively, under 30 MPa t_{ex}: 10 s. (b) SERS spectra with variety of static pressure of H_2O 0.5M $NaClO_4$ aq. were obtained at −1.42V vs. Ag/AgCl in t_{ex}: 10 s. The static pressure was kept as 10, 20, 30, 40, 50, 60, and 75 MPa from bottom to top. (c) The cyclic voltammogram of 0.5M $NaClO_4$ aq.(H_2O) on roughened Ag are taken with 100 mV/s under different pressured condition, as 0.1 10, 25, 50, and 75 MPa from top to bottom.

Since water vibrational modes have relatively small Raman scattering cross section, Raman spectra of water by confocal laser needs high laser power and longtime exposure with high magnification lens. As a result, the present condition of less than 10 mW of 514 nm laser with x50 objective lens and 10 s exposure time gave weak water signal with stretching mode peak (about 3450 cm^{-1}) in the bulk aqueous solution as shown in Figure 4-4 bottom spectra. A similar trend was also observed on the smooth surface of the Ag electrode. It should be noted that the two peaks at 1328 and 1562 cm^{-1} are assigned to photo activated Ag oxides, which disappeared with a negative sweep in this experimental system.[16–18] On the other hand, SERS from adsorbed water molecules on roughened Ag wire shows the higher intensity of stretching mode due to plasmon enhancement for Raman measurement, even though the observed molecules are limited to interface region of Ag.

The pressure dependent SERS spectra were obtained under electrochemical potential control at −1.42 V vs. Ag/AgCl from 10 to 75 MPa (Figure 4-4b), where the

reduction current is relatively small as shown in Figure 4-4c. The scattering intensity of stretching mode showed relatively stable under each pressured condition, while cyclic voltammogram for cathodic region of Ag shows the obvious increment of reduction current of HER with increasing static pressure.

4.3.3 Interfacial water structure at negative electrochemical potential

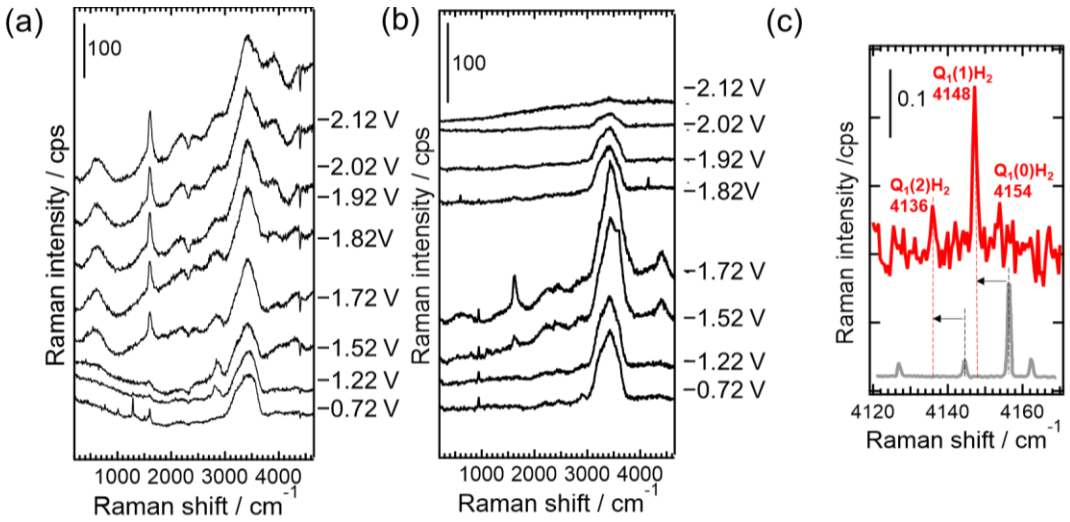

Figure 4-5. Potential dependent series SERS spectra of (a) 0.1 M $NaClO_4$ aq. on roughened Ag surface under 30 MPa and (b) 0.5 M $NaClO_4$ aq. on roughened Ag surface under 50 MPa, in t_{ex}: 10 s, −0.72, −1.22, −1.52, −1.72, −1.82, −1.92, −2.02, and −2.22 V vs. Ag/AgCl from bottom to top . (c) High grating SERS spectra of 0.5 M $NaClO_4$ aq. (H_2O : D_2O = 1: 1) show very narrow vibrational modes of hydrogen gas with spin isomers appeared in negative region at −1.92 V under 50 MPa, in t_{ex}: 60 s. The gray line is 0.1 MPa hydrogen gas as a referred.[20]

Figure 4-5a shows the electrochemical SERS spectra of roughened Ag wire obtained at 30 MPa in 0.1 M $NaClO_4$ aq. The libration mode at 600 cm^{-1}, the bending mode at 1608 cm^{-1}, and the enhanced OH stretching vibration at 3500 cm^{-1} are observed at negative potentials than −1.52 V vs. Ag/AgCl. The peaks of the libration and the

bending modes appeared at above −1.5 V, corresponding to the region where the reduction current occurs due to the HER (Figure4-4c). While the stretching and bending modes are enhanced, the scattering intensities of the libration mode were almost stable at negative potentials below −1.8 V. The peak of the libration mode depends on the arrangements of water molecules and a hydrogen bonding network at the interface.[19] On the other hand, the bending modes are observed in the HER, indicating the possibility that the water interacting with the Ag surface under CT resonance with HER intermediates gives a strong scattering signal.[11] While the amount of interfacial H_2O in the inner Helmholtz layer is considered to be changed to HER intermediate with negative sweep exponentially, the intensity of the bending mode at negative potential became maximum at about −1.92 V. This intensity dependence on electrochemical potential seems to correspond to the amounts of CT resonant intermediates and the matching degree of the resonant states.

Figure 4-5b shows the electrochemical SERS at 50 MPa in 0.5 M $NaClO_4$ aq. with 5 times higher electrolyte concentration than in Figure 4-5a. Both libration and bending modes are observed during the reduction current associated with the HER reaction. The intensity of these modes became stronger at negative potentials as shown in Figure 4-5a. On the other hand, more negative than −1.82 V, the signal at the interface was no longer observed due to bubble effects. The sharp peak in the high wavenumber region consisted of multiple peaks with very small full width at half maximum in Figure 4-5c. This Raman band was similar to that of gaseous hydrogen at atmospheric pressure, but the multiple red shift was observed[20] From this comparison, it was found that the hydrogen gases evolved enormously beyond the dissolution rate, which was characteristically observed especially in the higher electrolyte condition. Thus, it can be summarized that three regions corresponding to the initial region of HER, the steady

region of HER with high coverage of intermediates on Ag, and the excess region of produced hydrogen molecules were confirmed. Therefore, the SERS results on this nanostructured Ag show the interaction of water molecular states and plasmon polariton. To get more insight of each region of HER under interaction with plasmon, I tried the mixed isotope experiment, which allows to analyze the elementary step of HER.

4.3.4 Nanostructure effects for isotope effects on HER

In Figure 4-6a, b, and c, I compared the initial overpotential of HER less than −1.72 V with three samples of 0.5 M $NaClO_4$ dissolved in H_2O: D_2O = 1 : 0, 1 : 1, and 0 : 1, respectively. As the interesting aspects on D_2O existing condition, the specific sharp peak appeared at 2650 cm^{-1} more positive than −1.62 V. This peak is considered as decoupling OD stretching from hydrogen bonding network as a result of hydration to Na^+ according to the study of $NaClO_4$ or NaOH in H_2O under high concentration.[21–23] Instead of the hydrated water as reported in the papers, the intensity was strongly dependent on SERS hotspots throughout my experiments. In other words, the presence of Na^+ hydrated water depended on the nanostructured surface morphology and electrochemical potential. The reason why the strong OD stretching was more clearly observed in these experiments is that the OD hydrogen bonding makes it difficult to delocalize the OD oscillation and form hydrogen bonds with neighboring waters.[24–26] Note that, in H_2O: D_2O = 1 : 1 at −0.72 V, the small peak of OH of hydration at 3600 cm^{-1} corresponds to HOD, which are much more decoupled water molecules in H_2O and D_2O. From Figure 4-6, although the sharp hydration peaks of OD or OH were observed stably

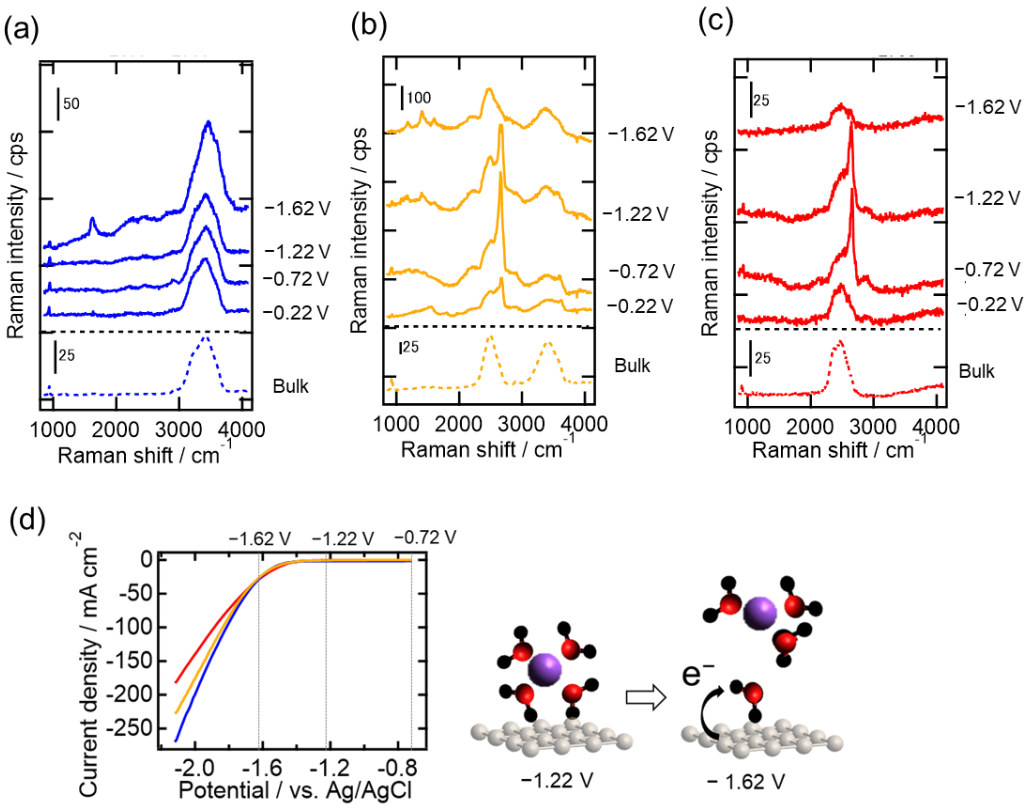

Figure 4-6. Potential dependent series SERS spectra of (a) 0.5 M $NaClO_4$ aq. (H_2O : D_2O = 1 : 0), (b) 0.5 M $NaClO_4$ aq. (H_2O : D_2O = 1 : 1)), (c) 0.5 M $NaClO_4$ aq. (H_2O : D_2O = 1 : 5), and (d) 0.5 M $NaClO_4$ aq. (H_2O : D_2O = 0 : 1)were obtained on roughened Ag surface under 50 MPa in t_{ex}: 10 s with Raman spectra in solution bottom (broken line). For each SERS spectrum (solid line) in the panels, the electrochemical potential was controlled at −0.22, −0.62, −1.22, and −1.62 V vs. Ag/AgCl from bottom to top. (d) Linear sweep voltammograms of each solution are plotted for the same colors of (a, b, c).

at certain potential, these peaks suddenly disappeared at –1.62 V. Instead of the hydration peak, bending peaks became stronger where the reduction current of HER becomes larger as discussed in Figure 4-4, appearing for H_2O at 1608 cm^{-1}, for HDO at 1406 cm^{-1}, and for D_2O at 1184 cm^{-1}. This switching behavior of the interfacial molecules seems to play an important role in the HER reaction in the steady region associated with the elementary step or the rate-determining step. From this aspect, it is considered that the water structure showing bending mode as intermediates under CT resonance dominated the chemical reaction from water to hydrogen.

This hydrated water band in the Raman spectra is also confirmed in the other anion of 0.25 M Na_2SO_4 aq. (H_2O : D_2O = 1 : 1) and the cation of (b) 0.25 M Cs_2SO_4 aq. (H_2O : D_2O = 1 : 1) with the same trend of potential dependence shown in Figure 4-7. However, the OH and OD peak shapes are much more enhanced in the spectra from hydrated to Cs^+ water in the spectra. Since the SERS spectra originate from the interfacial OH bonding, especially in the inner Helmholtz layer, the broadening of the OH (3600 cm^{-1}) and OD (2650 cm^{-1}) peaks corresponds to the increase in the number of waters due to the wider hydration shell for Cs^+ than Na^+.[27,28]

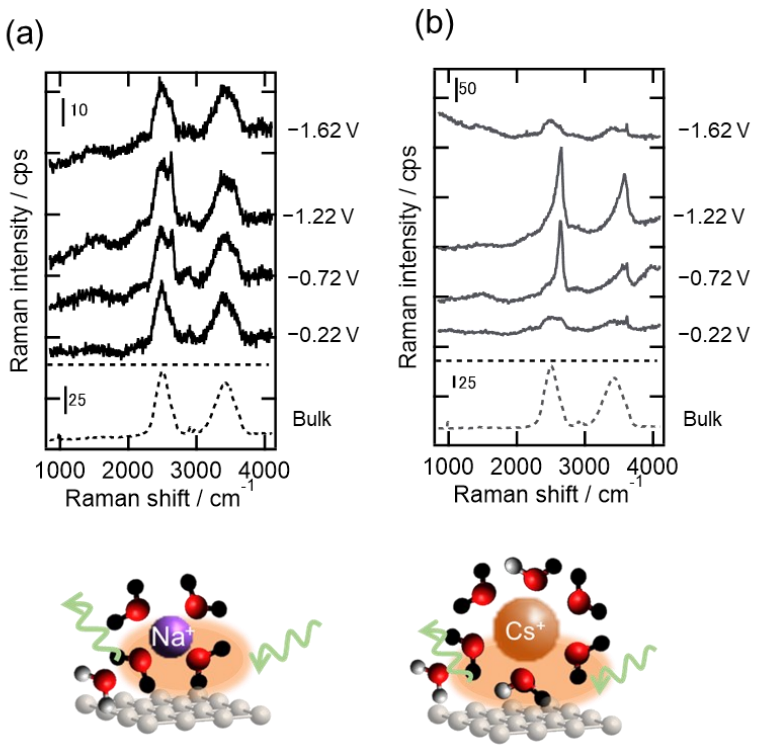

Figure 4-7. Potential dependent series SERS spectra of (a) 0.25 M Na_2SO_4 aq. (H_2O : D_2O = 1 : 1), (b) 0.25 M Cs_2SO_4 aq. (H_2O : D_2O = 1 : 1)were obtained on roughened Ag surface under 50 MPa in t_{ex}: 10 s with Raman spectra in solution bottom (broken line). For each SERS spectrum (solid line) in the panels, electrochemical potential was controlled at −0.22, −0.62, −1.22, and −1.62 V vs. Ag/AgCl from bottom to top.

Furthermore, I focused on the bending mode of each isotope of water as the molecules directly involved in the chemical reaction in the steady region. Figure 4-8a and

b show representative spectra in the negative potential than −1.72 V in H_2O: D_2O = 1 : 1, 1 : 5, and 1 : 10, which were expanded for each wavenumber range of water bending and water stretching. In particular, in Figure 4-8c, the spectra of hydrogen molecules associated with the HER hydrogen evolution reaction were obtained at −1.92V, and I expanded the range of the stretching vibration of the hydrogen gas. Since the peaks of the

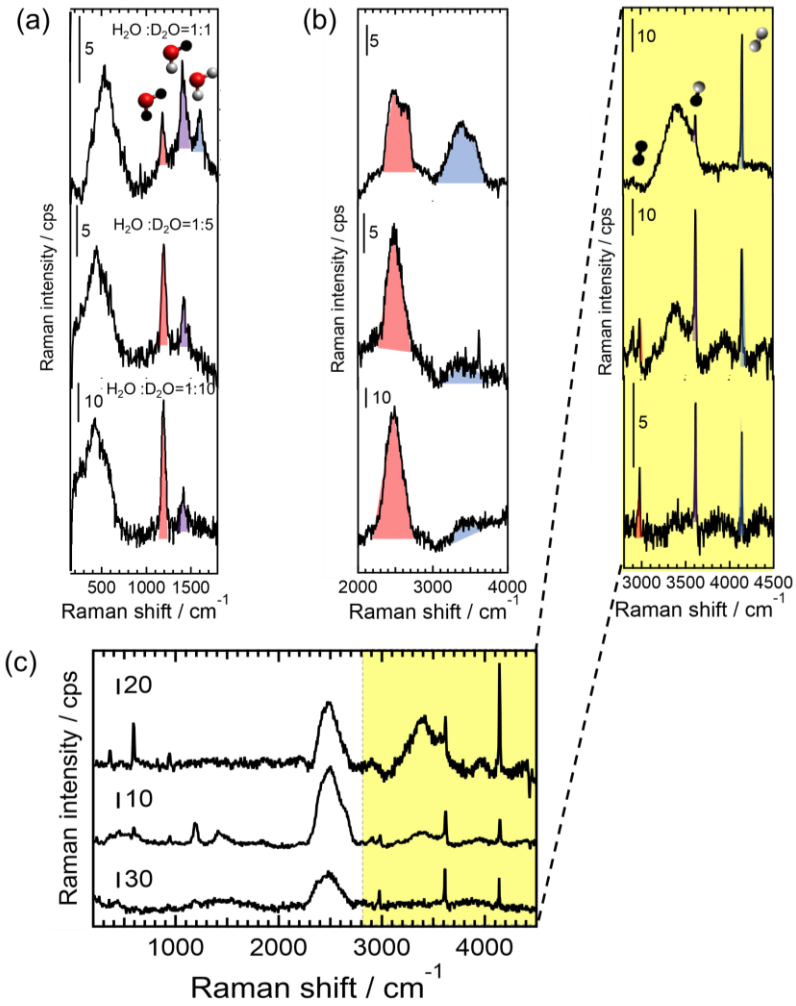

Figure 4-8. Expanded spectra of H_2O : D_2O = 1 : 1 (top), H_2O : D_2O = 1 : 5 (middle), and H_2O : D_2O = 1 : 10 (bottom) were shown in identical vibration regions as (a) bending region, (b) stretching region, and (c) whole region and vibration of hydrogen gas region under 30-50 MPa in t_{ex}: (a,b)10 s at at −1.92 V, at −1.72 V, and at −1.82 V, from top to bottom, or (c) 30 s at −1.92 V for each spectra. The peaks of H_2O and H_2, HDO and HD, or D_2O and D_2 were colored as blue, purple, or red, respectively.

bending mode of H_2O, HDO and D_2O gave different wavenumbers, the peak area can be used to estimate the ratio of reacting water molecules at the interface. The spectra in Figure 4-8c show that the bending mode of H_2O decreases and the bending mode of D_2O increases as the amount of D_2O and HDO increases. Note that the HDO value is larger than preparation value in solution due to isotopic substitution the equilibrium.[29]

$$H_2O + D_2O \leftrightarrow 2HDO, \quad K = 3.75 \qquad \text{(Equation 4-1)}$$

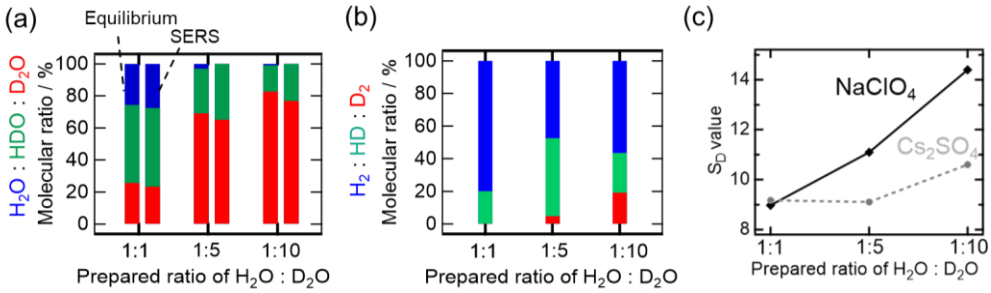

Figure 4-9. (a)The equilibrium fraction of water molecules in solution (left bars) and estimated molecular ratio by SERS intensity ratio of bending mode area (right area) were plotted against the solution composition. H_2O, HDO, and D_2O were colored with red, green, and blue, respectively. (b) [H] / [D] ratios in the gas phase by SERS intensity were plotted with color square: red, green, and blue for H_2, HD, and D_2. (c) Estimates of the separation factor (S_D) were plotted from the [H] / [D] ratio in the gas phase by the SERS intensity of 0.5 M $NaClO_4$ (black solid line)aq. and 0.25 M Cs_2SO_4 aq.(grey broken line) in three isotopic compositions.

This condensation of HOD was also confirmed by the ratio of OH to OD peak area, suggesting that HDO is preferentially adsorbed at the Ag interface during the HER reaction than D_2O. To verify the difference in HER reactivity, the amount of water in solution was estimated as an equilibrium value from the isotopic composition and at the interface from the peak area of the bending mode in Figure 4-8a. The water bending mode was observed in the region where the generated bubbles dissolved, and the water molecules involved in the HER reaction are supplied in a steady state. Since the Na^+ hydrate was difficult to observe in this potential region, it is expected that the water

molecules at the interface are in close proximity to the electrode in the Helmholtz layer. In solution, isotopic substitution occurs and HDO is formed from H_2O and D_2O, but the amount of D_2O at the interface (right bar) is lower for all mixing ratios compared to the equilibrium ratios (left bar) in Figure 4-9a.The difference of the ratio of [H] to [D] at the interface estimated from the bending mode intensity and in the bulk after exchange equilibrium is more than 1.1 times higher in all mix compositions as well as in the stretching mode estimation. In addition, the difference of the ratio of [H] to [D] of product gas and in the bulk after exchange equilibrium shows more than 9 times higher value in all mixed compositions. These values are summarized in Table 4-2.

Table 4-2. Equilibrium population of water and estimation of interface molecular amounts by SERS intensity ration for water and hydrogen gas

Preparation H_2O : D_2O	Equilibrium H_2O : HDO : D_2O	Bending intensity H_2O : HDO : D_2O	Stretching intensity area OH : OD	Vibration intensity height H_2 : HD : D_2
1:0	1 : 0 : 0	1 : 0 : 0	1 : 0	0 : 0 : 1
1 : 1	1 : 1.92 : 1	1.19 : 2.12 : 1	1.00 :1.08	3.99 : 1 : 0
1 : 5	1 : 9.44 : 23.3	0 : 1 : 1.86	1.83 : 4.98	8.90 : 11.0 : 1
1 : 10	1 : 18.0 : 91.0	0 : 1 : 3.34	1 : 8.69	1.93 : 2.26 : 1
0 : 1	0 : 0 : 1	0 : 0 : 1	1 : 0	0 : 0 : 1

From these comparisons with the population of isotopes in bulk, interface and gas, it is clear that the isotope selective process occurs during adsorption and charge transfer in HER. The amount of the separation factor (S_D) which indicates of the isotopic selectivity was calculated by dividing the amount of hydrogen gas by the concentration ratio in solution (Equation 4-2).

$$S_{\mathrm{D}} = \frac{\left\{\frac{[\mathrm{D}]}{[\mathrm{H}]}\right\}_{\mathrm{liq}}}{\left\{\frac{[\mathrm{D}]}{[\mathrm{H}]}\right\}_{\mathrm{gas}}} = \frac{\left\{\frac{2[\mathrm{H_2}]+[\mathrm{HD}]}{2[\mathrm{D_2}]+[\mathrm{HD}]}\right\}_{\mathrm{gas}}}{\left\{\frac{[\mathrm{H_2O}]}{[\mathrm{D_2O}]}\right\}_{\mathrm{liq}}} = \frac{\frac{2I_{\mathrm{H_2}}+I_{\mathrm{HD}}}{2I_{D_2}+I_{\mathrm{HD}}}}{\left\{\frac{[\mathrm{H_2O}]}{[\mathrm{D_2O}]}\right\}_{\mathrm{liq}}} \qquad \text{(Equation 4-2)}$$

The S_{D} values calculated using this equation are shown in Figure 4-9c for 0.5 M NaClO4 and 0.25 M Cs_2SO_4. In particular, as the population of H in the solution decreases, the composition ratio of H in the generated hydrogen molecules tends to increase. The reason composition effects on S_{D} value are considered as the degree of easy water desorption

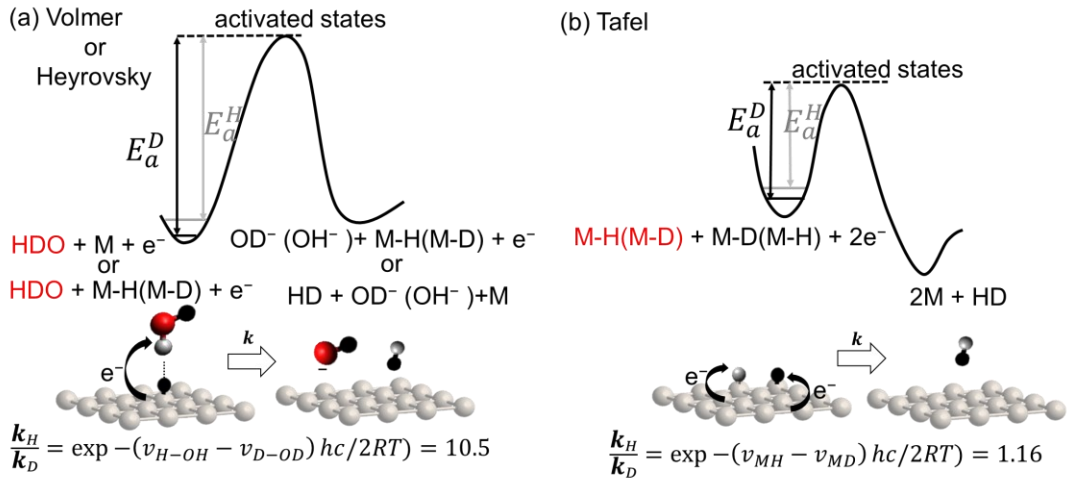

Figure 4-10. Reaction scheme of hydrogen evolution reaction with two elementary steps in desorption process; (a) Heyrovsky process and (b) Tafel process. Theoretical value of reaction ratio for isotope water was estimated from experimental data of vibration mode in (a) and reference of bonding energy in (b).[20]

from bulk to interface depends on the surroundings. When the reactant H_2O is predominantly surrounded by D_2O, the energy to break the hydrogen bond becomes smaller than when surrounded by H2O.[30] At this point, it is also reasonable that the S_{D} values are relatively lower in 0.25 M Cs_2SO_4 than in 0.5 M $NaClO_4$ because the hydration number of water is increased by larger cation of Cs^+ than Na^+. The S_{D} value increases from 10 to about 14 in the 0.5 M $NaClO_4$ aq. on the roughened Ag electrode, which exceeds the experimental value of 10 from the smooth Ag electrode.[12,31,32]

In the reduction reaction of water molecules, there is a Volmer step as the first step. This step is followed by two elementary processes, the Heyrovsky process and the Tafel process, as shown in Figure 4-10. Considering only the excited states up to the intermediate state, the kinetic effect of the Volmer step is the same as that of the Heyrovsky step. Although most of the water molecules at the interface are D_2O or HOD, H_2 is mainly produced. The results of higher separation suggest that isolated OH stretching may be more favorable for the Heyrovsky process, which values in the experiment reached values up to about 14 almost the theoretical value in Figure4-10a. In the HER process, the difference between the thermodynamic Gibbs energies of the isotopes does not differ by a factor of two. Therefore, the kinetic effect is significant, which clearly indicates that the Volmer-Heyrovsky process is dominant and promoted by the nanostructured surface.[33] In other words, it is shown that the proton desorption is faster, especially from the OH group. These trends indicate a large H selectivity, in addition to the composition ratio dependence, suggesting that the CT state of the interfacial water molecules on the nanostructure is involved in the molecular reaction process.

4.4 Conclusion

In this chapter, the local structure of water molecules and the reaction selectivity depending on the nanostructured interfaces were investigated. Electrochemical SERS under high pressured conditions allowed me to observe the CT resonant states and network structure of water molecules at the localized site. The libration and bending modes of H_2O / D_2O / HOD allowed me to determine the molecular layer and their number at the interface. The water molecules in the reduction region would have a higher concentration of Na^+ hydration than in the bulk solution, since the Na^+ hydrated structure is specifically expressed at the surface just before the large reduction current observed. The presence of OD stretching of HOD / D_2O facilitated the observation of such a hydration structure, suggesting that the interfacial hydration structure is comparable to the stability of the water molecule binding network. The interfacial water structure also differed from ions and isotope types. On the other hand, the bending mode and gaseous hydrogen spectra were obtained during the reaction in which the reduction current proceeded. It was found that the hydrogen bonding network and the orientation of the water molecules at the interface were stable. The observation of gaseous hydrogen in the reaction allowed me to quantify both reactants and products. It was confirmed that the OH bond cleavage and the ease of H_2 formation in the electrochemical reaction depended on the composition ratio. In this system, it was found that a specific Volmer-Heyrovsky elementary process was selectively observed even on the roughened Ag, which metal has low catalytic activity, and that the reaction rate was altered. Based on the above results, I will try to control the local HER reaction on different polariton mode by controlling the nanostructure in the next chapter.

4.5 References

(1) Otto, K. E.; Xue, Z.; Zielke, P.; Suhm, M. A. The Raman Spectrum of Isolated Water Clusters. *Phys. Chem. Chem. Phys.* **2014**, *16* (21), 9849–9858.

(2) Ataka, K. I.; Yotsuyanagi, T.; Osawa, M. Potential-Dependent Reorientation of Water Molecules at an Electrode/Electrolyte Interface Studied by Surface-Enhanced Infrared Absorption Spectroscopy. *J. Phys. Chem.* **1996**, *100* (25), 10664–10672.

(3) Men, Z.; Fang, W.; Li, D.; Li, Z.; Sun, C. Raman Spectra from Symmetric Hydrogen Bonds in Water by High-Intensity Laser-Induced Breakdown. *Sci. Rep.* **2014**, *3*, 1–5.

(4) Bertie, J. E.; Ahmed, M. K.; Eysel, H. H. Infrared Intensities of Liquids. 5. Optical and Dielectric Constants, Integrated Intensities, and Dipole Moment Derivatives of H2O and D2O at 22°C. *J. Phys. Chem.* **1989**, *93* (6), 2210–2218.

(5) Shin, D.; Hwang, J.; Jhe, W. Ice-VII-like Molecular Structure of Ambient Water Nanomeniscus. *Nat. Commun.* **2019**, *10* (1), 1–8.

(6) Tong, Y.; Lapointe, F.; Thämer, M.; Wolf, M.; Campen, R. K. Hydrophobic Water Probed Experimentally at the Gold Electrode/Aqueous Interface. *Angew. Chemie Int. Ed.* **2017**, *56* (15), 4211–4214.

(7) McCrum, I. T.; Koper, M. T. M. The Role of Adsorbed Hydroxide in Hydrogen Evolution Reaction Kinetics on Modified Platinum. *Nat. Energy* **2020**, *5* (11), 891–899.

(8) Monteiro, M. C. O.; Goyal, A.; Moerland, P.; Koper, M. T. M. Understanding Cation Trends for Hydrogen Evolution on Platinum and Gold Electrodes in Alkaline Media. *ACS Catal.* **2021**, *11* (23), 14328–14335.

(9) Li, C.-Y.; Le, J.-B.; Wang, Y.-H.; Chen, S.; Yang, Z.-L.; Li, J.-F.; Cheng, J.; Tian, Z.-Q. In Situ Probing Electrified Interfacial Water Structures at Atomically Flat Surfaces. *Nat. Mater.* **2019**, *18* (7), 697–701.

(10) Wang, Y. H.; Zheng, S.; Yang, W. M.; Zhou, R. Y.; He, Q. F.; Radjenovic, P.; Dong, J. C.; Li, S.; Zheng, J.; Yang, Z. L.; Attard, G.; Pan, F.; Tian, Z. Q.; Li, J. F. SI-In Situ Raman Spectroscopy Reveals the Structure and Dissociation of Interfacial Water. *Nature* **2021**, *600* (7887), 81–85.

(11) Chen, Y. X.; Zou, S. Z.; Huang, K. Q.; Tian, Z. Q. SERS Studies of Electrode/Electrolyte Interfacial Water Part II—Librations of Water Correlated to Hydrogen Evolution Reaction. *J. Raman Spectrosc.* **1998**, *29* (8), 749–756.

(12) Minamimoto, H.; Osaka, R.; Murakoshi, K. In-Situ Observation of Isotopic Hydrogen Evolution Reactions Using Electrochemical Mass Spectroscopy to Evaluate Surface Morphological Effect. *Electrochim. Acta* **2019**, *304*, 87–93.

(13) Wiebe, R.; Gaddy, V. L.; Heins, C. Solubility of Hydrogen in Water at 25° C. from 25 to 1000 Atmospheres. *Ind. Eng. Chem.* **1932**, *24* (7), 823–825.

(14) Xiong, X. L.; Ma, H. X.; Tao, X.; Li, J. X.; Su, Y. J.; Zhou, Q. J.; Volinsky, A. A. Hydrostatic Pressure Effects on the Kinetic Parameters of Hydrogen Evolution and Permeation in Armco Iron. *Electrochim. Acta* **2017**, *255*, 230–238.

(15) Hills, G. J.; Kinnibrugh, D. R. The Pressure Coefficient of the Hydrogen Electrode Reaction. *J. Electrochem. Soc.* **1966**, *113* (11), 1111.

(16) Chuang, C. M.; Wu, M. C.; Su, W. F.; Cheng, K. C.; Chen, Y. F. High Intensity Fluorescence of Photoactivated Silver Oxide from Composite Thin Film with Periodic Array Structure. *Appl. Phys. Lett.* **2006**, *89* (6), 1–4.

(17) Monti, O. L. A.; Fourkas, J. T.; Nesbitt, D. J. Diffraction-Limited Photogeneration and Characterization of Silver Nanoparticles. *J. Phys. Chem. B* **2004**, *108* (5), 1604–1612.

(18) Martina, I.; Wiesinger, R.; Schreiner, M. Micro-Raman Characterisation of Silver Corrosion Products : Instrumental Set Up and Reference. *e-Preservation Sci.* **2012**, *9*, 1–8.

(19) Eisenberg, D. S.; Kauzmann, W. *The Structure and Properties of Water*; Oxford University Press, 1969.

(20) Panella, B.; Hirscher, M. Raman Studies of Hydrogen Adsorbed on Nanostructured Porous Materials. *Phys. Chem. Chem. Phys.* **2008**, *10* (20), 2910–2917.

(21) Wang, Y. H.; Zheng, S.; Yang, W. M.; Zhou, R. Y.; He, Q. F.; Radjenovic, P.; Dong, J. C.; Li, S.; Zheng, J.; Yang, Z. L.; Attard, G.; Pan, F.; Tian, Z. Q.; Li, J. F. In Situ Raman Spectroscopy Reveals the Structure and Dissociation of Interfacial Water. *Nature* **2021**, *600* (7887), 81–85.

(22) Lee, M. H.; Kim, S. J.; Chang, D.; Kim, J.; Moon, S.; Oh, K.; Park, K.-Y.; Seong, W. M.; Park, H.; Kwon, G.; Lee, B.; Kang, K. Toward a Low-Cost High-Voltage Sodium Aqueous Rechargeable Battery. *Mater. Today* **2019**, *29* (October), 26–36.

(23) Stefanski, J.; Schmidt, C.; Jahn, S. Aqueous Sodium Hydroxide (NaOH) Solutions at High Pressure and Temperature: Insights from: In Situ Raman Spectroscopy and Ab Initio Molecular Dynamics Simulations. *Phys. Chem. Chem. Phys.* **2018**, *20* (33), 21629–21639.

(24) Wong, A.; Shi, L.; Auchettl, R.; McNaughton, D.; Appadoo, D. R. T.; Robertson, E. G. Heavy Snow: IR Spectroscopy of Isotope Mixed Crystalline Water Ice. *Phys. Chem. Chem. Phys.* **2016**, *18* (6), 4978–4993.

(25) Pastorczak, M.; Nejbauer, M.; Radzewicz, C. Femtosecond Infrared Pump-Stimulated Raman Probe Spectroscopy: The First Application of the Method to Studies of Vibrational Relaxation Pathways in the Liquid HDO/D2O System. *Phys. Chem. Chem. Phys.* **2019**, *21* (31), 16895–16904.

(26) Matt, S. M.; Ben-Amotz, D. Influence of Intermolecular Coupling on the Vibrational Spectrum of Water. *J. Phys. Chem. B* **2018**, *122* (21), 5375–5380.

(27) Singh, M. R.; Kwon, Y.; Lum, Y.; Ager, J. W.; Bell, A. T. Hydrolysis of Electrolyte Cations Enhances the Electrochemical Reduction of CO2 over Ag and Cu. *J. Am. Chem. Soc.* **2016**, *138* (39), 13006–13012.

(28) Xue, S.; Garlyyev, B.; Watzele, S.; Liang, Y.; Fichtner, J.; Pohl, M. D.; Bandarenka, A. S. Influence of Alkali Metal Cations on the Hydrogen Evolution Reaction Activity of Pt, Ir, Au, and Ag Electrodes in Alkaline Electrolytes. *ChemElectroChem* **2018**, *5* (17), 2326–2329.

(29) Pyper, J. W.; Newbury, R. S.; Barton, G. W. Study of the Isotopic Disproportionation Reaction between Light and Heavy Water Using a Pulsed-Molecular-Beam Mass Spectrometer. *J. Chem. Phys.* **1967**, *46* (6), 2253–2257.

(30) Kato, F.; Sugimoto, T.; Harada, K.; Watanabe, K.; Matsumoto, Y. Unveiling Two Deuteration Effects on Hydrogen-Bond Breaking Process of Water Isotopomers. *Phys. Rev. Mater.* **2019**, *3* (11), 1–7.

(31) Rebollar, L.; Intikhab, S.; Snyder, J. D.; Tang, M. H. Kinetic Isotope Effects Quantify PH-Sensitive Water Dynamics at the Pt Electrode Interface. *J. Phys. Chem. Lett.* **2020**, *11* (6), 2308–2313.

(32) Lewis, G. P.; Ruetschi, P. THE DEPENDENCE OF THE ELECTROLYTIC HYDROGEN-DEUTERIUM SEPARATION FACTOR ON THE ELECTRODE POTENTIAL. *J. Phys. Chem.* **1962**, *66* (8), 1487–1492.

(33) Conway, B. E. The Electrolytic Hydrogen–Deuterium Separation Factor and Reaction Mechanism. *Proc. R. Soc. London. Ser. A. Math. Phys. Sci.* **1958**, *247* (1250), 400–419.

Chapter 5

Accelerations of hydrogen evolution reaction via tuning plasmon modes

5.1 Introduction

Although changes in the kinetics and reaction energies of water at interface could be controlled by combining optical modes and geometrical structures so far, there are still few reports on the modulation of electrochemical reactions.[1–4] Up to Chapter 4, I proposed the possibility for the control of the interfacial molecular structures at the strong electric field under CT resonant condition, leading to the modulation of the chemical reaction pathways. However, the clear insight on the design for the nanostructured electrode related to the optical mode has not been clarified yet. Thus, it can be expected that the investigations of the relationship between the reaction activity dependence on the nanostructure would provide insight about the ambient control of electrochemical reactions. In this chapter, I aim to improve the local efficiency of HER at nanostructured interfaces where CT resonance potentially formed without illumination. In particular, I attempted to modulate the interfacial HER reaction at electrodes with low catalytic activity, such as Ag electrodes, by means of optical modes. At the present attempts, I prepared the two-dimensionally arranged nanoparticles which allow to excite the surface lattice plasmon (SLR). The SLR mode is the coupling of LSPR with diffracted light from each nanoparticle.[5,6] I evaluated the change in the optical modes on periodic structures via theoretical calculations and spectroscopic measurements. Through the experiments, I propose a system that plasmon polaritons correlated with water molecules leading to local control of chemical reactions.

5.2 Experimental method

5.2.1 Finite difference time domain simulation of nanostructures

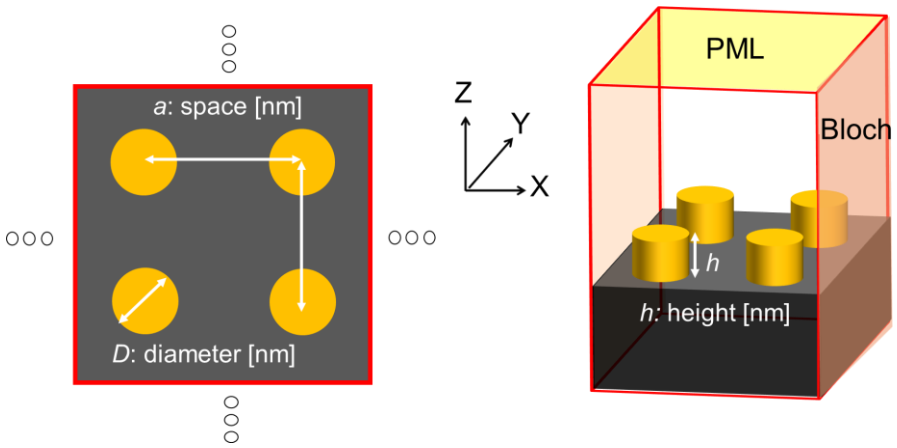

Figure 5-1. Designs of nanostructure simulated by FDTD method. An example of lattice design consists of a disk with each variable abbreviation. Red lines and color filled area correspond to periodic boundary or absorption boundary, called Bloch periodicity or perfectly matched layer (PML) respectively.

In this experiment, the finite difference time domain (FDTD) calculations were performed to evaluate LSPR and lattice mode depending on the structures by the software (Lumerical, Ansys Inc.). The reflection spectra were calculated depending on the lattice structure of the metal with diameter (D) and the distance between the structures called the lattice spacing (a). The structures have a layer thickness of 100 nm. The periodicity of the Bloch boundary condition was introduced to the periodic structures in the XY direction. A perfectly matched layer (PML) was introduced in the vertical direction. The upper part of the structure was satisfied with the wavelength dependent dielectric constant of water. The rough calculation conditions are as follows; mesh setting (overall): auto non-uniform: mesh accuracy 3-7, mesh step: minimum 0.25 nm, boundary conditions: x: Bloch, y: Bloch, Z: PML, source: plane wave, Bloch/periodic, polarization angle: x axis (0 degrees), λ: 200-3500 nm.

5.2.2 Fabrications of nanostructures for hydrogen evolution reactions

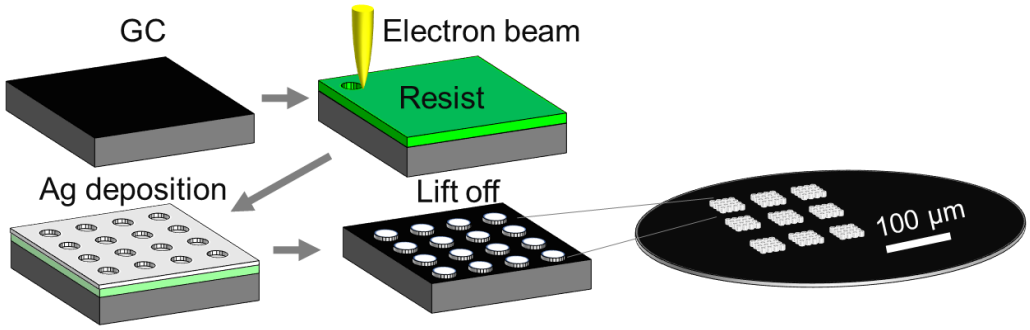

Figure 5-2. Scheme of the deposition process of Ag nanodisk lattice substrate on GC.

As the sample preparation of optical mode defined nano structures on glassy carbon (GC), the electron beam lithography was performed as same procedure as those in Chapter 3. All Ag disks were deposited by Ag evaporation with the height of 100 nm. After Ag deposition, the substrate was cleaned in the N, N'-dimethylacetamide and trichloroethylene with sonication followed acetone washing. Figure 5-2 shows fabrication scheme. The periodic structures are fabricated with diameters (D) of 100, 200, 400 and 800 nm. The nanostructure spacing (a) is designed with the range of 110-1100 nm. Each square lattice is composed of 100 × 100 units, a total of 10,000 units. The optical mode can be tuned by the variation of the periodicity while keeping the shape of the disk nanostructure. Based on these conditions, I tuned the optical modes by changing the diameter and lattice spacing in experiments and evaluated the effects of optical modes on electrochemical reactions.

5.2.3 Reflection spectroscopy measurements under static pressure

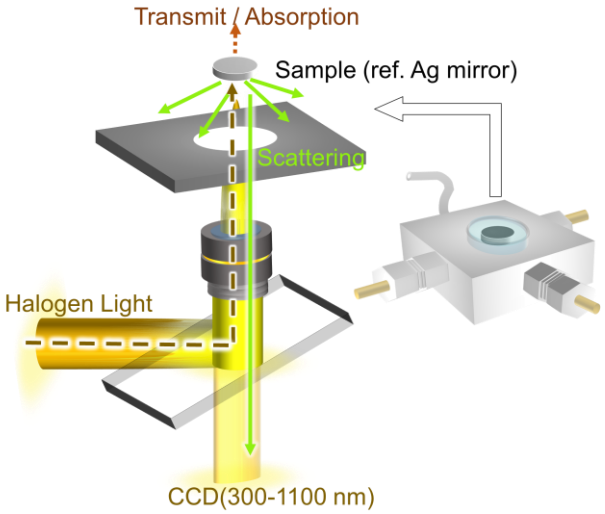

Figure 5-3. Schematic illustration of reflection spectroscopy with referenced sample (Ag mirror) and sample holding in static pressured electrochemical cell.

In principle, it is difficult to measure the plasmon mode by transmitted light, such as extinction spectra, when the structures are supported on opaque substrates. Therefore, we acquired spectra using a reflective optical system and compared them with Ag, which has a high reflectivity of almost 100% over the entire visible spectrum. Since the Ag mirror in air was used as a reference, the intensity in this measurement was reduced by the amount of light absorption and scattering by water, glass, and pressurized oil. From the experiment, GC with a mirror surface of the incident light shows about 10% reflectance compared to the silver mirror, and the reflectance increases up to 100% when the bulk state of Ag was deposited on it. Thus, the absorbing component in the nanostructure shows the same or lower reflectance than that of the GC.[7] For observation in the static pressure cell through transparent windows, I used the x50 objective lens with WD: 13.8 and NA: 0.45 (Nikon Inc.),

5.2.4 Video analysis of HER on the nanostructures

For taking movie of HER, three electrodes, WE: Ag/GC, CE: Au, RE: Au were used in 0.5 M $NaClO_4$ aq. under high hydrostatic pressure conditions of 75 MPa as same set up as in Chapter 4. To observe the wide region of electrode surface through several windows of cell, the ultra-long working distance x10 objective lens (WD = 21, Olympus) was chosen. The movies were taken by CCD camera (1920 × 1080 pixel, 2.9 μm^2 per pixel, Wraymer, Inc.) equipped with the microscope (Leica Microsystems) optical as 60 fps rate in the position of ocular lens. The linear sweep voltammetry (LSV) was set to 5 mV/s and the movie was observed simultaneously with LSV measurements. The local current (I_{H_2}) was estimated from the bubble volume with semi sphere approximation as bellow equations. N_{H_2} is the number of molecules, which is calculated by bubble volume(V) , density of hydrogen (d_{H_2}) under 75 MPa 40 g/L and molecular weight of hydrogen (MW_{H_2}) .[8]

$$N_{H_2} = \frac{V \times d_{H_2}}{MW_{H_2}} \qquad \text{(Equation 5-1)}$$

Here, the bubble volume is automatically analysed using the motion analysis software (Dipp-Macro II, DITECT Co. Ltd.) Then, the current can be estimated by detect time (t) and Faraday constant (F). Note that when converting to current density, I defined the electrode area as the projected area of the lattice structure.

$$I_{H_2} = \frac{F \times N_{H_2}}{t} \qquad \text{(Equation 5-2)}$$

5.3 Results and discussion

5.3.1 Conformation of optical mode of nanostructures

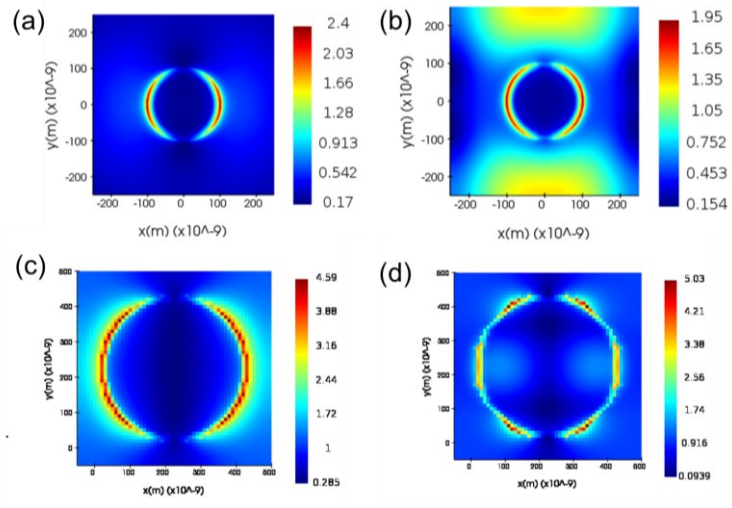

Figure 5-4. Calculated electric field intensity distribution of nanodisk of (a, b) D= 200 and (c, d) D = 400 nm) with (b) a= 500 nm and (c, d). Boundary condition set as (a) PML boundary (isolate) and (b, c, d)) Bloch boundary (SLR mode). The filed distribution map is obtained at (c) the top position of Ag nano disk and at (d) the interface position of Ag nanodisk and GC.

The single LSP mode of the Ag disk has the localized electric filed only in the vicinity of the metal surface as shown in Figure 5-4 a. To confirm the plasmon mode coupled with diffracted light, I also mapped the electric field intensity distribution in Figure 5-4b by fitting the Bloch boundary condition to the FDTD region as a periodic condition.[9,10] Since the intensity is normalized by 1 V/m, it is confirmed that the electric field is distributed in the wide area of the unit region as a result of diffraction interference. This diffraction coupled polariton mode are expected to interact the water molecules coherently.[11] On the other hand, because the lattice substrate system has three interfaces of water and Ag and GC, the special polarization also depends on the position of nanodisk by the difference of plasmon damping at each position. As a result, the electric field distribution at the bottom position shows a different polarization from that at the top of the nanodisk in Figure 5-3c, d. It should be mentioned that these non-uniform polariton

modes in nanostructure directly affect the spectral shapes.[12–14]

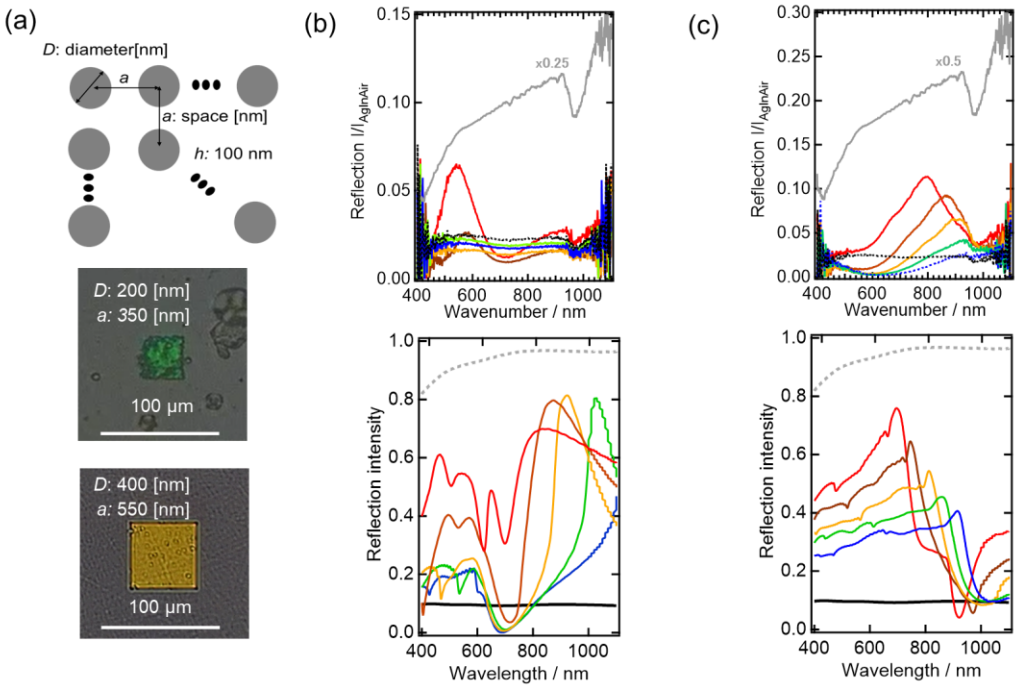

Figure 5-5. (a) Design and optical images of plasmonic disk lattices with different disk diameter (D) and lattice spacing (a). (b) Experimental reflection spectra of Ag disk grating of (b) D= 200 nm with a= 300, 350, 400, 450, 500 nm and (c) D= 400 nm with a= 500, 550, 600, 650, 700 nm are shown as reflection ratio to Ag mirror reference in air. In figure (b), red, brown, orange, green, and blue lines represent the spectra of a= 300, 350, 400, 450, and 500 nm, respectively. In figure (c), the red, brown, orange, green, and blue lines represent the spectra of a= 500, 550, 600, 650, and 700 nm, respectively. The gray line and black dashed lines correspond to Ag 100 nm films and GC 100 nm layer. All spectra are obtained in 0.5 M $NaClO_4$ aq. under 75 MPa. Bottom panels show FDTD calculations of each disk spacing with Ag and GC in the same manner as the experimental spectra.

To confirm the optical mode of lattice structure, the visible region reflection experiments were carried out. The diameter (*D*) was set to 200 and 400 nm, the structure height was fixed at 100 nm, and only the lattice spacing (*a*) was varied to 300, 350, 400, 450, 500 nm and 500, 550, 600, 650, 700 nm, respectively for reflection measurements. The design conditions and optical images are shown in Figure 5-5a. The measured reflection spectra for these structures are shown in the upper part of Figure 5-5b and c, and the corresponding FDTD simulations are shown in the lower part. The experiments

were performed in a static pressured electrochemical cell at 75 MPa. The black dashed line in each figure is the reflection from the GC, and the gray line corresponds to the reflection from the 100 nm Ag film. The dip-like peak near 900 nm is considered to be absorption originating from the glass and oil used in the static pressured cell. Scattering components from Ag are above the black line, and plasmon modes corresponding to LSP and SLR are observed as dips. The red line spectra in Figure 5-5b represent a D= 200 nm diameter sample with a= 300 nm, which has an SLR mode at about 520 nm, while the peak of the SLR modes at other lattice spacings shifted to higher wavelengths and became smaller. This trend was similar for the D= 400 nm shown in Figure 5-5c. The a= 500 nm lattice has a peak at 780 nm, but a broad scattering component from 630 to 850 nm. This is because the peak wavelength of SLR is around 1200 nm, which cannot be detected by visible light reflectance measurements. From the above, it can be seen that the optical modes of the actual structure are experimentally evaluated and are in good agreement with the FDTD calculations. Since it has been confirmed that the optical modes can be observed at arbitrary wavelengths by controlling the diameter and lattice spacing, electrochemical measurements on these structures were performed.

Reflectance spectra of a square lattice structure on a disk with diameter of 200 nm, 100 nm thickness, and 500 nm lattice spacing were taken with GC reference in 0.5 M $NaClO_4$ aq. at 75 MPa. Figure 5-6a and b show the spectra of GC itself and Ag nano disk, respectively. For each substrate, electrochemical potential was scanned from 0.39, to −1.61 V vs Ag/and rescanned to 0.39 V vs. RHE. As in Figure 5-6a, the GC itself is stable to the negative potential sweep, even though the refractive index changes on the surface due to occurrence of HER. On the other hand, as shown in Figure5-6b, the absorption and scattering peaks of the Ag nano-disk SLR became maximum at −0.61 V

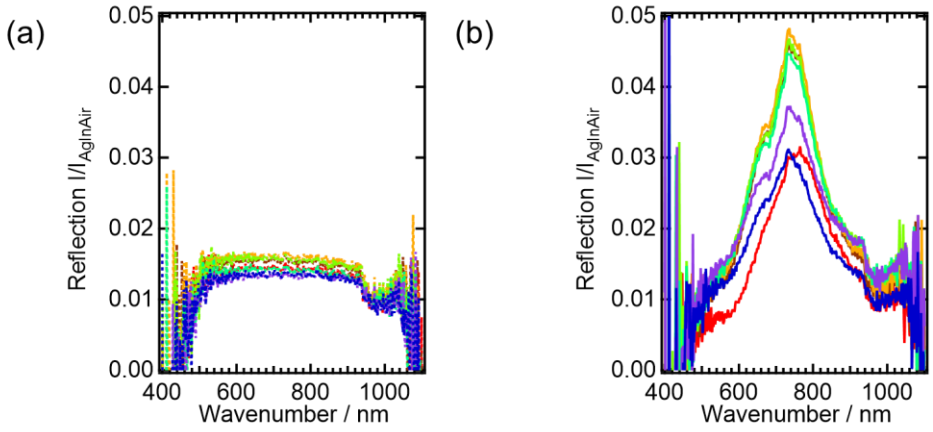

Figure 5-6. Reflection spectra of (a) GC only and (b)Ag nanodisk lattice on GC substrate. Potential was kept at negative potential from 0.39 V to − 1.61 V vs. Ag/AgCl in 0.5 M $NaClO_4$ aq. under 75 MPa. Red, brown, orange, light-green, green, purple, and blue line represent the potential of 0.39 V, −0.11 V, −0.61 V, −1.31 V, −. V, −1.61 V, and 0.39 V, respectively, which potential order is same as experimental sequential order.

after the negative potential sweep, then decreased, After the return to 0.39 V, the spectrum was slightly blue shifted compared to that at the initial 0.39 V. This is due to the destruction of the structures during HER. Although some deformation of the structure occurred, it was confirmed that the structure was generally maintained during HER under 75 MPa. Therefore, it is agreed that in this potential region the lattice structure for plasmon active substrate under 75 MPa can be used for HER measurement.

5.3.2 Evaluation of hydrogen evolution on each plasmon mode

To reveal the relationship between the optical mode and HER activities, various Ag nanodisk lattice was prepared on GC with different diameters and lattice spacing as shown in Figure 5-7a. SEM images of the Ag lattice structures formed on GC corresponding to the bright-field image with the D = 200 to 800 nm and a= 210 to 1100

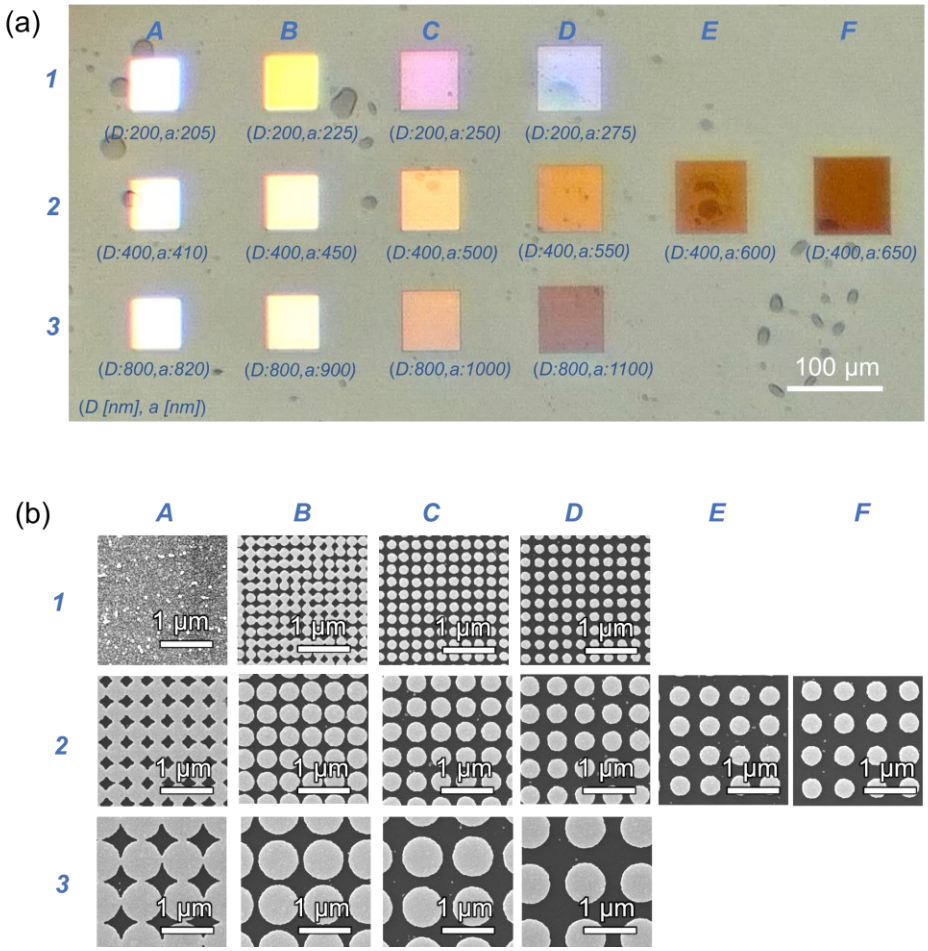

Figure 5-7. (a) CCD image and (b) SEM image of plasmonic disc lattices on GC of various disk diameter (D) and lattice spacing (a) corresponding to blue text in figure. CCD image was taken by × 3.7 magnification in 0.5 M $NaClO_4$ aq. under 75 MPa at open circuit. (b) SEM image was taken by ×25000 magnification.

nm were given as Figure 5-7b. Almost all disk lattices show good conformation as CAD design but the short lattice spacing such as a= 205, 225, 410, 820 nm showed the different shapes from default design. The lattice with D= 200 and a= 205 nm (marked as 1A) shows a fully covered Ag layer. The lattice of 1B (D = 200 and a= 225 nm), 2A (D= 400 and a= 410 nm), or 3A (D= 800 and a= 820 nm) show the hole-like structures due to the limitation of the focal size of the electron beam. Although there are small differences from the CAD designs, the lattices had enough variation coupled with resonance peaks of the plasmon

mode. In particular, the lattices show different colors depending on the diffraction coupling although with same diameter. Using these Ag nanostructures, the electrochemical potential was swept up to the HER potential region with video image recording under the static pressure of 75 MPa to reveal the details of the local modulation of HER, which has hardly been observed by electrochemical measurements.

The snapshots of the electrode interface at each potential are shown in Figure 5-8, which was measured simultaneously with the first cathodic scan of the LSV from −0.39

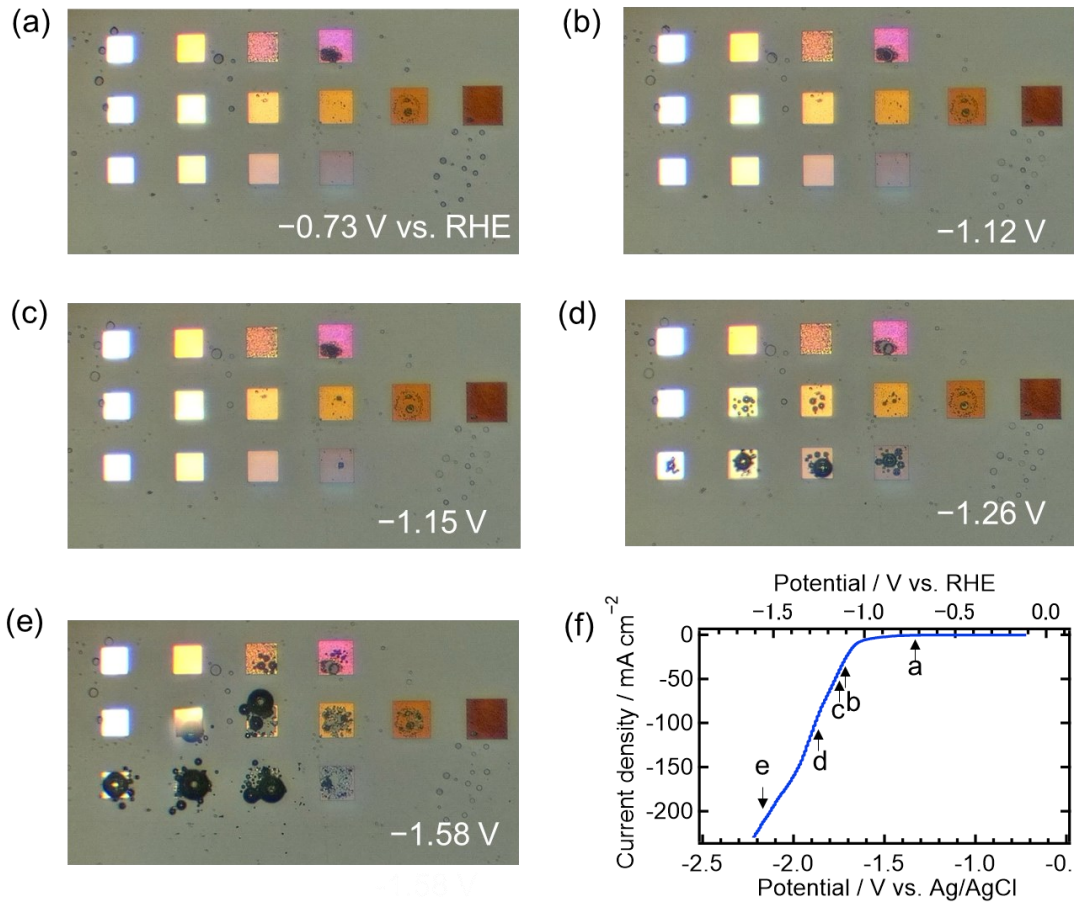

Figure 5-8. CCD images of plasmonic disc lattices on GC in 0.5 M $NaClO_4$ aq. under 75 MPa were taken with LSV measurement, where at (a) −0.73 V, (b) −1.12 V, (c) −1.15 V, (d) −1.26 V, and (e) −1.58 V vs. RHE. (f) Current density on Ag/GC plasmonic lattice substrate was plotted to electrochemical potential of the substrate with each picture of (a-d).

to −1.61 V vs. RHE. In the range of −0.39 to −1.12 V vs RHE, there was only a slight blue shift on several structures due to the change in electron density in the structures. The first hydrogen bubble formation was observed on the lattices of 2C (*D*= 400 nm and *a*= 550) and 3D (*D*= 800 nm and *a*= 1100 nm) at −1.15 V vs RHE (Figure 5-8c). Second at −1.26 V vs RHE (Figure 5-8d), hydrogen bubble evolutions were observed in the several lattices of *D* = 400 and 800 nm but not the *D* =200 or in the other lattice spacings. In the very negative potential region (−1.58 V, Figure 5-68), the lattice of *D*= 200 nm shows the evolution of hydrogen gas, while some lattices with strong bubble generations seemed not to have the da mage of hydrogen gas. The disk diameter and lattice spacing dependence of the hydrogen evolutions on the structure were reproduced by several experiments. As the current values increased, the hydrogen evolution reaction took place over the entire substrate. However, most of the hydrogen on the substate dissolves before growing as visible bubbles. In contrast, bubble formation was specifically enhanced in some specific structures where the rate of hydrogens exceeds the dissolution rate. In this case, especially for the same diameter of *D*= 400 nm, it was found that the largest lattice spacing did not enhance bubble generation, which is unlikely to be due to simple geometric factors alone. Although the lattices of 1A (*D*= 200 and *a*= 205 nm) are practically uniform Ag films, no bubbles were observed in them. These results support the relationship between optical modes and hydrogen evolution rate at the Ag interface.

From the video image, hydrogen bubble generation is observed at each lattice structure with different starting potential and number of bubbles. Using the software diameter analysis and Equation 5-2, the local current density was calculated from these grids as shown in Figure 5-9. Since 1A, 1B, 2A, 2F and 3A did not generate the bubbles, the current cannot be defined in figures for the current potential range of -0.39 to -1.61.

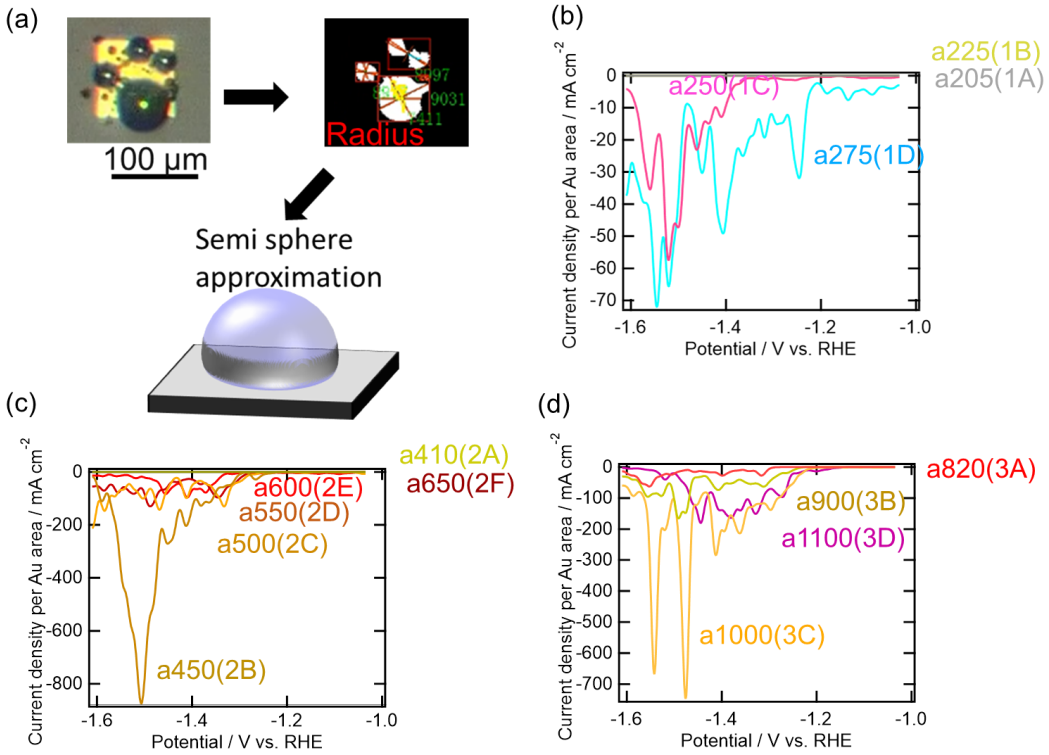

Figure 5-9. (a) Video image analysis of hydrogen gas evolution performed by auto-fitting software using semi spherical approximation of current density. (b, c, d) Current density is estimated from the bubble volume under 75 MPa for (a) 1A-1D , (b) 2A-2F and (a) 3A-3D structures.

However, as shown in LSV, the reduction current occurs over an entire area of the Ag/GC substrate where the bubbles were never produced, at least not in visible size. Focusing on the amount of current density, 2B and 3C show the vigorous bubble generation and mark enormous current more than 10 times compared to low active structures: 1C, 2D, 2E, 3B. Although the same column of 1C, 2C and 3C have almost the same total area because these lattices are similar in shape, the HER activity of 3C is obviously highest. It should be noted that the estimated current density may be overestimated due to the different bubble shape, e.g. not always hemispherical, but the dependence of bubble generation is clear. Therefore, the specific structure shows efficient hydrogen evolution activity more than GC, only Ag layer (1A) and others.

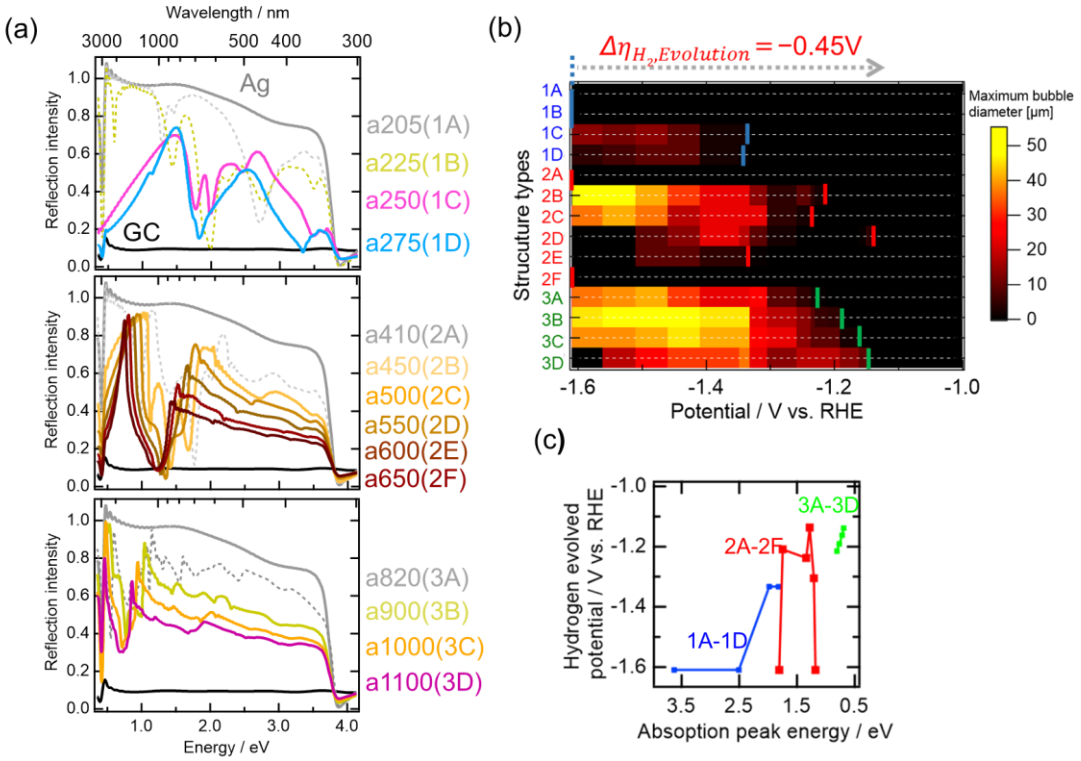

Figure 5-10. (a) Wide range reflection spectra are calculated by FDTD method to row 1, 2 and 3C with each lattice spacing of Fig. 5-7. The spectra of 1A, 1B, 2A and 3A (Dot lines of) are simulated as hole structure. (b) Bubble diameter analysis of evolved hydrogen gas were traced with LSV in 0.5 M $NaClO_4$ aq. under 75 MPa The colored lines show the first hydrogen evolution potential for 1A-1D (blue), 2A-2F (red) and 3A-3D (green). (c) The hydrogen evolution potential is plotted as the observed first hydrogen potential for each nanodisk lattice as a function of the absorption peak from the FDTD calculation.

For all of the above structures, FDTD simulations of the reflection spectra up to the infrared region show that the position of the diffraction-coupled absorption peak is proportional to the increase in diameter and lattice spacing in Figure 5-10a. The absorption intensities per unit area are not simply comparable, however, for large diameter and longer lattice spacing structures show strong absorption, especially for highly active 2D and 3D structures. The peak shift at the same diameter corresponds to the diffraction coupling to the plasmon. Figure 5-10b shows a plot of the bubble diameter size at each potential shown in Figure 5-8. By the structure type, bubble generation was

modulated up to +450 mV compared to the Ag thin film (1A) where no bubble generation was observed in the experimental potential range. This result indicates that even non-catalytic metals such as Ag can locally accelerate the rate of hydrogen evolution by nanostructured interface. Finally, Figures 5-9c show the bubble formation potential plotted against the absorption wavelength of the SLR mode obtained from FDTD simulations. Although there is no clear reaction modulation in some of the peaks, the bubble formation potential is positively correlated with the absorption wavelength of the lattices. This tendency is supported by the fact that at the pressure condition of 50 MPa described in Chapter 4, the potential at which hydrogen gas is partially observed at SERS hot spots under CT resonating with the 514 nm (2.4 eV) laser in the roughened Ag wire is −1.31 V vs. RHE (−1.92 V vs Ag/AgCl).

5.4 Conclusion

In this chapter, the optical mode response to the water reduction reaction by a non-catalytic metal of Ag nanostructure is verified. Microscopic video analysis of the HER reaction at high pressure successfully visualized the difference in the rate of local bubble formation. The spectroscopic properties of the HER reaction under high pressure and electrochemistry were successfully obtained on a non-transparent substrate by reflection spectra, where it is usually difficult to obtain spectroscopic properties. In addition to experimental spectra, the identification of the SLR mode was confirmed by comparison with FDTD calculations. For structures where the absorption is not in the visible region, I estimated the optical modes from the visible to the infrared region by FDTD. Thus, it was found that the differences in the bubble-generated potentials are related to each optical mode of the nanostructures. The electronic transition of water molecules is 6.7 eV, the vibrational level of OH stretching is 0.44 eV, and the vibrational level of bending is 0.18 eV, so the response to the optical mode was observed even though it is not consistent with these values.[15] This may indicate that not only the peak position of the SLR mode, but also the strength, half-width, and lifetime of the LSPR mode play the important role in the responses. The above findings enable us to control molecular reactivity by designing nanostructure-specific optical modes, which can be applied to all kinds of electrochemical reactions, not only Ag and HER.

5.5 References

(1) Kazuma, E.; Lee, M.; Jung, J.; Trenary, M.; Kim, Y. Single-Molecule Study of a Plasmon-Induced Reaction for a Strongly Chemisorbed Molecule. *Angew. Chemie - Int. Ed.* **2020**.

(2) Fukushima, T.; Yoshimitsu, S.; Murakoshi, K. Inherent Promotion of Ionic Conductivity via Collective Vibrational Strong Coupling of Water with the Vacuum Electromagnetic Field. *J. Am. Chem. Soc.* **2022**.

(3) Ueno, K.; Oshikiri, T.; Sun, Q.; Shi, X.; Misawa, H. Solid-State Plasmonic Solar Cells. *Chem. Rev.* **2018**, *118* (6), 2955–2993.

(4) Ebbesen, T. W. Hybrid Light-Matter States in a Molecular and Material Science Perspective. *Acc. Chem. Res.* **2016**, *49* (11), 2403–2412.

(5) Minamimoto, H.; Oikawa, S.; Hayashi, T.; Shibazaki, A.; Li, X.; Murakoshi, K. Electrochemical Fine Tuning of the Plasmonic Properties of Au Lattice Structures. *J. Phys. Chem. C* **2018**, *122* (25), 14162–14167.

(6) Khlopin, D.; Laux, F.; Wardley, W. P.; Martin, J.; Wurtz, G. A.; Plain, J.; Bonod, N.; Zayats, A. V.; Dickson, W.; Gérard, D. Lattice Modes and Plasmonic Linewidth Engineering in Gold and Aluminum Nanoparticle Arrays. *J. Opt. Soc. Am. B* **2017**, *34* (3), 691.

(7) Yanagawa, H.; Hinamoto, T.; Kanno, T.; Sugimoto, H.; Shioi, M.; Fujii, M. Gold Nanopillar Array with Sharp Surface Plasmon Resonances and the Application in Immunoassay. *J. Appl. Phys.* **2019**, *126* (22).

(8) Elberry, A. M.; Thakur, J.; Santasalo-Aarnio, A.; Larmi, M. Large-Scale Compressed Hydrogen Storage as Part of Renewable Electricity Storage Systems. *Int. J. Hydrogen Energy* **2021**, *46* (29), 15671–15690.

(9) Kravets, V. G.; Kabashin, A. V.; Barnes, W. L.; Grigorenko, A. N. Plasmonic Surface Lattice Resonances: A Review of Properties and Applications. *Chem. Rev.* **2018**, *118* (12), 5912–5951.

(10) Li, G. H. Y.; Li, G. Necessary Conditions for Out-of-Plane Lattice Plasmons in Nanoparticle Arrays. *J. Opt. Soc. Am. B* **2019**, *36* (4), 805.

(11) Heiderscheit, T. S.; Oikawa, S.; Sanders, S.; Minamimoto, H.; Searles, E. K.; Landes, C. F.; Murakoshi, K.; Manjavacas, A.; Link, S. Tuning Electrogenerated Chemiluminescence Intensity Enhancement Using Hexagonal Lattice Arrays of Gold Nanodisks. *J. Phys. Chem. Lett.* **2021**, *12* (10), 2516–2522.

(12) Debu, D. T.; Ghosh, P. K.; French, D.; Herzog, J. B. Surface Plasmon Damping Effects Due to Ti Adhesion Layer in Individual Gold Nanodisks. *Opt. Mater. Express* **2017**, *7* (1), 73.

(13) Habteyes, T. G.; Dhuey, S.; Wood, E.; Gargas, D.; Cabrini, S.; Schuck, P. J.; Alivisatos, A. P.; Leone, S. R. Metallic Adhesion Layer Induced Plasmon Damping and Molecular

Linker as a Nondamping Alternative. *ACS Nano* **2012**, *6* (6), 5702–5709.

(14) Madsen, S. J.; Esfandyarpour, M.; Brongersma, M. L.; Sinclair, R. Observing Plasmon Damping Due to Adhesion Layers in Gold Nanostructures Using Electron Energy Loss Spectroscopy. *ACS Photonics* **2017**, *4* (2), 268–274.

(15) Eisenberg, D. S.; Kauzmann, W. *The Structure and Properties of Water*; Oxford University Press, 1969.

Chapter 6
General conclusions

In this doctoral thesis, I achieved the modulation of molecular motion, structure, and even the reactivity at the nanoscale interface through highly sensitive vibration observation measurements under electrochemical controls. Especially, focusing on plasmons as polariton, I have successfully revealed how their intrinsic modes interact with molecules.

In Chapter 1, I introduce the possibility of molecular manipulation by polariton mode as the frontier of chemical reaction control.

In Chapter 2, SERS investigations were carried out on how localized electric fields affected the two-dimensional diffusion behavior of adsorbed molecules on plasmonic nanoarrays. This study demonstrated that it is possible to control the translational motion of organic molecules in a way that cannot be achieved by conventional laser polarization control. Moreover, it was demonstrated that the molecular condensation behavior was modulated by the types of organic solvents such as water or acetonitrile and salts concentration. It was also understood how electrochemical potential control could achieve the aggregation of interfacial molecules in a localized electric field.

In Chapter 3, I examined the molecular motion at a gap of single bowtie structure under electrochemical potential control and light illumination. The control of the electrochemical potential defines the Fermi level in the metal, resulting in the charge transfer resonance, which modulates the vibrational motion of the molecules at the interface. It was confirmed that the auxiliary effect structural isomers in solution modified the aggregation behavior when they actually aggregate under the driving force of the

localized electric field. In particular, under charge-transfer resonance, I found distinct molecular aggregation domain under the presence of structural isomer that cannot be achieved by thermodynamic adsorption equilibrium This allowed us to propose the ultimate molecular control possible when polaritons, electrochemical potentials, and intermolecular forces interact with each other.

Following above facts, in Chapter 4, I conducted the modulation of water molecular behavior at the nanostructured surface. Firstly, the water molecular structures at the surface of nanostructures during the electrochemical reactions were investigated by SERS measurements. In order to investigate the SERS spectroscopy of the interface during the hydrogen evolution reaction, I constructed an electrochemical spectroscopy measurement system in a high-pressure cell to avoid bubble inherence. It was observed that Na^+ hydration structure changed to the steady-state structure during reduction reaction. By examining the isotope separation rate of HER from the detection of molecular hydrogen by SERS spectra under static pressure, it was found that the elementary step such as Volmer-Heyrovsky step are accelerated on nano structured Ag surface.

In Chapter 5, based on the finding about the modulation of the reduction reaction of water molecules at nanostructures, I evaluated the rate of bubble generation by the microscopic movie to determine how the optical mode of plasmon polariton of nanostructures affects the hydrogen evolution reaction rate. By conducting measurements under a static pressure, where bubbles enable to dissolve into water quickly, I confirmed that the specific plasmon mode on two-dimensional lattice structure was responsible for the changes in the rate of the generated hydrogen gas.

In Chapter 6, I summarized my doctoral thesis and the perspective of polariton electrochemistry. In these studies, by focusing on the interaction between the plasmon polariton and the molecules at the electrode interface involved in the reaction, I achieved the active modulation of translational motion, vibrational motion, and chemical reaction modulation at the nanostructured interface. In particular, in a plasmon field with a strong localized electric field, I reported for the first time the formation of a unique molecular layer, which cannot be obtained by thermodynamic equilibrium under CT resonance, by combining motion manipulation with electronic state tuning by electrochemical potential. Furthermore, by spectroscopically observing the water molecule structure involved in the reduction reaction at the nanostructure interface where the electric field is localized, I discovered the possibility of elementary process modulation. Based on these findings, I finally clarified that the polariton state of the electrochemical interface with different polariton modes is correlated with the rate of the hydrogen evolution reaction. This doctoral thesis established the polariton control of interfacial reactions and proposed a new reaction design guideline for polariton electrochemistry.

Acknowledgement

I would like to express my gratitude to Prof. Kei Murakoshi for his discussion and teaching whole my student life.

I would also like to thank Prof. Tetsuya Taketsugu, Prof. Hiroki Habazaki and Prof. Kosei Ueno for their helpful suggestions with deep insight.

Many thanks to Assistant Prof. Hiro Minamimoto for much support whenever I need, even in Kobe University. I thank Assistant Prof. Tomohiro Fukushima for the experimental proposal.

The entire study in this thesis could not have been accomplished without the cooperation of the laboratory members. I am grateful to Shunpei Oikawa, Fumiya Kato, Takayoshi Furukawa, Shinya Suzuki, Daiki Sato, and Takahiro Hayashi for discussions, experimental suggestions, and life advice. I am grateful to Rumi Akiyama, Mariko Yonezawa, Junko Hattori, and Hiroko Nishimoto as secretaries in the Physical Chemistry Laboratory for their dedicated support.

I am also grateful to all my colleagues at Hokkaido University for their humor and for giving me the ambition to be a scientist. I especially appreciate one of my best friends, Yumehiro Manabe, Seiya Hirano, Ryuki Abe, Shuichi Ebisawa, Kenta Nishigata, Miku Izutsu, Ryo Ogawa, and Fumikazu Ueda.

Finally, I would like to express my deepest gratitude to my family and friends for believing in my potential. My father, my mother, my brother, my mentor Taro Yamauchi, and my partner Marie.

Noabuki Oyamada